A Search for a Light Charged Higgs Boson Decaying to $c\bar{s}$ at $\sqrt{s} = 7$ TeV

A THESIS

SUBMITTED TO THE UNIVERSITY OF MANCHESTER

FOR THE DEGREE OF

DOCTOR OF PHILOSOPHY (PHD)

IN THE FACULTY OF ENGINEERING AND PHYSICAL SCIENCES

Alex Martyniuk

PARTICLE PHYSICS GROUP

SCHOOL OF PHYSICS AND ASTRONOMY

2011

Contents

Word count: 29452

List of Figures

List of Tables

Abstract

A search for a light charged Higgs boson decaying into $c\bar{s}$ is presented using data recorded in pp collisions at $\sqrt{s} = 7$ TeV. The analysis uses a data sample corresponding to an integrated luminosity of 35.3 pb^{-1} collected by the ATLAS detector at the LHC between June and November 2010. The search is based on the semi-leptonic $t\bar{t}$ channel searching for the process $t \rightarrow H^+b$ where $H^+ \rightarrow c\bar{s}$. The invariant mass distribution of the dijet system consistent with the hadronic decay of a W^+ is used to search for a secondary bump from hadronic H^+ decays. With no observation of the charged Higgs signal, 95% confidence level upper limits on the decay branching ratio of top quarks to charged Higgs bosons are set as a function of the charged Higgs boson mass.

Declaration

No portion of the work referred to in the thesis has been submitted in support of an application for another degree or qualification of this or any other university or other institute of learning;

Alex Martyniuk
School of Physics and Astronomy
University of Manchester
Oxford Road
Manchester
M13 9PL
United Kingdom

Copyright

Acknowledgements

I would like to firstly thank my supervisor, Un-ki Yang, for guiding me through the minefield and helping to defend my work to the collaboration. I would also like to thank Mark Owen for his tireless support for my analysis and especially for his help with the ever shifting statistical methods.

I would like to thank Jenna and Paul for setting the sturdy foundations for this analysis and teaching me some of its subtler points. Thanks to Joerg and Simon for allowing me to be let loose developing the Trigger Tool. Thanks to all the people who I have shared a coffee (or indeed beer) with over the fantastic years I had at Manchester and CERN. I am sure most useful exchanges occurred frequently during those breaks from work, but the details get lost in the noise. Special thanks to Fred Loebinger for not only allowing me to do a PhD, but also providing many of the lively coffee time discussions and general support over the years.

Thanks to all my friends both in Manchester and CERN for providing various sources of entertainment; snowboarding (not skiing), climbing, pub quizzes, computer gaming (especially LANs), DnD etc. (because what I really need is more esoteric knowledge), boardgames, poker, film nights and finally Sandbar. People should know who contributed to what. Without these things I may well have descended further into madness. Additional friendship thanks go to Graham for putting up with me as a housemate for so many years.

Thanks to my family Gay, Stefan and Nadine for putting up with me over the years. Finally, but by no means least, special thanks to Gemma for her love and support over the years. Without her help this thesis would be emptier along with my future.

To Gay and Stefan

Chapter 1

Introduction

The Standard Model (SM) of particles physics is possibly the most successful theory humankind has ever conceived. The cumulative work of generations of physicists, the SM elegantly describes the elementary particles and the strong, electromagnetic and weak interactions between them. Its predictions have successfully borne the brunt of years of experimental testing. The theory remains to this day a strong predictive force, however some questions are left unanswered. One of the remaining questions is the nature of electroweak symmetry breaking, the progenitor of particle masses. In the SM the symmetry is broken by the Higgs mechanism. Currently particle physics experiments around the world, using the LHC and Tevatron accelerators, are searching for the Higgs boson, a physical manifestation of the Higgs mechanism. The mass of the Higgs in the SM is expected to be of order 100 GeV[1] from precise mass measurements of the W boson and top quark [1, 2]. Therefore it is expected to be well within the reach of current experiments.

In addition to the origin of mass there are a few further issues that need to be solved. These problems include; the solution to the hierarchy problem, an observed dichotomy between the experimental and theoretical expectations for the Higgs boson mass; the source of the matter and anti-matter asymmetry that led to a matter dominated universe; the origin of dark matter in the universe. Many extensions to the SM have been proposed over the years to try and solve these problems. This thesis will

[1]Natural units, $c = \hbar = 1$, are assumed throughout this thesis.

concentrate on models containing an extended Higgs sector compared to the SM. This extended sector leads to five physical Higgs bosons; three neutral, h^0, H^0 and A^0 and two charged H^+ and H^-. The discovery of a charged Higgs boson would be an unequivocal sign of physics beyond the SM. Supersymmetric models are for example one possible class of theories containing an extended Higgs sector. Supersymmetric models predict a symmetry between the fermions and bosons. In such models for each fermion there appears a bosonic super-partner and vice-versa. To impart mass to the up and down type quarks within a supersymmetric model an extended Higgs sector is required. This leads to the appearance of a charged Higgs boson.

This thesis presents a search for such a charged Higgs boson in the leptophobic decay channel to a quark and anti-quark pair, $H^+ \to c\bar{s}$ [2]. The search is performed in the $t\bar{t}$ system, replacing one W boson in a $t \to W^+ b$ decay with a H^+. The search uses 35 pb^{-1} of pp collisions collected by the ATLAS detector at the Large Hadron Collider in 2010.

The thesis is structured as follows. Firstly the theoretical background required to understand this search will be explored in Chapter 2. A description of the LHC and the ATLAS detector follows in Chapter 3. The ATLAS trigger and data distribution systems will then be described in Chapter 4. The techniques required to reconstruct the detector objects in events are outlined in Chapter 5. The analysis relies on the accurate modelling of the expected events by Monte Carlo simulation, this will be explained in Chapter 6. The event selection criteria along with the analysis techniques used will be introduced in Chapter 7. Chapter 8 will describe the systematic uncertainties that can influence the analysis. Statistical methods are required to determine the significance of any observed signal or to define the signal strength that can be excluded by the data. These techniques will be specified in Chapter 9. The results gained from the analysis will be presented in Chapter 10 and the conclusions drawn from them shown in Chapter 11.

[2] Charge conjugation of processes is assumed throughout this thesis.

Chapter 2

Theoretical Background

This chapter presents an overview of the theoretical information required to understand the search presented in this thesis. It will start by setting out the basic fundamentals of the Standard Model (SM), which is the current theory for fundamental particles and their interactions. The Standard Model is a long standing, heavily tested and successful theory. It has been described in extensive detail elsewhere [3, **?**]. Reasons why a theory beyond the SM (BSM) is required will be briefly explored in Section 2.2, specifically outlining extensions pertinent to this analysis. The chapter will end with a description of the decay channel explored in this thesis and the results from previous searches.

2.1 The Standard Model

The Standard Model is a relativistic quantum field theory describing the elementary particles of the universe and the interactions between them. In the theory quantum fields are defined describing two distinct types of particles. The first type are the spin $1/2$ fermions comprised of the quarks and leptons, which together form the elementary particles of matter. Interactions between the elementary particles are introduced by requiring that the Lagrangians of the quantum fields describing the fermions are invariant under gauge transformations in several symmetry groups. By enforcing invariance a set of vector fields are introduced. These fields describe the second type of particles, the integer spin bosons which are responsible for mediating the interactions between

	Quarks		
Generation	1^{st}	2^{nd}	3^{rd}
Particle	Up (u)	Charm (c)	Top (t)
Mass [GeV]	$1.7 - 3.1 \times 10^{-3}$	$1.29^{+0.05}_{-0.11}$	$172.9 \pm 0.6 \pm 0.9$
Charge [e]	$+\frac{2}{3}$	$+\frac{2}{3}$	$+\frac{2}{3}$
Particle	Down (d)	Strange (s)	Bottom (b)
Mass [GeV]	$4.1 - 5.7 \times 10^{-3}$	$100^{+30}_{-20} \times 10^{-3}$	$4.19^{+0.18}_{-0.06}$
Charge [e]	$-\frac{1}{3}$	$-\frac{1}{3}$	$-\frac{1}{3}$
	Leptons		
Particle	Electron (e)	Muon (μ)	Tau (τ)
Mass [MeV]	0.511	105.7	1777
Charge [e]	1	1	1
Particle	e neutrino (ν_e)	μ neutrino (ν_μ)	τ neutrino (ν_τ)
Mass [MeV]	$< 2 \times 10^{-6}$	< 0.19	< 18.2
Charge [e]	0	0	0

Table 2.1: The fermionic matter present in the Standard Model [4].

the fermions.

2.1.1 Matter

In total there are twelve fundamental fermions; six quarks and six leptons. The quarks undergo both strong and electroweak interactions which distinguishes them from the leptons which only undergo the latter. The particles are further separated into three generations of two fermions, shown in Table 2.1. The three generations all contain two quarks with electric charges of $+\frac{2}{3}$ and $-\frac{1}{3}$ for the up and down type quarks respectively. Each quark carries a baryon quantum number $\mathbf{B} = +1/3$ which is conserved in interactions. Additionally each quark flavour has its own quantum number. These flavour quantum numbers are conserved by both electromagnetic and strong interactions but not by the weak interaction.

	Gauge Bosons			
Force	EM	Electroweak		Strong
Particle	Photon (γ)	$W^{\pm}$	Z	Gluon (g)
Mass [GeV]	0	80.399	91.188	0
Charge [e]	0	± 1	0	0

Table 2.2: The gauge bosons present in the Standard Model [4].

For the leptons, each generation contains a charged lepton, for example the electron, and the corresponding neutral neutrino. The neutrinos were introduced to allow conservation of momentum in weak decays and until recently they were assumed to be massless. With the discovery of neutrino mixing it is now known that their masses cannot be zero. As they only interact via the weak interaction neutrinos are very hard to detect and escape most detectors unmeasured. Each lepton generation has its own quantum number L_e, L_μ, L_τ which are conserved except for in neutrino oscillations. All particles are observed to have an anti-particle with the same mass and spin, but with opposite non-zero quantum numbers.

2.1.2 Interactions

Four interactions between particles are observed in nature; the strong, electromagnetic, weak and gravitational forces. The gauge bosons which transmit each force are shown in Table 2.2. These gauge bosons arise in the theory by requiring that the Lagrangian of the theory is invariant under local phase transformations. An example of this idea is the derivation of Quantum Electrodynamics (QED) by requiring that the Lagrangian for a free electron is invariant under the local phase transformations of the U(1) gauge group. Requiring the invariance of the theory under such transformations gives rise to a quantum field A_μ which can be seen as a quantum field of massless photons mediating the electromagnetic force with a coupling equal to the fine structure constant, α. The photons of this field are required to be massless as the addition of a mass term to the Lagrangian would again break the gauge invariance.

The complete SM theory is required to be invariant under the gauge transformations of $SU(3)_C \otimes SU(2)_L \otimes U(1)_Y$. Each group is a representation of an underlying symmetry of the theory; weak hypercharge (Y), the left handed component of weak isospin (L) and colour (C). Requiring invariance under these groups leads to the manifestation of both the strong and electroweak forces and their gauge bosons.

Quantum Chromodynamics (QCD) requires that the theory is invariant under the $SU(3)_C$ gauge group. This leads to the appearance of the strong force mediated by the gluon; a massless gauge boson of the colour field introduced in a similar fashion to the photon in QED. Colour charge appears as a new conserved quantity which allows the strong force to occur. Colour interactions take place between colour charges much like electromagnetic ones do between electric charges, but with a coupling constant α_s. Quarks can now be labeled as having red (R), blue (B) or green (G) colour charge as well as anti colours ($\bar{\mathrm{R}}$, $\bar{\mathrm{B}}$, $\bar{\mathrm{G}}$). Gluons come in eight bi-colour states allowing them to carry colour charge between the quarks. Coloured particles are not observed in nature, this leads to the concept of colour confinement, the requirement that the observed particles are colour neutral. Therefore the now coloured quarks must be bound together by gluons into the colourless states observed in detectors, the hadrons. These states are formed from either two quarks in colour and anti-colour states (mesons) or three quarks one of each colour or anti-colour state (baryons). As gluons are colour charged themselves this leads to them being able to interact with other gluons via the strong force, unlike the photon. A combination of colour confinement and the self interaction of gluons via the strong force leads to quarks produced in collisions appearing as jets of hadronic particles in the detector. As quarks and anti-quarks separate the strength of the colour interaction between them increases. As the gluons can interact the colour force lines, shown in Figure 2.1, are squeezed into tube like regions. As the quarks separate the potential energy in the colour tube increases. This continues until the potential energy is large enough that the formation of a further quark and anti-quark, thus forming two shorter tubes, is energetically favourable. This continues until the system no longer has enough energy to produce quark and anti-quark pairs. Thus the initial quarks have metamorphosed into a jet of colourless mesons.

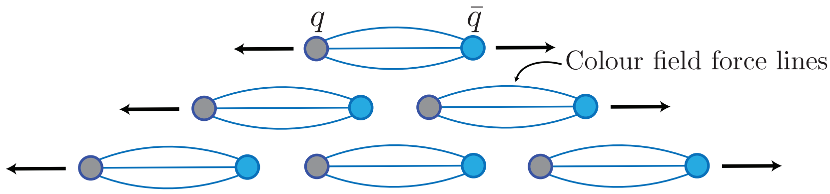

Figure 2.1: Diagram showing the formation of a jet of mesons from the separation of a quark and anti-quark pair.

The electroweak force is the unification of the weak and electromagnetic forces. In the SM it is brought about by requiring the invariance of the theory under $SU(2)_L \otimes U(1)_Y$. Requiring this invariance leads to four gauge bosons, the W^+, W^-, Z and the photon. As these gauge bosons were introduced by requiring the invariance of the theory under the transformation of a gauge group it is expected that they should be massless. The photon is is massless. The $W^\pm$ and Z bosons are however observed to have masses of 80.4 GeV and 91.2 GeV respectively [4].

2.1.3 Electroweak Symmetry Breaking and the Higgs

The SM now has a mass problem. It has two massless gauge bosons, the photon and gluon, as expected by requiring gauge invariance. By introducing the electroweak force in the same manner however it now has three unexpectedly massive bosons. Additionally, up until this point the theory has not explained the observed masses of the other fundamental particles. As pointed out previously, the direct addition of fermion Dirac mass terms of the form $\frac{1}{2}m^2\bar{\psi}\psi$ breaks the gauge invariance. Similarly direct addition of mass terms for the fermions breaks invariance as the $SU(2)_L$ operator only acts upon the left handed components of the fields. Instead of putting the mass terms for the electroweak gauge bosons in by hand they can be generated by a "spontaneous symmetry breaking" mechanism. This mechanism is known as electroweak symmetry breaking (EWSB).

An example of a spontaneous symmetry breaking is a pencil balanced upon its tip. Obviously the pencil is in a symmetric (if somewhat miraculous) meta-stable state. The system can be seen as having a symmetric state, on its point, and a set of degenerate ground state solutions, the possible directions of falling. It has the freedom to move in any direction; the slightest force will cause the pencil to fall. When the pencil falls, the symmetry of the system is now broken as a direction has been chosen. However the initial choice of direction did not matter; all choices of direction lead to equivalent states.

In the SM the EWSB is performed by the so called Higgs mechanism, although a multitude of theorists are credited with its discovery [5, 6, 7]. The Higgs mechanism spontaneously breaks the problematic $SU(2)_L$ symmetry. In doing so it gives mass to the gauge bosons and produces a surprise bonus. A simple way to visualise the symmetry breaking achieved by the Higgs mechanism is by using it to break a U(1) local gauge symmetry, such as the one in QED. A complex scalar field $\phi = (\phi_1 + i\phi_2) / \sqrt{2}$

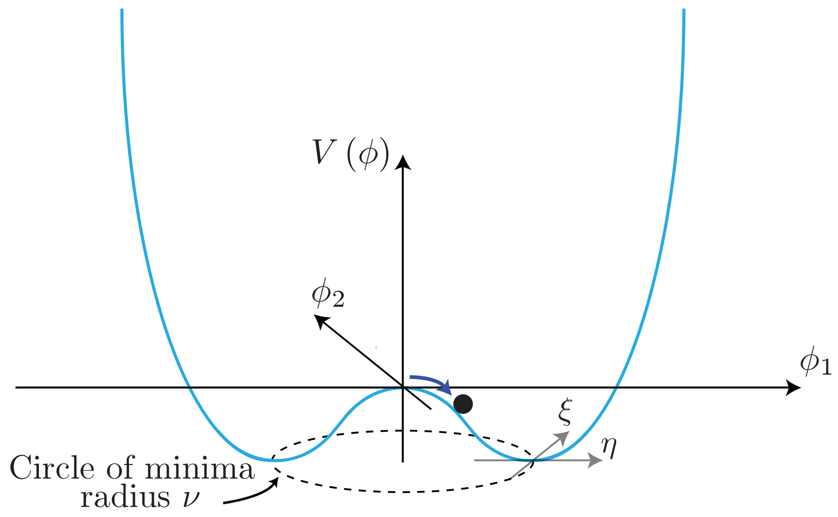

Figure 2.2: A diagram showing the Higgs potential $V(\phi)$ for a complex scalar field $\phi = (\phi_1 + i\phi_2) / \sqrt{2}$. A circle of minima are found at the vacuum expectation value centred on the origin. By moving to these new minima mass can be given to the particles of the SM.

can be added with a mass μ and quartic self coupling parameter λ. Using this field and defining a covariant derivative to maintain gauge invariance, additional terms appear in the Lagrangian representing the mass, $\mu^2\bar{\phi}\phi$, and self coupling, $\lambda(\bar{\phi}\phi)^2$, of the scalar field. If the mass parameter is set as $\mu < 0$ and the coupling parameter forced to be $\lambda > 0$ then the potential shown in Figure 2.2 is achieved for this new scalar potential,

$V(\phi)$. Here it can be seen that the origin no longer represents the minimum energy of the system. Instead there is a circle of minima of the potential $V(\phi)$ with a radius v, the vacuum expectation value, where v is given by,

$$\phi_1^2 + \phi_2^2 = v^2, \tag{2.1}$$

$$v^2 = -\frac{\mu^2}{\lambda}. \tag{2.2}$$

Clearly now there is a series of degenerate states around the circle of minima. The symmetry can now be broken by freely choosing a new minima position, for example $\phi_1 = v$, $\phi_2 = 0$. By expanding about this new minima in terms of the fields η, ξ, shown in Figure 2.2, the Lagrangian gains terms for a massless Goldstone boson ξ and a massive scalar η. The vector boson field A_μ also gains a mass term in this expansion. By making a further gauge translation it can be shown that the Goldstone boson can be absorbed as the longitudinal polarisation needed by the now massive vector gauge boson, A_μ. This now massive photon interacts with the surprise bonus of a massive spin-0 real scalar particle, the Higgs boson H. A massive photon is not needed to describe observations. However the process shows it is possible to spontaneously break a local gauge symmetry and thus provide mass to a vector gauge boson. In doing so a real Higgs boson is produced that can be hunted for in detectors.

The logic used to break the $U(1)$ gauge symmetry can be similarly applied to the $\mathrm{SU}(2)_L$ case. Instead of defining a single complex scalar field it becomes necessary to define an SU(2) doublet of complex scalar fields,

$$\phi = \begin{pmatrix} \phi_\alpha \\ \phi_\beta \end{pmatrix} = \sqrt{\frac{1}{2}} \begin{pmatrix} \phi_1 + i\phi_2 \\ \phi_3 + i\phi_4 \end{pmatrix}. \tag{2.3}$$

The new minima chosen in this case is one where $\phi_1 = \phi_2 = \phi_4 = 0$ and $\phi_3 = v$ thus defining the Higgs potential. Due to the presence of four fields in the SU(2) doublet of scalar fields there are now three scalar degrees of freedom from the Goldstone bosons which can be absorbed by the three gauge fields forming massive $W^\pm$ and Z particles. The aim of the process is now complete. The final scalar field is left once again to become a massive scalar Higgs boson. This scalar Higgs field can then in a similar fashion impart mass to the fermions. The Higgs field couples to particles with a strength proportional to the mass of the particle. The theory makes no predictions of the masses, which must be measured experimentally. The theory also makes no prediction of the mass of the new Higgs boson. The mass can however be related to the vacuum expectation value, v and self coupling constant λ via,

$$m_H^2 = 2v^2\lambda. \tag{2.4}$$

The vacuum expectation value v can be calculated to be 246 GeV [8][1], but λ is an unknown. Experimental searches for the SM Higgs have been performed for many years and massive advances have been made recently. A combination of the LEP experiments' results [9, 10, 11, 12] excluded the existence of a Higgs boson with a mass less than 114.4 GeV [13]. By the EPS conference in 2011 the Tevatron experiments had further expanded the excluded range to include a higher mass band between 156 − 177 GeV [14]. The LHC experiments also joined the hunt with a higher mass reach. Between ATLAS and CMS exclusion was achieved over the range from 155 − 210 GeV and 270 − 440 GeV [15, 16]. With the LHC accumulating data at a rapid pace the Higgs boson is rapidly running out of places to hide.

2.2 Extensions to the SM

If the Higgs boson, the final piece of the SM, is found, is this the end of particle physics? In short no. The SM has been a powerfully predictive theory standing up to years of experimental scrutiny. As powerful as it has been it still has a series of problems that it cannot resolve. To begin the theory from the outset is incomplete. Gravity, possibly the most macroscopically obvious force, is not included. Beyond this obvious omission there are some additional problems,

1. <u>The hierarchy problem.</u>

   The mass parameter of the Higgs field μ receives quantum corrections due to loop diagrams of the order the cut off scale for the Standard Model. As it is known that gravity has been omitted from the theory this scale λ can be set at the

[1] The simple calculation is $v = \left(G_F \sqrt{2}\right)^{-1/2}$.

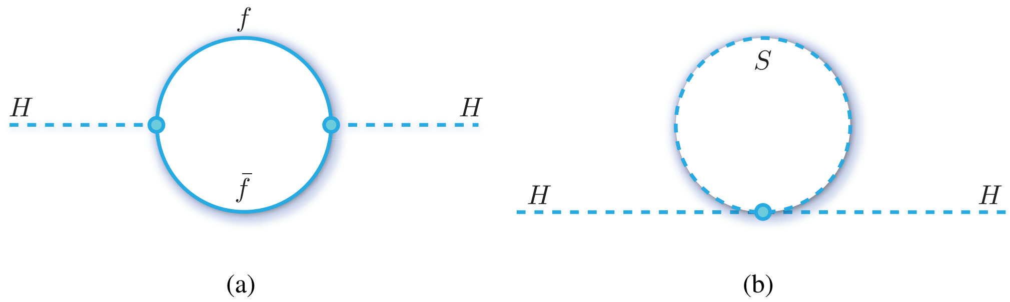

Figure 2.3: Feynman diagrams showing the quantum corrections to the squared Higgs mass parameter (μ^2) due to (a) a fermion and (b) a scalar particle.

Planck mass scale,

$$M_{Pl} = \sqrt{\frac{\hbar c}{8\pi G}}, \tag{2.5}$$

where it is expected that gravitons will start being important contributions to these corrections. From measurements of the top quark and W boson mass the Higgs mass is expected to be O (100 GeV) [1, 2]. It is therefore expected that $\mu^2 \approx -10^4$ GeV^2 however if the cut off is at the Planck scale then it receives corrections of the order $\Delta\mu^2 \approx -10^{35}$ GeV^2. To stop the Higgs mass being dragged up to the bare μ_0^2 mass at the Planck scale there must be a cancellation of the corrections provided by these diagrams of the $O\left(10^{31}\right)$ decimal places. This appears an unnatural level of fine tuning to impose on nature [17].

2. The mass hierarchy problem.

   There is an astonishing disparity between the lightest and heaviest observed quarks and leptons. The top quark is over 40 times more massive than its generational partner the bottom quark. As shown in the previous section the Higgs mechanism make no prediction for the masses of the fermions. The Yukawa couplings of the fermion fields to the Higgs scalar field are input parameters of the theory to be determined experimentally. A more satisfactory theory would explain not just how the particles gain mass, but make accurate mass predictions for them [18].

3. Dark matter.

   Various observations by astronomers suggest that "dark" matter dominates the matter present in the universe. Dark matter is so called as it does not interact electromagnetically and therefore does not absorb or emit light. Its existence is therefore inferred from the gravitational profiles of galaxies and gravitational lensing effects that are not explainable by the visible matter alone. Although neutrinos fit the profile of dark matter, they cannot provide enough missing mass and also would not clump around galaxies as required. The SM is therefore missing a candidate to reproduce cosmological observations [19, 20].

4. <u>Matter versus anti-matter asymmetry in the universe.</u>
   At the beginning of the universe it can be presumed that the baryon and lepton numbers were zero. Matter and anti-matter would then be pair produced leading to equal amounts of both. The present observed universe is however dominated by matter. An asymmetry is therefore required between the number of baryons and anti baryons leading to the abundance of matter seen today. The SM contains some CP-violation in the flavour sector, which leads to a small asymmetry between the decays of matter and anti-matter. However the size of the observed asymmetry is not enough to account for the density of matter observed today [21, 22].

These unanswered questions hint at unknown physics processes beyond the SM. Many candidate theories have be proposed to address some or all of these problems. The analysis presented in this thesis is associated with one of these theories, the Minimal Supersymmetric Standard Model. This model proposes extensions to the SM which aim to solve some of the problems outlined here.

2.2.1 Supersymmetry

In supersymmetry (SUSY) [23] an additional symmetry between bosons and fermions is introduced to the theory. It introduces an operator Q which converts bosons into fermions and vice-versa,

$$Q\,|\mathrm{Boson}\rangle = |\mathrm{Fermion}\rangle \quad \text{and} \quad Q\,|\mathrm{Fermion}\rangle = |\mathrm{Boson}\rangle\,. \tag{2.6}$$

By imposing such a symmetry upon the SM Lagrangian SUSY predicts that each SM particle will have a super-partner possessing an identical set of quantum numbers, but differing by a half unit of spin. Therefore for each SM fermion a supersymmetric bosonic partner is added identified by an prefixed s. For example the supersymmetric partner of the electron is the selectron. Similarly for every SM boson a supersymmetric fermionic partner will be introduced with an -ino suffix. For example the supersymmetric partner of the W is the Wino. At first glance, the instantaneous doubling of the number of particles is appears a very strange thing to do. Adding such a plethora of new particles brings more free parameters to the theory. SUSY should definitely solve some of the previous woes of the SM in return for such additions.

In exchange for the bounty of new particles, SUSY offers solutions to two of the problems outlined in the previous section. Firstly the inclusion of a set of super-partner particles adds additional loop corrections terms to the Higgs mass parameter. For each SM fermion loop correction the SUSY partner produces a scalar loop correction and vice-versa for the SM scalar loops. This leads to an exact cancellation of the SM contribution to the quantum corrections. This therefore leaves the Higgs mass stable under such corrections and not at the Planck scale. Here lies a problem however, these particles have never been observed in nature. The new super-partners would be obvious as they would have the same mass as their SM partners. To account for the fact that the super-partners have not been observed the symmetry must be broken to raise the masses of the SUSY particles to a higher scale. By breaking SUSY the mass degeneracy problem is solved. Unfortunately in doing so the exact cancellation of the quantum corrections is now lost as the SUSY particles running round the loop corrections now have different masses.

SUSY additionally offers a candidate dark matter particle if a property known as R-parity is conserved. R-parity is a multiplicatively conserved quantum number defined as,

$$P_R = (-1)^{3(\mathrm{B}-\mathrm{L})+2s}, \tag{2.7}$$

where B and L are the SM baryon and lepton numbers and s is the spin of the particle. The Standard Model particles and the Higgs bosons have $P_R = +1$, and the SUSY partners have $P_R = -1$. This leads to the fact that if R-parity is exactly conserved then every interaction vertex will contain an even number of sparticles. The lightest of the new SUSY particles by this logic will now be stable as it has no possible decay channels open to it. If this particle is neutral and only interacts weakly with normal matter then it offers an excellent dark matter candidate. Additionally R-parity conservation blocks decay channels that would cause proton decay of the order 10^{-2}s from occurring. As current limits on the proton lifetime are around 10^{34} years [24] such decays would be problematic to say the least.

The MSSM is an R-parity conserving SUSY implementation which contains the minimum number of additional particles to allow SUSY to be realised in nature. In the SM the Higgs field ϕ generates masses for the down type quarks and the conjugate field performs the same task for the up type quarks. In the MSSM however using complex conjugates in this manner is not allowed. The Higgs sector in the MSSM therefore needs to approach the problem of generating masses from a slightly different angle.

2.2.2 The Two Higgs Doublet Model

The simplest model for the Higgs sector which would allow the MSSM to generate masses for the both the up and down type quarks is a two Higgs doublet model (2HDM). In models of this type the Higgs sector responsible for breaking the $SU(2)_L$ symmetry contains two Higgs doublets instead of the single doublet found in the SM. The theory now has two vacuum expectation values (v_1 and v_2) one in each Higgs doublet. They are positioned in the MSSM Higgs doublets such that one couples to the down type and the other the up type quarks. These new vacuum expectation values are constrained to be equal to the SM value but the relative strengths are not constrained,

$$v_1^2 + v_2^2 = v_{SM}^2, \tag{2.8}$$

$$\tan\beta \equiv \frac{v_2}{v_1}. \tag{2.9}$$

The parameter $\tan\beta$ here describes the relative strength of the two Higgs vacuum expectation values. Any theory containing a two Higgs doublet model has eight fields contained in the two complex SU(2) doublets. The extra degrees of freedom mean that after the gauge bosons have been imbued with mass that the theory is left with not one but five massive Higgs bosons. Three of these bosons are electrically neutral (h, H and A) and two are charged ($H^{\pm}$). The phenomenology of the MSSM Higgs sector can be described in terms of one of the masses, usually chosen to be m_{A^0}, and $\tan\beta$, The analysis presented in this thesis will be a search for a light charged Higgs boson. Here light is deemed to be a charged Higgs with a mass less than the top quark. If $m_{H^+} < m_t$ then the decay $t \to H^+ b$ is possible, allowing for a H^+ signal to be found in the decay of $t\bar{t}$ pairs. The discovery of such a signal would be evidence for physics beyond the SM, or at the very least that the Higgs sector of the SM is not just a single SU(2) doublet. The

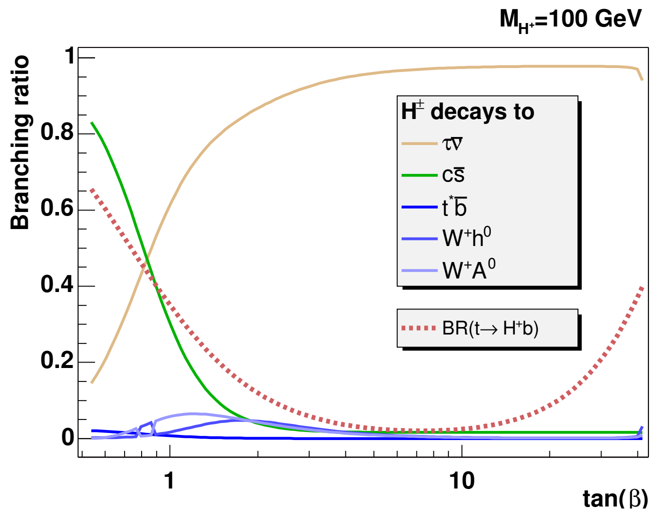

Figure 2.4: Diagram showing the expected decay branching ratios for a 100 GeV charged Higgs boson as a function of $\tan\beta$ [25, 26].

expected decay branching ratios for a 100 GeV charged Higgs boson in the MSSM are shown in Figure 2.4. For most of the $\tan\beta$ range, decays of the form $H^+ \to \tau\bar{\nu}$ are the dominant decays. At low $\tan\beta$ there is a significant decay contribution from the $H^+ \to c\bar{s}$ channel. This decay channel will be the mode explored in this analysis.

Although the 2HDM model is naturally required in the MSSM, the arrangement of the vacuum expectation values in the doublets is constrained by the SUSY requirements. There is in fact nothing preventing the SM containing a two Higgs doublet Higgs sector. It is merely not the simplest available solution. Other arrangements of the vacuum expectation values in the two doublets are possible outside the constraints of the MSSM. In these models [27] the decay $H^+ \to c\bar{s}$ can be enhanced across a wider range of $\tan\beta$ values.

2.3 Top Quark Physics

The search for a light charged Higgs boson is performed in $t\bar{t}$ decays at ATLAS. Therefore to understand the analysis an overview of the SM $t\bar{t}$ system is necessary. Production of $t\bar{t}$ events in pp collisions at $\sqrt{s} = 7$ TeV has a theoretical cross section of $164.6^{+11.4}_{-15.7}$pb [28]. By comparison, at the Tevatron,which produces $p\bar{p}$ collisions at $\sqrt{s} = 1.96$ TeV, the cross-section is $7.27^{+0.76}_{-0.85}$pb [29], a factor of over twenty smaller than at current LHC energies. With such a large increase in cross-section the LHC can be considered a top factory. The current measured cross sections from ATLAS and CMS are $174 \pm 6(stat)^{+16}_{-14}(sys) \pm 9(lum)$pb [30] and 158 ± 19pb [31] respectively. Both experiments results are consistent with the theoretical prediction. The main $t\bar{t}$ production mode at $\sqrt{s} = 7$ TeV is via gluon-gluon fusion, with a lower fraction produced via quark anti-quark annihilation. The reverse case was true at the lower energies of the Tevatron. The LO production modes are shown in Figure 2.5.

Top quarks have a lifetime of $5{\times}10^{-25}$s and therefore are the only quarks which decay before they hadronise. The top quark decays via $t \to W^+b$ with a branching ratio $\mathcal{B} = 99\%$. The decay channels of the SM $t\bar{t}$ system can be categorised by the decays of the two W bosons present in the system. The W bosons can either decay leptonically to a lepton-neutrino pair or hadronically to two quarks, which typically produces a dijet system.

Shown in Figure 2.6 are the three main groups of $t\bar{t}$ decays, which are;

1. Fully hadronic: both W bosons decay hadronically.

2. Semi-leptonic: one W decays leptonically, the other hadronically.

3. Dileptonic: both W bosons decay leptonically.

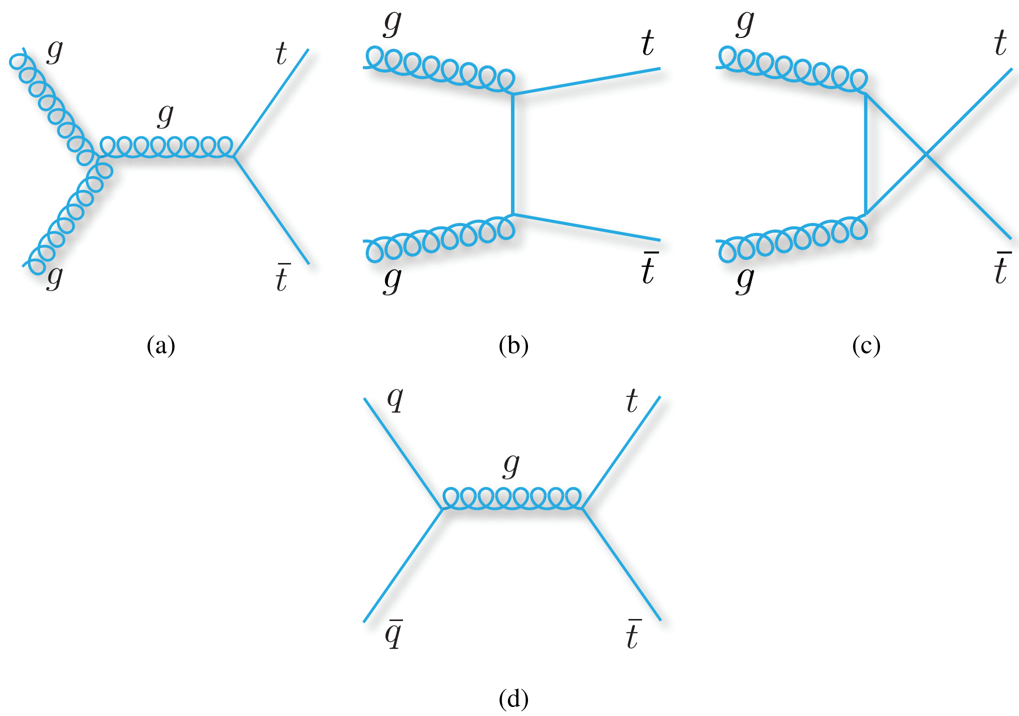

Figure 2.5: Diagrams showing he leading order production modes for $t\bar{t}$ pairs via (a, b, c) gluon-gluon fusion and (d) quark anti-quark annihilation,

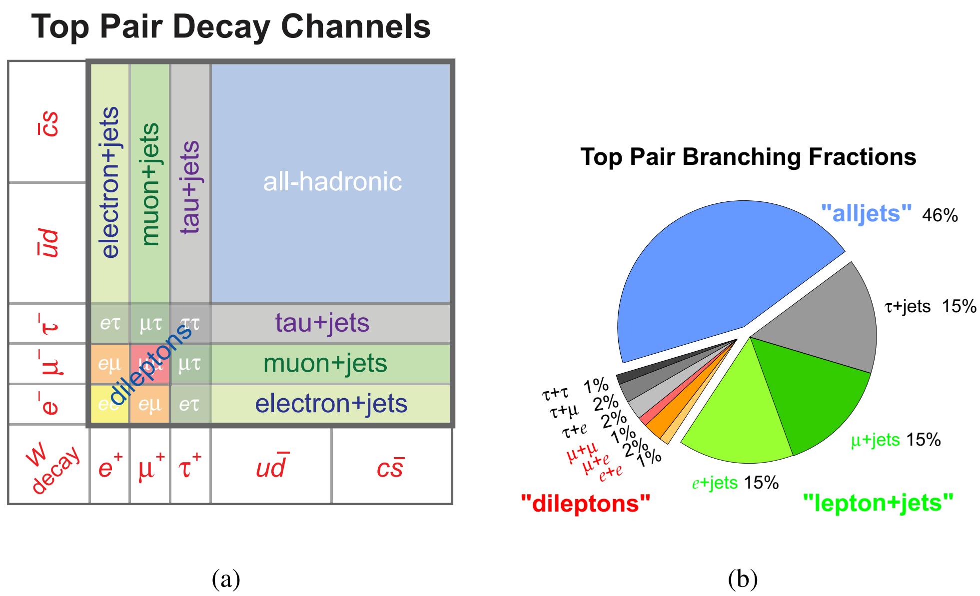

Figure 2.6: Diagrams showing the decay channels for $t\bar{t}$ decays, (a) shows the separate decay channels, (b) explicitly shows the branching ratio for each channel

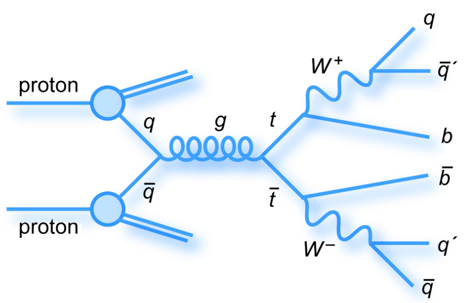

Figure 2.7: Feynman diagram showing the fully hadronic $t\bar{t}$ decay channel.

The fully hadronic channels have the largest individual branching fraction with 46% of all $t\bar{t}$ decays going to six jets including two b-jets, as shown in Figure 2.7. This channel has the advantage of containing no neutrinos and therefore can be fully reconstructed. However it proves hard to distinguish from a large QCD multi-jet background which has very similar kinematics only separated by the multiple b-jets. Additionally ascertaining the correct jet to parton assignment is difficult with six jets in the events.

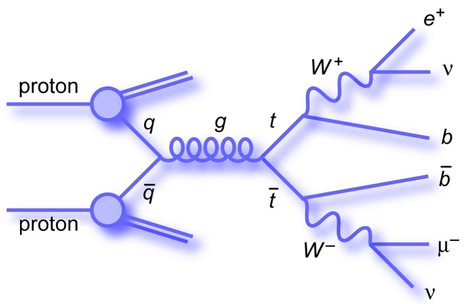

Figure 2.8: Feynman diagram showing the dileptonic $t\bar{t}$ decay channel.

The dileptonic channels have the smallest branching fraction at 9%, with two lepton-neutrino pairs and two b-jets, as shown in Figure 2.8. This channel has the advantage of a very clean signal with two isolated leptons and two b-jets giving a strong rejection against backgrounds. However it suffers from the fact that it contains two neutrinos, making it impossible to reconstruct the system fully.

The semi-leptonic channels lay between the two extremes with the $t\bar{t}$ system decaying to a lepton-neutrino pair, two light jets and two b-jets, as shown in Figure 2.9.

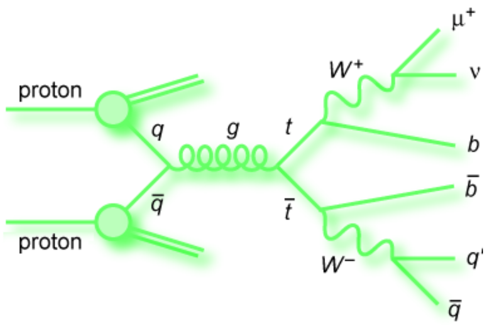

Figure 2.9: Feynman diagram showing the semi-leptonic $t\bar{t}$ decay channel.

They account for 45% of $t\bar{t}$ decays. The semi-leptonic channel can be distinguished from the QCD multi-jet background by a high p_T lepton and $E_{\mathrm{T}}^{\mathrm{miss}}$ requirements, an advantage over the fully hadronic channel. Using the known W boson mass, the neutrino p_z can be calculated and therefore the event can be fully reconstructed. This is an advantage over the dileptonic channel. The full neutrino momentum calculation is shown in Appendix B. Prior to considerations related to H^+ decays the semi-leptonic $t\bar{t}$ channel is already a favourable decay to work with offering an fully reconstructable event which can be easily triggered upon.

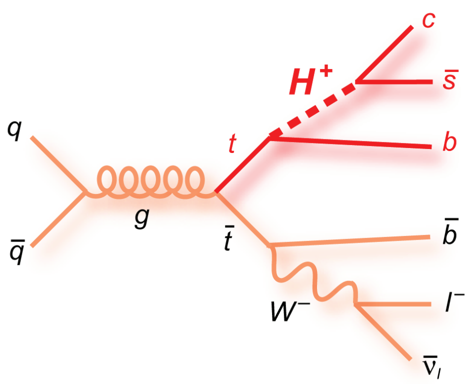

Figure 2.10: Feynman diagram showing the semi-leptonic $t\bar{t}$ decay channel with a H^+ boson decaying to $c\bar{s}$. This is the signal searched for in this analysis.

The search presented here aims to discover an anomalous decay of a top quark, $t \rightarrow H^+b$. If a charged Higgs can be formed in such a decay, then two new $t\bar{t}$ decay modes are made available $t\bar{t} \rightarrow H^{+}bW^{-}\bar{b}$ and $t\bar{t} \rightarrow H^{+}bH^{-}\bar{b}$. In this analysis the $\mathcal{B}(H^{+} \rightarrow c\bar{s})$ is assumed to be 100% with the aim of measuring or setting limits on the $\mathcal{B}(t \rightarrow H^{+}b)$. The channel containing two charged Higgs bosons would therefore produce a fully hadronic $t\bar{t}$ event. These events would prove hard to trigger on and if $\mathcal{B}(t \rightarrow H^{+}b) \approx 10-20\%$ then the branching fraction for $t\bar{t} \rightarrow H^{+}bH^{-}\bar{b}$ would be small at $\approx 1-4\%$. The fully hadronic search channel is therefore not favoured. The decay channel containing the single charged Higgs, however, includes the semi-leptonic final state corresponding to the leptonic decay of the W boson. This final state provides a lepton in the event to trigger on. This analysis will therefore use semi-leptonic $t\bar{t}$ events to search for the decay $t\bar{t} \rightarrow H^{+}b\ W^{-}\bar{b} \rightarrow c\bar{s}b\ l\nu\bar{b}$, as shown in Figure 2.10. The presence of a charged Higgs in the sample will alter the kinematic distributions from the SM expectations. The H^{+} is expected to be heavier than the W boson from previous limits from LEP [32, 33, 34, 35]. Therefore the hadronic b-jet spectrum will be softened as the H^{+} requires more energy from the top to be produced. A dijet mass distribution can be formed from the hadronically decaying boson in the top decays. If a charged Higgs signal is present then this distribution will gain a second peak from the new $H^{+} \rightarrow c\bar{s}$ decays at the $m_{H^{+}}$. This secondary peak is the H^{+} signal which this analysis aims to find. The following chapters will outline how this search is performed and the results gained. Similar searches have already been performed at CDF [36] and D0 [37] at the Tevatron. They set upper limits on $\mathcal{B}(t \rightarrow H^{+}b)$ in the region of $\approx 10-30\%$ as shown in Figure 2.11. The D0 result searched for deviations from the expectated SM top decay branching ratios due to the presence of a charged Higgs boson. The CDF analysis followed a similar methodology to the one presented in this thesis, searching for a secondary mass peak in the dijet mass distribution. This analysis aims to be competitive with these existing limits but using a much smaller data set.

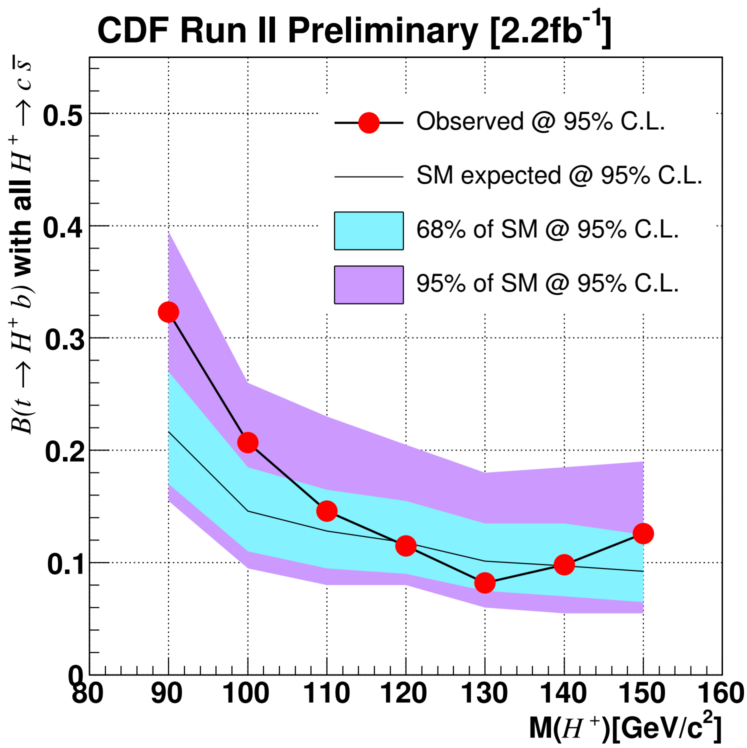

(a)

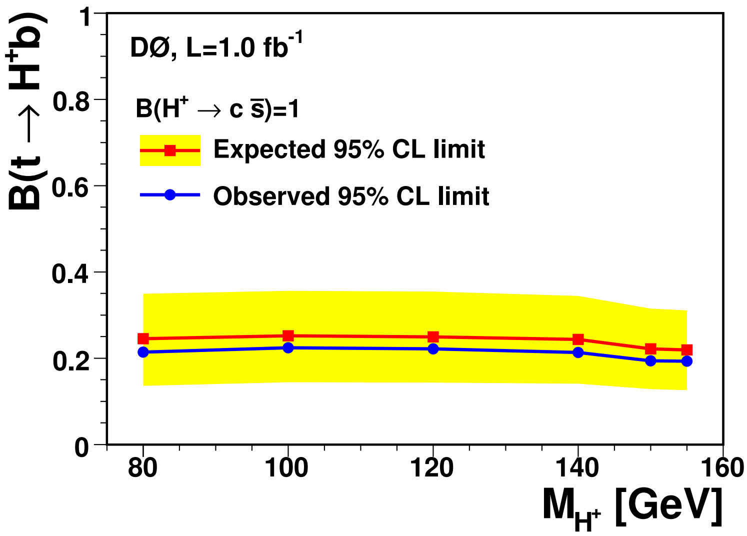

(b)

Figure 2.11: Plots showing the limits on the $\mathcal{B}(t \to H^+b)$ found by (a) CDF with 2.2 fb^{-1} [36] and (b) D0 with 1.0 fb^{-1} [37].

Chapter 3

Experimental Apparatus

3.1 Large Hadron Collider, LHC

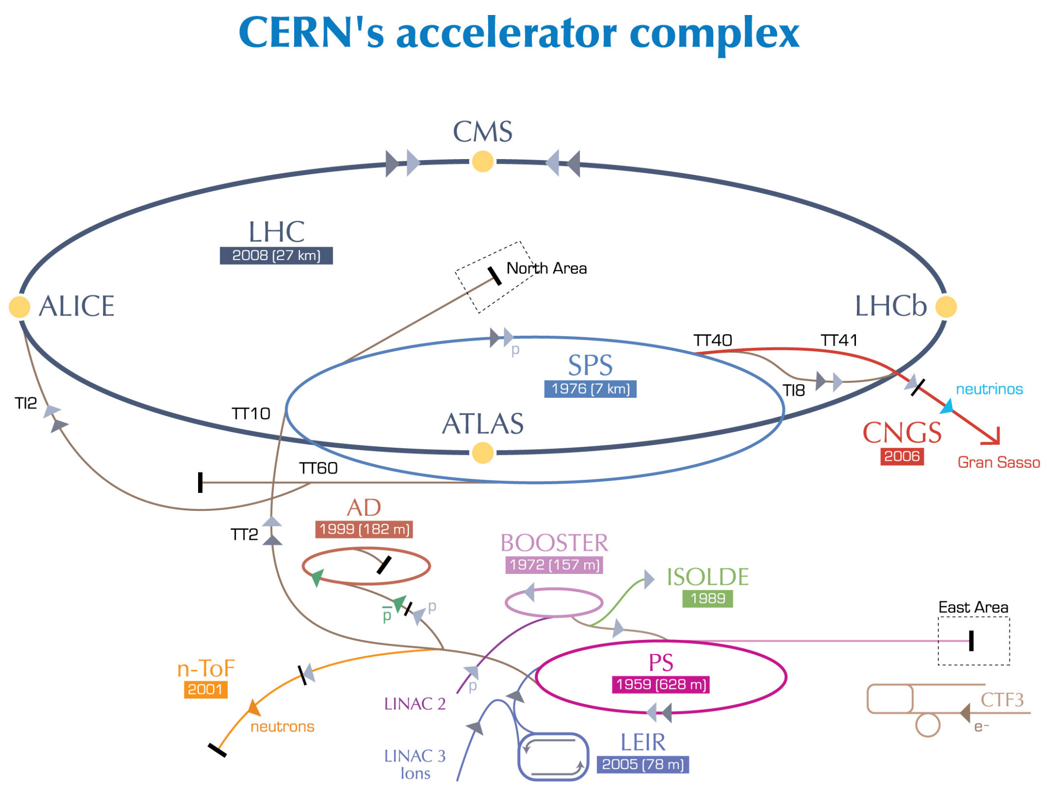

Figure 3.1: The layout of the accelerator structures and experiments present at CERN[38].

The Large Hadron Collider (LHC) [39] is the highest energy hadron accelerator and collider facility in the world, providing proton-proton collisions at $\sqrt{s} = 7$ TeV. It is located approximately 100 m underground in a 27 km circumference tunnel, at CERN near Geneva on the Franco-Swiss border. The LHC is the final stage of an accelerator complex consisting of a linear accelerator (LINAC) followed by a series of synchrotrons, shown in Figure 3.1. This complex accelerates protons from rest to the current maximum energy of 3.5 TeV. The protons are initially accelerated from an ion source to 50 MeV by the LINAC 2 which injects them into the Booster. This small synchrotron boosts the protons up to 1.4 GeV to feed them into the Proton Synchrotron (PS). The PS then accelerates the protons up to 26 GeV and feeds them into the Super Proton Synchrotron (SPS). The SPS is the last energy increase before the main LHC ring, bringing the energy up to the 450 GeV injection energy of the LHC. The SPS injects the clockwise and anti-clockwise beams into the LHC down the T12 and T18 transfer lines. The LHC itself consists of two separate evacuated beampipes contained within a series of liquid helium cooled superconducting electromagnets. The beampipes each have their own Radio Frequency (RF) cavities which accelerate the protons using a standing wave with a frequency timed to give the protons a small kick of energy as they pass by. Two main types of magnet are used within the LHC, large superconducting dipoles to guide the beams round the curvature of the machine and quadrapoles to focus and squeeze the beam size. The proton beams are not continuous but are filled into the main LHC ring in up to 2808 bunches each containing of order 10^{11} protons. The spacing of the bunches in the ring is defined by the harmonics of the full accelerating complex. The bunches need to be placed in time with the rise of the RF cavities to allow acceleration. In addition the bunches need to be positioned so they can be brought into collision at each interaction point around the ring. The beam energy is ramped up by the RF cavities from 450 GeV to the current full beam energy of 3.5 TeV. As the beam energy is increased the magnetic fields of the dipole magnets have to be synchronously ramped from 0.53T at injection energy to around 4T at the full beam energy to continue the bending of the beam around the LHC. At the end of the ramp the optics of the machine squeeze the beams' sizes at the interaction points ready to be collided at the four main experiments around the ring: ATLAS, ALICE, CMS and LHCb.

The purpose of the LHC is to deliver proton-proton collisions at the highest energy ever explored to search for new physical phenomena. The event rate of a physics process, R, is the product of the cross section of the process, σ, at the machine's centre of mass energy and the instantaneous luminosity of the machine, $\mathcal{L}_0$, which describes the intensity of the beam delivered,

$$R = \mathcal{L}_0\sigma. \tag{3.1}$$

$\mathcal{L}_0$ is defined in terms of the beam parameters;

$$\mathcal{L}_0 = \frac{N_b f_r n_1 n_2}{4\pi\sigma_x\sigma_y}, \tag{3.2}$$

where N_b is the number of bunches in each beam, n_1 and n_2 are the proton intensities of each beams bunches, f_r is the frequency of revolution of the bunches and σ_x and σ_y together describe the transverse beam size. Total integrated luminosity, L, is a measure of the amount of data recorded and is measured in units of pb^{-1}. The beam size can also be defined in terms of two LHC machine parameters, the transverse emittance, ϵ, and the amplitude function, β. The transverse emittance is a constant of the beam fixed at the proton source and the amplitude function is a measure of the magnet configuration seen as the beam travels round the ring. They are related by the function,

$$\epsilon = \frac{\pi\sigma_x\sigma_y}{\beta}, \tag{3.3}$$

so to achieve a small transverse beam size, therefore increasing the luminosity, the value of β at the interaction point, β^*, needs to be as small as possible. This is constrained by how close focussing magnets can be placed to the interaction point without interfering with the detector systems. To achieve a high luminosity a pp collider machine should aim to have a large number of bunches, each with high proton populations produced at a low emittance. These bunches should then be squeezed at the interaction point into a small transverse area. Finally a high collision frequency of these bunches will increase the luminosity delivered.

3.2 A Brief History of the LHC

The LHC has been many years in the planning, having first been approved as a project in 1994. It was initially designed to collide proton beams at $\sqrt{s}$ = 14 TeV with a design luminosity of $10^{-34}cm^{-2}s^{-1}$. This would provide physics reach into an energy regime far above the Tevatron, a long running $p\bar{p}$ collider at $\sqrt{s}$ = 1.96 TeV at Batavia, Illinois in the USA. After a number of hard years of research, development and construction, the LHC first circulated a proton beam on the morning of September 10th 2008. Operational testing of the machine then set off at a rapid pace with everything running smoothly until nine days later when there was an 'incident'. A faulty electrical bus connection between two dipole magnets experienced an increase in resistance which led to an electrical arc over the faulty bar. The liquid helium enclosure was punctured releasing 6 tonnes of He into the tunnel displacing surrounding magnets and physically damaging 53 magnets. After the 'incident' it was necessary to warm up the LHC for repairs to the damaged sector and to install additional protection systems to prevent a repeat of the incident. This process took the best part of a year and it was not until November 2009 that 450 GeV beams were once again circulating in the LHC being brought to collision on the 23rd.

The beams energies were carefully ramped up and on the 30th of March 2010 collisions at $\sqrt{s}$ = 7 TeV were achieved. The reduced energy was a decision made to reduce the stress on the bus connectors by not running the magnets at full power. The LHC then ran through until the start of November delivering 48pb^{-1} of data at an instantaneous luminosity of the order $10^{-32}cm^{-2}s^{-1}$, shown in Figure 3.2. It was this data set which was used to obtain the results presented in this thesis. Following the successful 2010 pp run the LHC switched to colliding lead ions for ALICE (along with ATLAS and CMS) to analyse. Arguably the most interesting results of the year were gleaned from this data with hints of jet quenching [40] seen for the first time shortly before the LHC shut down for the Winter. In 2011 the LHC team set themselves the task of delivering 1 fb^{-1} of $\sqrt{s}$ = 7 TeV data by the end of the year. Proton physics runs restarted on March 1st and by June 14th the machine had already surpassed this target. The LHC is still running efficiently and by August 2nd had delivered an integrated luminosity of

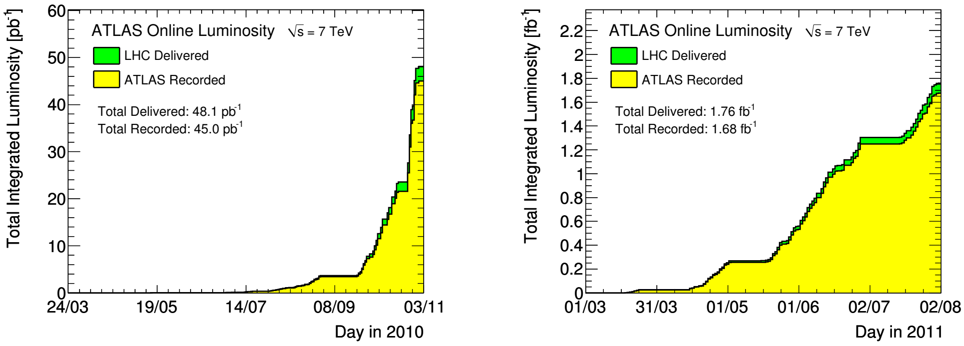

(a) (b)

Figure 3.2: Plots showing the cumulative luminosity delivered by the LHC and the amount recorded by ATLAS in (a) 2010 (48.1 pb^{-1} delivered and 45 pb^{-1} recorded) (b) 2011 1.76 fb^{-1} delivered and 1.68 fb^{-1} recorded). This analysis uses the 45pb^{-1} recorded in 2010.

1.76 fb^{-1}. It is intended for the proton run to again continue through until November. Time will tell if this is the year that the LHC experiments show the first signs of new physics.

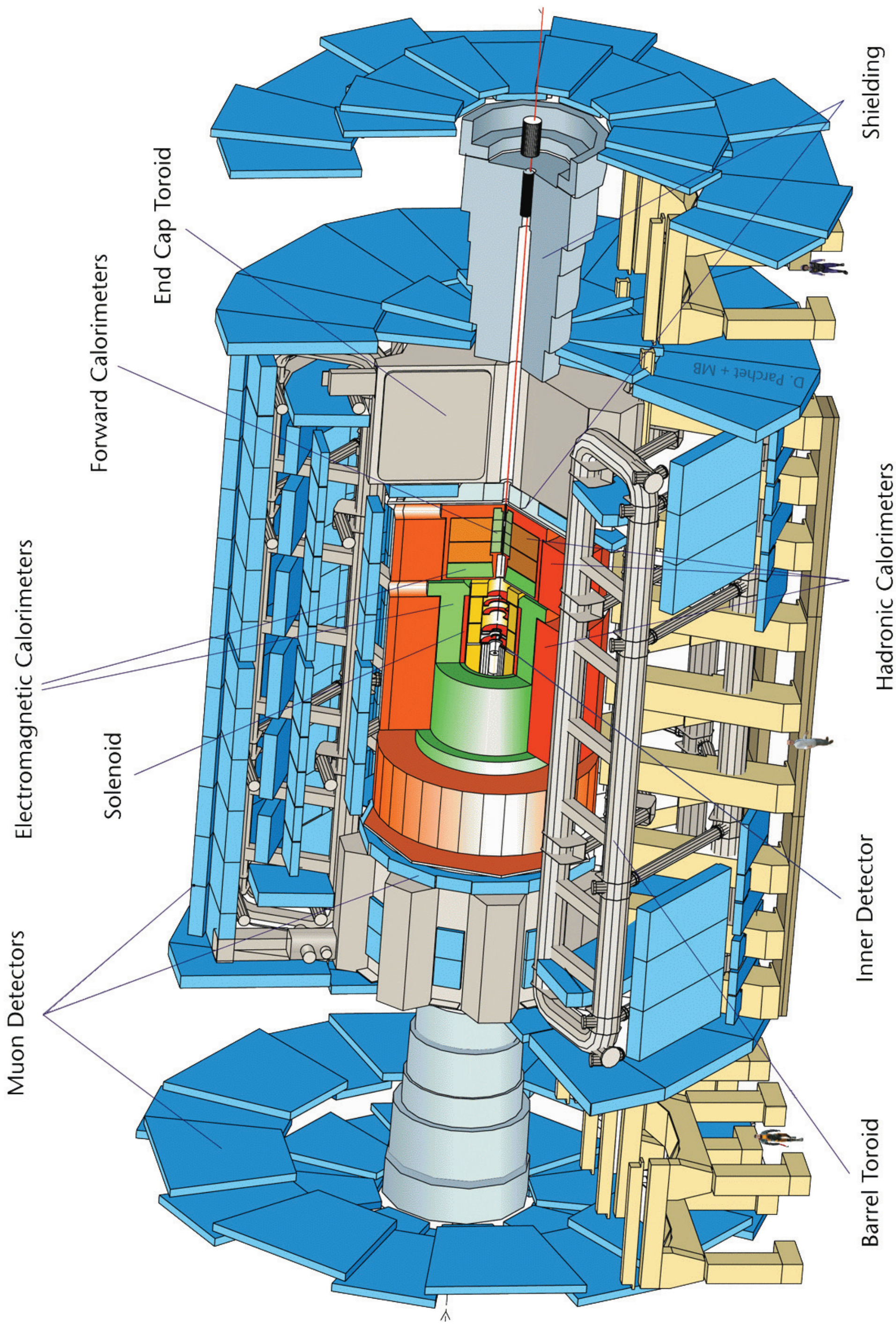

Figure 3.3: Diagram showing the main subdetectors of the ATLAS detector [41].

3.3 ATLAS

The ATLAS [42] detector, shown in Figure 3.3 is the largest of the general purpose detectors at the LHC. ATLAS is situated approximately 100 m underground at the point 1 experimental cavern at the LHC, as shown in Figure 3.1. It fills the experimental cavern, with a total length of around 46 m and a diameter of about 25 m. The total weight of the detector is approximately 7000 tonnes. The aims of the ATLAS detector are in short to test Standard Model predictions at LHC energies, discover the SM Higgs boson if it is realised in nature and to detect any BSM physics manifesting itself at LHC energies and intensity. Possible examples of BSM physics include supersymmetry, extra-dimensions or technicolor. The final states of these searches will generally contain SM particles, so accurate particle identification and measurement is the main aim of ATLAS.

The detector layout is constrained by these physics requirements, the main considerations are given below:

1. The whole detector is required to use fast and radiation hard electronics to survive the LHC environment: high-energy, high-flux radiation at short bunch crossing spacings.

2. The sub-detectors are required to have a high granularity to cope with high multiplicity events resulting from multiple parton interactions and pileup. Pileup occurs when the detector is simultaneous reading out information from more than one primary hard scatter interaction. Pileup can arise from multiple pp interactions in the same bunch crossing, in-time pileup, or from adjacent bunch crossings, out-of-time pileup. This of the utmost importance at the centre of the detector.

3. At the centre of the detector, charged particle tracking requires good momentum resolution and reconstruction efficiency. Vertex detectors close to the interaction point (IP) are needed to observe secondary vertices and thus tag τ leptons and b-jets.

4. Very good electromagnetic calorimetry is required to correctly identify electrons and photons and measure their energies.

5. Good hadronic calorimetry is required to measure the energy of jets formed from the hadronisation of quarks.

6. Good muon identification and momentum resolution is required from a detector surrounding the tracking and calorimetry as muons will traverse these regions as minimum ionising particles.

7. An almost fully hermetic detector design is necessary for each sub-detector to contain the entire collision event and allow for the precise calculation of missing transverse energy expected from neutrinos escaping the detector undetected. Missing transverse energy is taken to be the negative transverse vector sum of all energy deposits in the detector.

8. Large and stable magnetic fields are required for the inner detector and muon trackers to bend charged particles providing accurate momentum measurements.

9. Highly efficient triggering on high transverse-momentum objects is needed to provide a stable trigger and data taking rate while selecting events containing the physics processes of interest.

ATLAS attempts to meet these requirements by following the established design of a general purpose detector; a high granularity inner detector for tracking surrounded by electromagnetic and hadronic calorimetry which are in turn encompassed by a muon spectrometry system. Each main sub-detector consists of a barrel and endcap region to provide central and forward coverage. A solenoid provides the magnetic field for the inner detector while three air core toroid magnets provide the bending in the muon system. A three level triggering system is implemented to reduce the data taking rate from the nominal bunch crossing rate of 40MHz down to 200Hz. The full detector will be described in the following sections. The trigger system will be outlined in Chapter 4.

3.4 The ATLAS Coordinates

The ATLAS coordinate system defined here will be used throughout the thesis. The origin of the coordinate system is defined as the nominal interaction point at the centre of the detector. The beam direction defines the z-axis, and the $x - y$ plane is the plane transverse to the beam direction. The positive x-axis points towards the centre of the LHC ring and the positive y-axis points directly upwards from the interaction point. The positive z-axis points down the beam pipe towards LHCb on the LHC ring. It is often more useful to define a cylindrical polar coordinate system. The azimuthal angle, ϕ, is measured in the $x - y$ plane and the polar angle, θ, is between the the z-axis and the $x - y$ plane. Pseudorapidity is defined as,

$$\eta = -\ln \tan\left(\frac{\theta}{2}\right), \tag{3.4}$$

and is only dependent on the polar angle of a particle's trajectory and not its energy. It can also be defined in terms of momentum,

$$\eta = \frac{1}{2}\ln\left(\frac{|\mathbf{p}| + p_z}{|\mathbf{p}| - p_z}\right), \tag{3.5}$$

differing from the true rapidity, y, by taking the relativistic approximation that the particle's mass is negligible. Pseudorapidity is usually taken to define the polar angle in the detector as it is invariant under Lorentz-boosts along the z-axis. Transverse momentum, p_T, is defined in the $x - y$ plane as,

$$p_T = \sqrt{p_x^2 + p_y^2}, \tag{3.6}$$

and all other transverse objects such as the transverse energy, E_T, and missing transverse energy ($E_{\mathrm{T}}^{\mathrm{miss}}$) are all defined in a similar fashion. It is often useful to define the distance between two particles in the detector in terms of η, ϕ space,

$$\Delta R = \sqrt{\Delta\eta^2 + \Delta\phi^2}. \tag{3.7}$$

This object is useful in defining overlaps between objects in the detector or for matching hits at the boundary between two sub-detectors.

3.5 Magnet Systems

There are two main magnet systems incorporated into the ATLAS detector, a central solenoid (CS) and the air-core toroids. The CS surrounds the inner detector and provides it with a 2 T magnetic field to bend charged particles within the inner detector. The air-core toriods are arranged as two endcap toriods (ECT) and one central barrel toroid (BT) providing on average 1.0 and 0.5 T fields respectively to the muon spectrometers. All magnet systems are superconducting and therefore cooled by liquid helium, provided by a dedicated cryostat system, to 4.5K.

3.6 Inner Detector

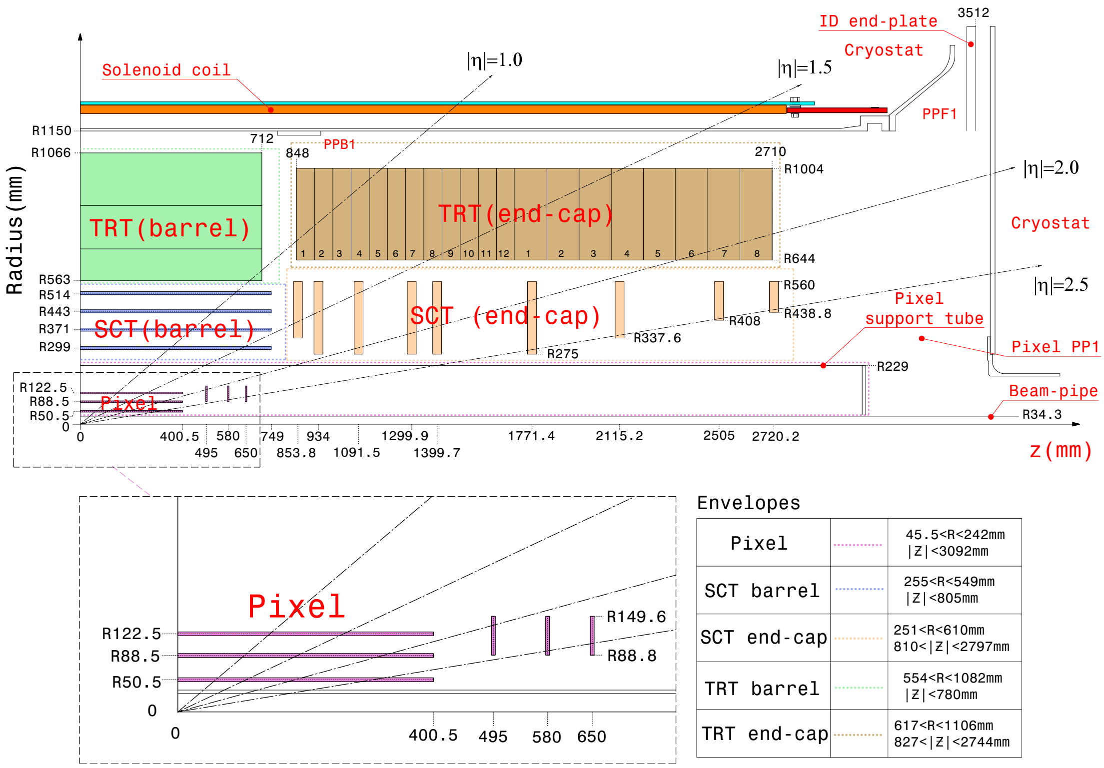

Figure 3.4: Diagram showing the layout of the inner detector sub-detectors around the nominal interaction point [41].

The inner detector (ID), shown in Figure 3.4, is the core of the ATLAS detector. It is the smallest sub-detector of ATLAS with a total radius of 115 cm and a total length of just over 7 m. Its functions are to provide high-resolution momentum measurements of charged particle tracks in the central region, $|\eta| < 2.5$, and to provide primary and secondary vertex measurements. The ID is made up of three different detectors; the pixel detector, the semi-conductor tracker (SCT) and the transition radiation tracker (TRT). Each provides multiple space points, or hits, from which to form particle tracks. The detectors all consist of three sections, two endcaps and one barrel thus giving hermetic coverage around the interaction point. Together these detectors provide on average 48 hits per particle. Together they aim to minimise the amount of material used to reduce the number of coulomb-scattering interactions and photon conversions. Therefore the total thickness of the inner detector is between $\approx 0.5-2$ radiation lengths (X_0) depending on η. These design features allow for precise track reconstruction and momentum calculation from the track's radius of curvature in the solenoid field. The resolution on the inverse momentum of the track, $1/p_T$ has been modelled in Monte Carlo studies using the following parameterisation,

$$\sigma_{\frac{1}{p_T}} = \sigma_\infty \text{ TeV}^{-1}\left(1 + \frac{\sigma_{\text{MS}} \text{ GeV}}{p_T}\right) \tag{3.8}$$

where the first term gives the expected resolution at infinite momentum and the second term gives the multiple scattering contribution. In a subset of the central barrel region ($0.25 < |\eta| < 0.5$) where the track traverses the minimal amount of material the resolution components are $\sigma_\infty = 0.34$ TeV^{-1} and $\sigma_{\text{MS}} = 44$ GeV. In the endcap regions ($1.50 < |\eta| < 1.75$) where near the maximum amount of material is crossed the resolution worsens to $\sigma_\infty = 0.41$ TeV^{-1} and $\sigma_{\text{MS}} = 80$ GeV[41]. The material crossed can be seen in Figure 3.4.

3.6.1 Pixel Detector

The pixel detector provides high-granularity and high-precision measurements close to the IP. It provides;

1. Full coverage up to $|\eta| = 2.5$.
2. Three high-precision space point measurements per track.

3. Aid to the primary vertex reconstruction of charged tracks with a resolution in the z-coordinate of < 1 mm.

4. Precise transverse impact parameter resolution of around 15 μm.

5. Good secondary vertex reconstruction.

With this information algorithms can be used to identify or "tag" short lived particles such as B hadrons and τ leptons.

It consists of three layers of silicon pixel detectors at radii of 5, 9 and 12 cm in the barrel region and three endcap discs extending radially from 9 cm to 15 cm at different points in z. The whole assembly has a total active area of silicon of 1.72 m^2. The ID contains 1744 pixel modules, 1456 in the barrel and 288 modules between the two endcaps. Each module contains 47232 pixel elements providing an active area of 60.8×16.4 mm^2. The majority of nominal pixels are 400 μm by 50 μm with some larger pixels included to maintain sensitivity between readout chips. In total 46080 channels are read out per module one column at a time by 16 readout chips bump bonded directly onto each module. There are in total around 67 million channels in the barrel and about 13 million in the endcap regions. The pixel detector's total of 80 million channels accounts for approximately 50% of the total channels read out by ATLAS. These complex electronic systems are also required to be radiation hard. They are expected to withstand dosages of 500 kGy at the inner most layer, whilst still maintaining a high quality tracking performance over a lifetime of at least 10 years. To achieve a constant performance the bias voltage applied will be increased from 150 V to 600 V to maintain the depletion zone as radiation damage increases.

3.6.2 Semi-Conductor Tracker

The SCT encloses the pixel detector and uses silicon strip detectors to providing further space points to form a track at a reduced monetary cost relative to a larger pixel detector. It consists of four cylinders in the barrel region and nine discs in each endcap region providing at least four precision space-point measurements up to $|\eta| = 2.5$. The barrel contains 2112 identical modules and between the two endcaps there are

1976 modules made up of three types depending on their position. In total the SCT contains 63 m^2 of silicon detectors. A strip sensor alone can only provide a position measurement in one direction. Therefore these sensors are attached back to back with a small angle of 40 mrad between them to solve any ambiguities and provide a full space point. Again as radiation damage increases it is expected that the bias voltage will be increased from 150V to 350V to maintain the depletion zone. Both the SCT and pixel detectors operate at temperatures between 0°C and -7°C, maintained by an environment of dry nitrogen gas.

3.6.3 Transition Radiation Tracker

The TRT completes the ID and is comprised of thin-walled proportional drift tubes or 'straws'. It contains 96 modules in the barrel region comprised of axially orientated straws and 20 wheels in the endcap regions with radially aligned straws. This design guarantees that particles traversing the TRT will cross 35-40 straws in the region $|\eta| < 2$. It therefore provides a large number of additional space points which can be used to provide enhanced pattern recognition for tracking at larger radii of the ID. The tubes are 4 mm in diameter with thin tube walls and contain 31 μm thick gold coated tungsten anode wires surrounded by a Xenon gas mixture. Particles traversing the tubes ionise the gas. The known drift time for the charge to be collected allows a drift circle to be defined for particles traversing the tubes. The Xe-based gas mixture used is chosen as it absorbs transition radiation (TR) photons efficiently providing larger signals than minimum-ionising particles (MIPs). This allows for discrimination between the track's drift circles and those originating from transition radiation. The TRT operates at the relatively balmy temperature of 20°C, maintained by a flow of CO_2 enveloping the system.

3.7 Calorimeter

The ATLAS calorimetry system, shown in Figure 3.5, provides energy and position measurements of electromagnetic (EM) and hadronic showers. The methodology of

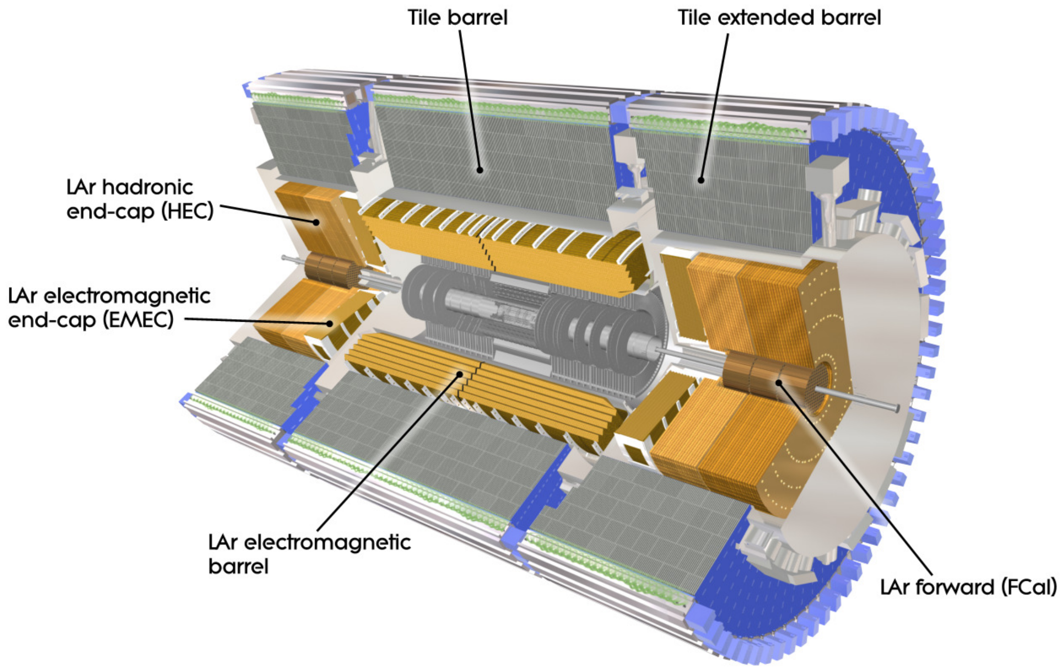

Figure 3.5: Diagram showing the arrangement of the hadronic, electromagnetic and forward calorimeter systems.[41].

both detectors is to have alternating layers of absorbing material, which initiate EM and hadronic showers, and a sampling material, which take energy and position measurements of the shower development. They are ϕ-symmetric and have almost hermetic coverage up to $|\eta| = 3.2$. Forward calorimeter systems extend this to $|\eta| < 4.9$, albeit affected by the higher fluxes in this region. The calorimeters have to fully contain the electromagnetic and hadronic showers and limit punch-through into the muon system. Therefore, conversely to the ID, they require a large amount of material to halt the showers within the calorimeter. By capturing the whole shower the total energy of the incident particle can be inferred from the sum of the energy deposited in each sampling layer. Any imbalance in the total transverse energy measured can be used to infer details of any weakly interacting neutral particles carrying away momentum unseen.

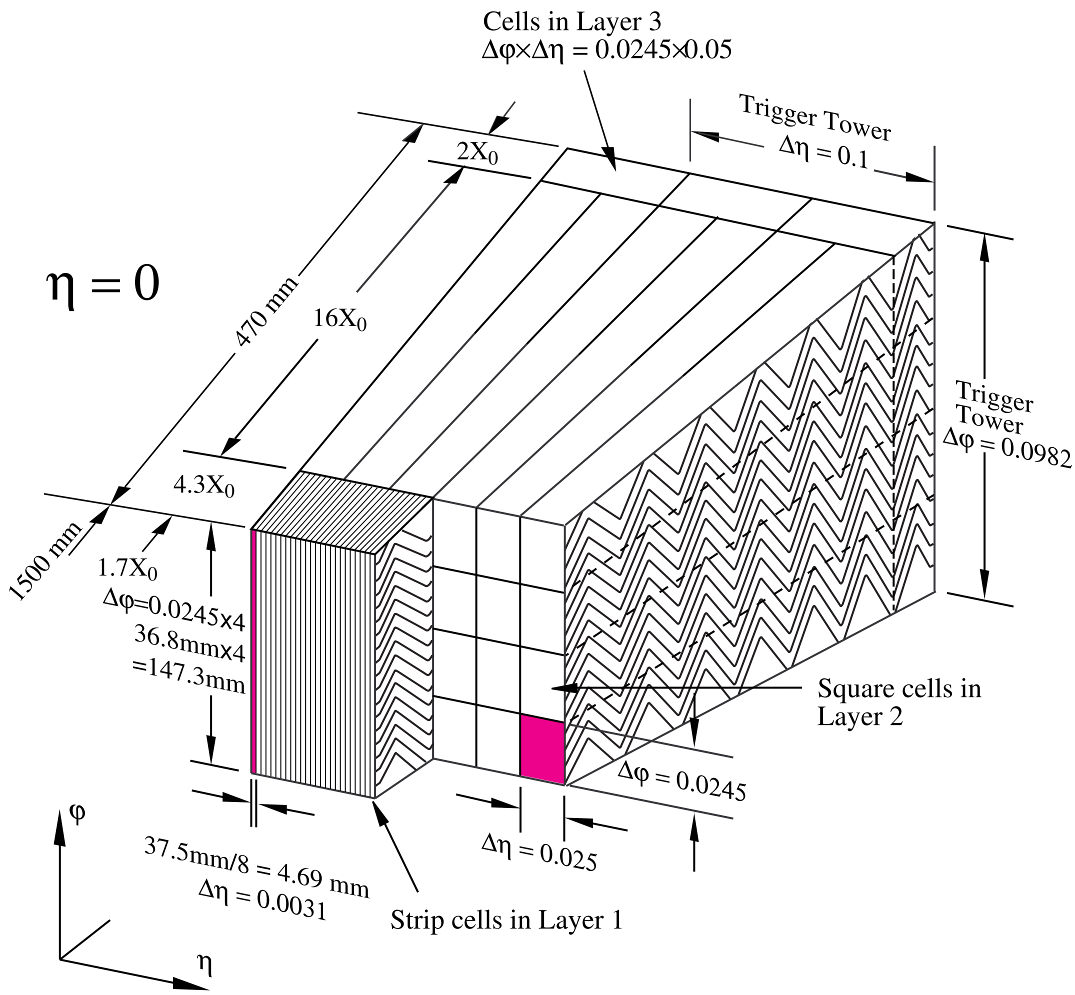

Figure 3.6: Diagram showing the segmentation of the ECAL into calorimeter cells and trigger towers[41].

3.7.1 Electromagnetic Calorimeter

The electromagnetic calorimeter (ECAL) is a lead-liquid argon (LAr) calorimeter. Its function is to measure the position and energy of electrons and photons incident on it. It also measures the neutral component of hadronic jets and τ leptons via the decay $\pi^0 \rightarrow \gamma\gamma$ depositing energy in the calorimeter. The ECAL has an accordion geometry which maximises ϕ coverage and speed of signal extraction. Thin layers of lead absorber initiate electromagntic showers when photons and electrons hit them. Electromagnetic showers are a cascade of electromagnetic interactions: Bremsstrahlung for electrons and e^+e^- pair production for photons, which form a narrow jet-like object.

Sampling layers of LAr are sandwiched between the lead absorbers. Electrons in the shower cause ionisation's of the argon and this charge is collected by layers of copper electrodes.

The barrel region is split into two half barrels covering the region $|\eta| < 1.48$. They have a combined length of 6.4 m and enclose the solenoid with an outer radius of 2m. In total the barrel contains 2048 absorber/sampler layers. The end caps cover the range $1.38 < |\eta| < 3.2$ and consists of two coaxial wheels which are 63 cm wide in total with 1024 absorber and sampling layers between them. These provide $\approx 22 - 30$ radiation lengths of material depending on η. The calorimeter is split into cells and towers which provide fine granularity measurements of the showers and trigger objects, full details are shown in Figure 3.6. The drift time for signals to reach the electrodes is around 450ns at 2000V. The ECAL readout time therefore spans several bunch crossings leading to the possibility of out-of-time pileup, where signals from future bunch crossings overlap with previous ones. Before particles reach the ECAL they have already passed through many radiation lengths of material in the inner detector and may have already lost energy. Therefore in front of the ECAL there is a pre-sampler layer of instrumented LAr which provides a position and energy measurement of the shower before the ECAL. This allows showers which may have been initiated in the inner detector to be corrected for.

The energy resolution of the ECAL is parameterised after noise subtraction by the following formula,

$$\frac{\sigma_E}{E} = \frac{a}{\sqrt{E(\text{ GeV})}} \oplus b, \tag{3.9}$$

where a is the stochastic sampling term and b is a constant describing local non-uniformities in the response. Test-beam studies with a beam of electrons between 10 and 245 GeV at $\eta = 0.69$ gives the sampling term to be $0.1\sqrt{\text{GeV}}$ and a constant term of 0.17%. This resolution varies as a function of η as the calorimeter depth varies along with changes in the thickness of upstream material.

3.7.2 Hadronic Calorimeter

The hadronic calorimeter (HCAL) measures the position and energy of hadronic jets originating from partons using two different technologies. The HCAL in the barrel region is a sampling tile calorimeter with steel absorbing layers and plastic scintillator sampling layers. A central barrel covers the range $|\eta| < 1.48$ and two extended barrels increase this by covering $0.8 < |\eta| < 1.7$. The material present represents ≈ 10 interaction lengths (λ). Charged particles passing through the scintillator material emit ultraviolet scintillation light. The scintillator contains fluors which shift the wavelength of this light towards the visible spectrum. This light is then collected by wavelength shifting fibres at the end of each tile. These fibres transmit the signal through to a set of photomultiplier tubes at the edges of the modules where the incident photons can be measured and an energy deposit determined.

In the hadronic endcap calorimeter (HEC) LAr calorimeter technology is used as in the ECAL. The HEC replaces the lead absorber with layers of flat copper plates. It covers the range $1.5 < |\eta| < 3.2$ with two wheels in each endcap region. The hadronic calorimeters follow a similar segmentation pattern to the ECAL allowing separation into separate cells used to form clusters of energy deposits.

The energy resolution of the HCAL after noise subtraction can again be parameterised by Equation 3.9. The resolution is dependent upon the particle type incident upon the calorimeter; the most precise measurements come from isolated pion test-beam results. In the tile calorimeter these tests yield a sampling term of $0.56\sqrt{\text{GeV}}$ and a constant term of 5.5%. For the HEC modules the response to π^+ and π^- test beams give sampling terms of $0.81\sqrt{\text{GeV}}$ and $0.84\sqrt{\text{GeV}}$ respectively, both with a constant term consistent with zero.

3.7.3 Forward Calorimeter

The forward calorimeters (FCals) cover the high η range $3.1 < |\eta| < 4.9$. Each FCal has three sub sections, an EM module FCal1 and two hadronic modules, FCal2 and FCal3. They all sit in the same cryostat systems as the other endcap calorimeters thus reducing gaps in coverage. High particle fluxes are expected in this very forward region from the underlying event (UL) and beam backgrounds. Therefore the LAr technology used in this region has thinner LAr gaps than the ECAL and HEC to reduce the signal collection time and to reduce ion build up problems. The absorber for FCal1 is copper to improve heat transfer whereas in the other two tungsten is used. The FCal system completes the coverage of the calorimeter system thus allowing robust missing transverse energy measurements to be made. As a bonus the FCAL also provides the muon chambers with shielding from the high flux of particles in the forward regions. The energy resolution for hadrons of the FCAL modules was again measured using pion test beams yielding a sampling term of $0.94\sqrt{\mathrm{GeV}}$ and a constant term of 7.5%.

3.8 Muon Spectrometer

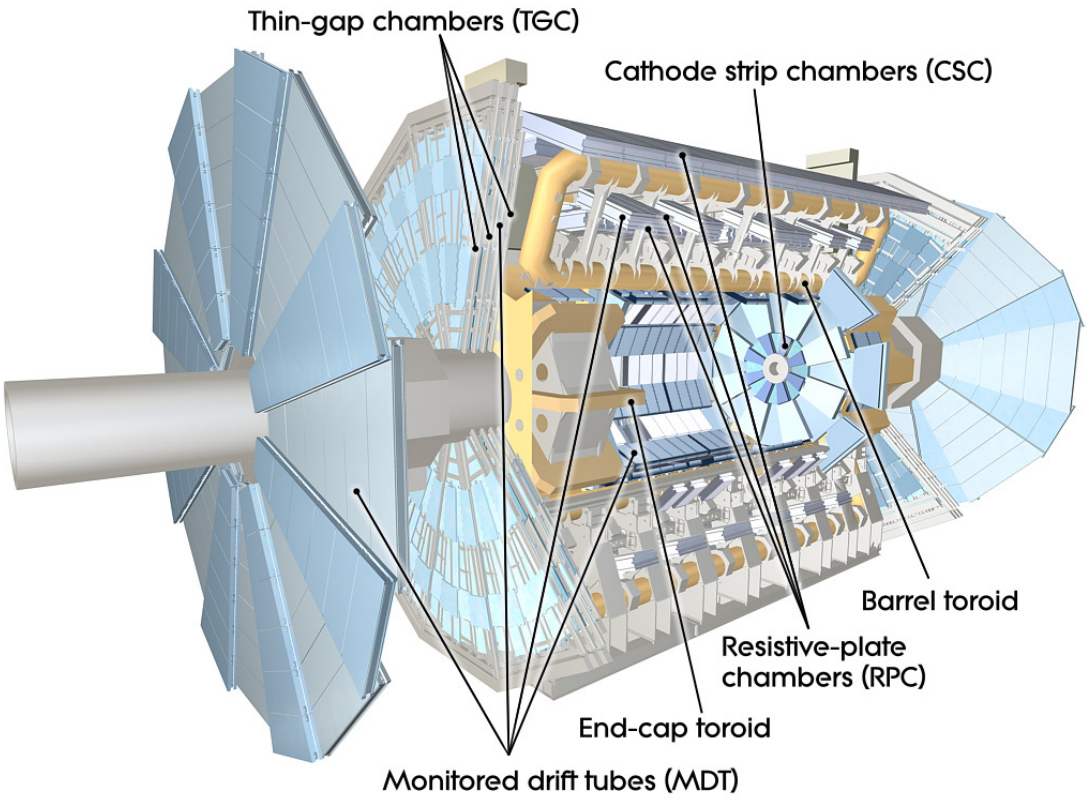

Figure 3.7: Diagram showing the muon system including the trigger chambers[41].

The muon spectrometer (MS), shown in Figure 3.8, provides tracking and momentum measurements of muons which have passed through the ID and calorimeter systems. It lies in and around the toroid magnets and defines the overall size of ATLAS. It covers the region $|\eta| < 2.7$ with a few gaps for services. The barrel and encap toroid magnets provide a non-uniform magnetic field to bend muons. The MS employs two precision measurement chamber designs: monitored drift tubes (MDTs) in the barrel and endcap covering the range $|\eta| < 2.7$; and cathode-strip chambers (CSC) in the inner endcaps, $2.0 < |\eta| < 2.7$. The MS also uses faster detectors for triggering purposes, with resistive plate chambers in the barrel ($|\eta| < 1.05$) and thin gap chambers (TGC) in the endcaps, $1.05 < |\eta| < 2.4$.

The precision tracking MDT chambers form cylindrical shells at radii of 5 m, 7.5 m, 10 m in the barrel region and four wheels at 7.4 m, 10.8 m, 14 m and 21.5 m from the IP in the z direction. The MDT's are pressurised drift tubes of radius 15 mm filled with an Ar/CO_2 gas mixture. A gold plated 50 μm W/Re anode wire runs along the centre of each tube and collects the charge from gas ionisations caused by muons passing through the tube. The chambers themselves are formed from 3 to 8 layers of MDTs depending on the position in the detector. In the very forward region CSCs are used to cope with the high particle fluxes present. These are multi-wire proportional chambers, with radially aligned anode wires and perpendicular cathode strips. They are filled with a different Ar/CO_2 gas mixture to the MDTs and record hits by interpolating the charge induced on adjacent cathode strips.

The MS trigger chambers provide fast triggering information from the MS providing a region of interest (ROI) and a fast estimate of the p_T of the muons. Resistive plate chambers are used in the barrel and are gaseous electrode plate chambers with a thin gap filled with a hydrocarbon gas mixture. There are three trigger stations between the MDTs each containing two RPCs which provide η and ϕ measurements. Thin gap chambers are used in the endcaps and are based on a similar technology to the CSCs. The trigger systems only cover up to $|\eta| = 2.4$, providing fast p_T information for the initial trigger decisions.

Chapter 4

Trigger System

The LHC is designed to deliver collisions at a rate of 40 MHz at an instantaneous luminosity of $10^{-34}cm^{-2}s^{-1}$. The data storage systems available can only store events at a rate of a few hundred events per second. With interesting physics events often rare, with cross-sections at the ≈pb level, a triggering system is needed to pick these needles out of the haystack of QCD and other higher cross-section standard model events. The trigger and data acquisition system is therefore vital. Without it ATLAS would mostly record uninteresting soft interaction events at a rate far higher than it could record. ATLAS employs a three level triggering system [41] to reduce the event rate to manageable levels by using event kinematics and topologies to select interesting events to be recorded to tape. The Level-1 trigger is a hardware trigger whereas the Level-2 and event filter (EF) triggers are software based running on computing clusters. A series of trigger chains are defined through each level for various physics objects. The bandwidth allocation to each chain at each level must be balanced across all possible chains taking into account expected rates and overlaps. If an event is triggered by at least one chain, then the event is considered interesting and recorded. The data is initially stored at CERN, then distributed to the GRID, a world wide data analysis and storage system. Here it can be stored and duplicated for easy processing and analysis. This chapter will outline in more detail the full ATLAS trigger system, the configuration system of the trigger and the methods employed to distribute the data recorded.

4.1 Level 1

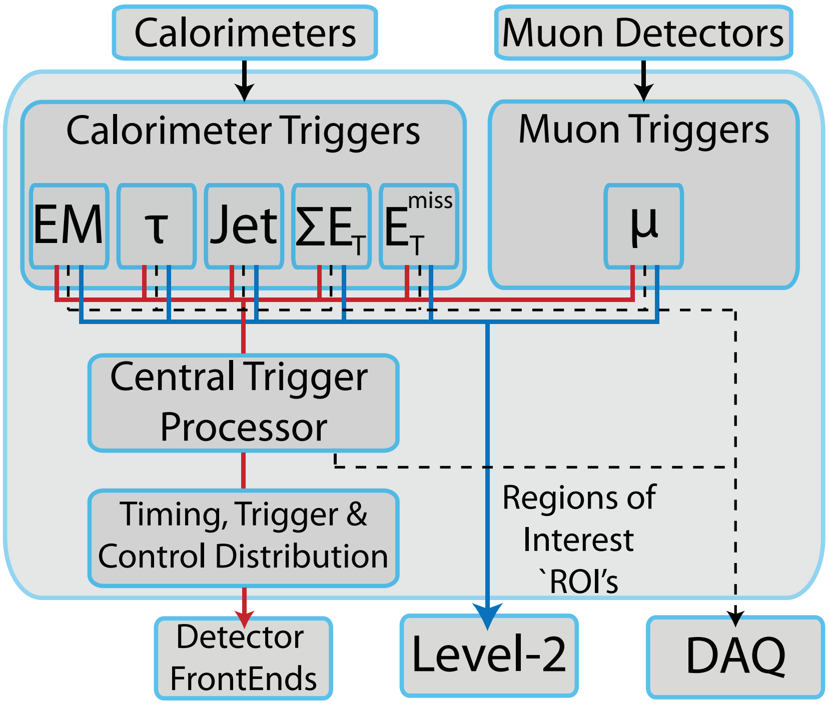

Figure 4.1: Diagram showing the level one trigger system[41].

The Level-1 hardware trigger makes an initial event selection reducing the event rate to below 100kHz. As an additional challenge this task must be performed within 2.5μs. This time constraint is due to the finite pipeline memory available to store events awaiting a decision. The decision is based on information from only the calorimeters and muon trigger chambers. The latency of both the inner detector and the full muon system is too high to provide information to the Level-1 trigger system within the required time. The Level-1 trigger is formed from specialised hardware processors. They are located on or near the detectors, therefore they are required to be radiation hard.

The Level-1 calorimeter trigger defines a series of programmable E_T thresholds for a selection of calorimeter objects including electrons/photons, jets and hadronically decaying τ leptons. The electromagnetic and hadronic calorimeters are divided into "trigger towers", shown in Figure. 3.6. Sliding window algorithms identify 2×2 clusters trigger towers with a combined energy deposit above the desired E_T threshold. Isolation of these deposits can be required by vetoing on large energy deposits in the surrounding twelve trigger towers. The EM and tau triggers cover up to $|\eta| < 2.5$, whereas the jet triggers and a set of jet E_T sum triggers extend to $|\eta| < 3.2$. Simple measurements of the missing transverse energy from particles escaping the detector and total ΣE_T thresholds can also be defined taking information from the whole calorimeter up to $|\eta| < 4.9$. For each calorimeter object type between four and 16 thresholds can be defined.

As mentioned in the previous Chapter the muon spectrometer possesses a set of dedicated trigger chambers to provide trigger information on the timescale required by the Level-1 system. In both the barrel and endcap the trigger uses lookup tables to find coincidental hits in the three trigger stations. The lookup tables contain ‘roads’ in which the hits must lie and whose width is defined by the p_T of the trigger. In total three low p_T (3-9GeV) and three high p_T (9-35GeV) thresholds can be defined in the lookup tables.

The multiplicities of each of the defined trigger objects are recorded and sent to the central trigger processor (CTP). The CTP can define 256 distinct trigger items each formed from a logical combination of the available threshold multiplicities. The CTP receives the threshold inputs from the calorimeter and muon readout systems and uses the logic defined in the Level-1 trigger menu to combine them into the desired trigger items. If the event is accepted by the CTP then it is passed to the Level-2 trigger. The Level-1 passes to the Level-2 the types of items which fired the trigger along with their locations in $\eta - \phi$ space. These locations are known as the regions of interest, RoIs.

4.2 High Level Trigger

The High Level Trigger (HLT) is formed by the Level-2 then Event Filter (EF) triggers. These software triggers run on a dedicated farm of around 2000 rack mounted computing nodes. The Level-2 trigger is the first level of software trigger at ATLAS, with the dedicated computing cluster running a specialised version of the ATLAS software framework (ATHENA). It receives the RoI’s selected by the Level-1 trigger accepts and uses them as seeds to run more sophisticated search algorithms on. The Level-2 trigger has $\approx 10ms$ in which to make a trigger decision. In this time it aims to reduce the event rate to around 3kHz which is defined by the rate at which the next stage, the Event Builder, can reconstruct the event for the EF. The Level-2 system has access to the full granularity information of the ATLAS detector. Using the Level-1 ROI seeds allows the Level-2 system to only need to read around 10% of the detector information to form a decision. The Level-2 decision is made by trigger chains. These are sequential lists of trigger signatures which are evaluated in order, halting the chain if one fails. Each signature is formed from a logical combination of trigger elements. The trigger elements run the necessary reconstruction and trigger algorithms to form a decision at each signature step. Each Level-1 ROI initiates a set of Level-2 trigger chains relevant to the object threshold and type that the ROI is related to. The Level-2 chains then steps through the elements running each successive step on the previous step's output. By only running on the RoI's highlighted by the Level-1 system and stopping chains that fail, the Level-2 farm can quickly make a more detailed decision within the allowed time. The Level-2 trigger passes events containing any successful trigger object onto the EF. At this stage all events are fully reconstructed by the Event Builder.

The Event Filter is the final stage of the ATLAS trigger. It uses the algorithms present in the offline version of ATHENA to make a final event selection. It has of the order a few seconds per event to make its decision and reduce the rate to a few hundred Hz. This final rate is defined by the rate at which events can be recorded to tape. Data storage at CERN can record between 300 and 600 Mb/s from ATLAS. Therefore with an average event size of 1.3 Mb the EF output limit is a few hundred Hertz. The HLT follows the same logic as the Level-2 trigger continuing the trigger chains with more sophisticated algorithms. If an event passes through a full trigger chain, from Level-1 through to the Event Filter, it is then recorded along with information of all of the triggers that it passed. An event is placed into data streams defined by the triggers it passed. There are a set of physics streams which take events from groups of physics triggers, the main physics streams are; egamma for electron and photon triggers, muon, jet (which includes triggered τ objects) and $E_{\mathrm{T}}^{\mathrm{miss}}$. There is a small amount of overlap between the streams. There are also express, calibration and debug streams which take small samples for testing and debugging purposes.

4.2.1 Prescales and Passthrough

There are trigger cases where a trigger will record interesting or useful data but the data rate would be too high to allow its inclusion. Prescale factors can be applied to reduce the rate associated with such triggers. Prescales can be applied at each level on any trigger item or chain. Low p_T jet triggers for example are prescaled in this way as it is useful to maintain a sample of low p_T QCD events for analysis, but the rate would be prohibitive without a high prescale. Prescales can be also be used to test the rate of new triggers before placing them into the system at potentially high rates. Passthrough of a trigger can also be defined to force a set fraction of events be accepted by the trigger, still recording the decision but not removing any events. In early low luminosity running the Level-1 system alone could keep the rate under control. At this time the entire HLT ran in passthrough mode, allowing testing of HLT rates to occur in preparation for the HLT's activation at higher luminosity.

4.3 Trigger Configuration

The full trigger system has to be configured consistently and coherently over all three levels. Therefore ATLAS has set up a trigger configuration system [43] which can configure the complete trigger menus and chains consistently from Level-1 through to Event Filter. It can also store the information for future usage in Monte Carlo production or analysis. Its main constituent is a relational database, the Trigger Database, which stores the Level-1 and high level trigger (HLT) menus. Each table in the database is defined by a unique primary key, thus preventing the duplication of records. Links can be formed between tables by linking the primary key of the top table as a foreign key in the lower table, as shown in Figure 4.2

In the database the Level-1 menu defines;

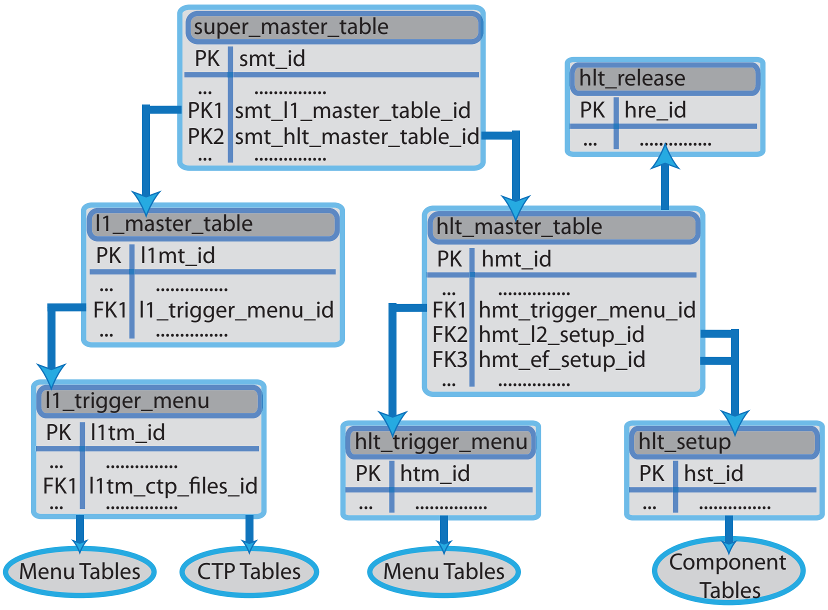

Figure 4.2: Diagram showing a simplified view of the Trigger Database. The whole database can be defined by a single SuperMasterKey that defines a full unique set of the database tables.

1. The trigger thresholds that the Level-1 calorimeter and muon systems must record the multiplicity for in each event.

2. The logical combinations of the thresholds that the CTP should use to form trigger items.

3. The full technical parameters for running the Level-1 menu such as prescale factors and random trigger rates.

With this information the CTP and Level-1 hardware can configure all of the Level-1 items and thresholds. The HLT menu defines:

1. The trigger elements, signatures and chains to be used in the Level-2 and EF triggers along with the Level-1 item each chain should be seeded by.

2. The links between the trigger elements and the algorithms that produce the results required.

3. The full technical parameters for running the HLT menu such as prescale factors, trigger algorithms and software components.

This information defines everything needed to set up the logic and algorithms for the HLT.

These menus can be stored and loaded from the database by defining three unique keys. The SuperMasterKey (SMK), which defines a unique state of the Level-1 and HLT menus with one single key. The Level-1 and HLT prescale keys, which define the prescales needed for the triggers present in the current configuration. The Level-1 and HLT menus are loaded at the start of the run by defining a single SMK. It selects from the database a predetermined set of triggers relevant for the expected beam conditions of the run and the current physics needs. A set of prescale keys are defined to produce the same output rates at different instantaneous luminosities. At the start of the run the prescales can be loaded to match the starting luminosity. At any time during the run a new prescale key can be loaded providing great flexibility in the trigger system. As the luminosity decreases over the course of the run the prescale key can be changed, reducing prescales on items to maintain a steady rate of data taking. If a certain trigger becomes noisy then a new prescale set can be created and the noisy trigger masked out without having the reload the whole menu.

4.4 The Trigger Tool

The Trigger Tool is a graphical user interface (GUI) system that provides the sole access to the Trigger Database. The main panel of the tool is shown in Figure 4.3. It allows the browsing and manipulation of the database whilst maintaining the consistency of the menus and prescale keys produced. Users can browse the trigger database to see the configuration defined by any SMK and the valid prescale keys for that configuration. It allows browsing of the data base in a “tree view” style showing the hierarchical nature of the database. Users can use it to define prescale sets for a given menu. Users can define new trigger configurations using the Trigger Tool. This can be done by either editing the contents of previous menus or uploading menus to the

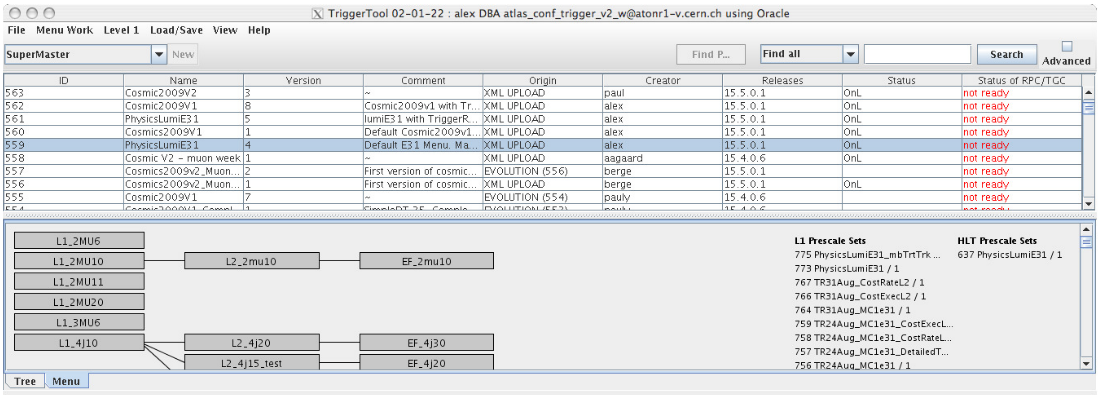

Figure 4.3: Diagram showing main browsing panel of the Trigger Tool. The top panel shows the available Super Master Keys. The bottom panel shows a simple tree view of the selected configuration as well as the associated prescale sets. The menus at the top allow access to the full browsing and editing features of the Trigger Tool.

database from external extended markup language (XML) files. In each case when a new SMK or prescale set is formed the Trigger Tool checks to see if the menu already exists. If it does not exist, the new object is stored in the database and a new key is given. If it does already exist then the Trigger Tool simply returns the existing SMK or prescale set unique identifier. By doing so the Trigger Database contains no duplication of SMK or prescale sets. The Trigger Tool also contains links to the software that controls the Level-1 CTP system. This allows input Level-1 menus to be communicated to the CTP which is programmed directly by propriety software.

The Trigger Tool offers multiple levels of users to differentiate separate tasks it performs. The average users, trigger shifters, have simple accounts that allow them to browse the database to visualise the menus they are using. They can also produce new prescale keys allowing them to react to changes in the data conditions rapidly. Higher level tasks are restricted to expert users. This separation allows the tool to be used by non-experts without causing problems in the Trigger Database.

4.5 The Distribution System

The triggered data recorded by ATLAS needs to be reconstructed and distributed for analysis. When data are recorded they are initially sent to the Tier 0 computing farm at CERN, shown in Figure 4.4. The meta-data containing the trigger configuration

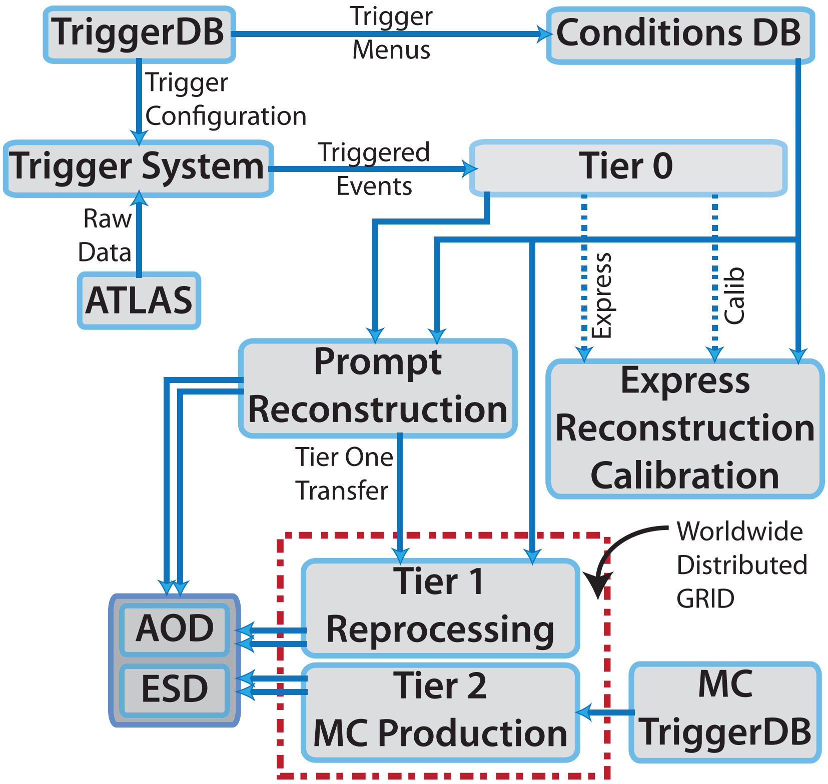

Figure 4.4: Diagram showing a simplified view of the ATLAS data distribution system. The data is triggered in ATLAS and sent to Tier 0 in CERN for processing. The data is replicated to the GRID (Tier 1 and 2 sites) where reprocessing and analysis occurs. Monte Carlo events are produced and distributed on the GRID for analysis. The conditions database is used to define the detector status in data and MC events.

information for the run is at the same time sent to the conditions database. The Tier 0 site performs a prompt reconstruction of the data into the detailed event summary data (ESD) files and slimmed analysis object data (AOD) files. The information on the trigger objects passed alongside more detailed trigger information for studies is attached to the data at this point. The data is then distributed to the Tier 1 and 2

GRID sites for storage and analysis. The GRID is a worldwide distributed network of computing clusters. Distributing the data in such a fashion protects against loss of data by storing multiple copies. Analysis jobs can be sent to the GRID Tier 2 sites, allowing rapid analysis of the large data sets.

Chapter 5

Object Reconstruction

In order to identify semi-leptonic $t\bar{t}$ candidates the electron, muon, jets, and missing energy present in the system need to be efficiently identified and reconstructed with a good energy resolution. This chapter will provide a description of the reconstruction of analysis objects from detector information and the object pre-selection cuts for each of the relevant physics objects [41].

5.1 Tracks

Tracks at ATLAS are reconstructed using the hit information from charged particles traversing the inner detector, under the influence of the solenoid magnetic field. These tracks are used to form the vertices involved in the interaction. Track reconstruction begins by forming clusters of space points from the pixel and SCT hits. The TRT timing information is also used to form drift circles. Track segments are formed from the space points in the three pixel layers and the first SCT layer. The trajectories of these track segments are then extrapolated through the rest of the SCT forming candidate tracks which are then fitted to clusters in the SCT to remove fakes and ambiguities. The tracks are then extended again into the TRT and use the extrapolation to resolve the ambiguity in the TRT drift circles. Tracks reaching this point are refitted using the full information of the inner detector to improve the resolution of the track. A second pass then runs from the TRT inwards searching for unused track segments in the TRT.

They are then extrapolated back into the SCT and pixels to find tracks originating from displaced or secondary vertices, originating from long lived particles or conversions in the detector material. The tracks formed here are used as an input to a vertex finder to reconstruct the primary vertices present in the event, which are used to define the interaction point(s) of the event and vertex resolution information [44].

5.2 Electrons

Electrons and photons produce electromagnetic showers as they enter the EM calorimeter. To reconstruct the electron energy, the energy deposited in calorimeter cells by the shower must be summed to give the total electron energy. In ATLAS a sliding window algorithm is used to search for and cluster the energy deposited by electrons. The algorithm proceeds in three steps; tower building, pre-clustering and cluster filling.

To begin the procedure, the calorimeter is split into a grid of calorimeter elements of size $\Delta\eta \times \Delta\phi = 0.025 \times 0.025$, highlighted in Figure 3.6. The energy deposited in cells within the calorimeter elements are summed through all calorimeter layers to form a tower energy. If an electron shower lies between multiple towers its energy is split between the two towers according to the fraction of the cell overlapping each tower. A window is defined as $N_\eta \times N_\phi$ in units of calorimeter towers. The transverse energy of the towers contained in this window are summed to form the window E_T. The window is allowed to scan the calorimeter and if the window E_T lies above a threshold E_T^{Thresh} then the window is accepted as a precluster. A window size of 5×5 towers and $E_T^{\text{Thresh}} = 3GeV$ are chosen to suppress the number of preclusters formed from calorimeter noise. If two preclusters overlap within 3×3 towers then the lower p_T precluster is removed. A secondary window algorithm, seeded upon the preclusters, is used to form clusters representing the full EM showers. The window size is dependant upon the EM calorimeter layer and the assumed particle type as photons and electrons have difference shower shapes. By the end of the algorithm a cluster of cells has therefore been formed from the preshower through to the back of the EM calorimeter. The cluster sizes used for each particle type, shown in Table 5.1, are op-

Particle Type	Barrel	Endcap
Electron	3×7	5×5
Converted Photon	3×7	5×5
Prompt Photon	3×5	5×5

Table 5.1: The cluster size in units of towers, $N_{\eta}^{towers} \times N_{\phi}^{towers}$, used for each EM particle type considered.

timised to contain the energy deposits of the EM shower whilst minimising the noise captured. Photon showers tend to be narrower than electron showers because electrons can interact more in the ID and PS and can emit bremsstrahlung photons. In addition, the solenoid-induced B-field bends the charged particles in ϕ and thus a wider window is used in the ϕ direction. Converted photons produce electron-positron pairs before the calorimeter and therefore are also smeared in ϕ by the B-field. The same window size for electrons and photons is used in the endcaps due to the reduced effect of the B-field. The final cluster energies can then be corrected to account for various effects including the ϕ-dependance of the absorbing material traversed by the incident particles, the loss of shower energy outside of the cluster and the finite granularity of the calorimeter.

Electron clusters can be distinguished from ones arising from photons by matching back to tracks in the inner detector within $\Delta\eta < 0.05$ and $\Delta\phi < 0.1$. If no track is found then the cluster can be considered as an unconverted photon and the appropriate shower shape used. The η, ϕ direction of the selected tracks are then extrapolated into the calorimeter and their compatibility with the cluster centres in each layer tested. The track with the closest match is considered to be the electron and can then be used to make momentum and charge measurements. A photon which has undergone a conversion in the inner detector can be misidentified as an electron. This background is reduced by making tighter requirements on the track found such as having hits in the pixel layers, which reduces the chance of a converted photon causing the track [45, 46].

Cluster and track combinations are then accepted as an electron object if they pass

Type	Cut Description
	Loose requirements
Detector acceptance	$\|\eta\| < 2.47$ and exclude $1.37 < \|\eta\| < 1.52$
Hadronic leakage	Ratio of E_T in the first sampling of hadronic calorimeter to the E_T of the EM cluster
Middle layer of EM calorimeter	Ratio in η of cell energies in 3×7 versus 7×7 cells. Lateral width of the shower
	Medium requirements
Strip layer of EM calorimeter	Total lateral shower width (20 strips) Ratio of the ΔE between the two leading energy deposits to the sum
Track quality	At least one pixel hit At least seven hits in the pixels and SCT combined Transverse impact paramter < 5 mm
Track Matching	$\Delta\eta$ between the cluster and the track in the strip layer of the EM calorimeter
	Tight requirements
B-layer	At least one B-layer hit
Track matching	$\Delta\phi$ between the cluster and the track in the middle of the EM calorimeter Ratio of the cluster energy to the track momentum
TRT	Total number of hits in the TRT Ratio of the high-threshold hits to the total number of TRT hits

Table 5.2: The pre-selection cuts defining loose, medium and tight electron objects, the cuts are cumulative through each level.

a series of pre-selection cuts. Electrons are first required to pass the ATLAS definition of a Tight [45] electron. These are a cumulative series of cuts designed to select good electron candidates whilst rejecting photons and jets faking electrons, described in Table 5.2. Tight electrons are then required to have a $E_T > 20$ GeV and to be found within $|\eta| < 2.47$ representing the fiducial region of the EM calorimeter. Electrons in the calorimeter barrel-endcap overlap region, $1.37 < |\eta| < 1.52$ are rejected to avoid the poorly instrumented region. In order to suppress fake electrons from jets and electrons from heavy-flavour decays, the electron cluster and track are required to be isolated from additional energy deposits. The electron is therefore rejected if there is $p_T^{calo} \geq$ 4 GeV of additional energy deposited in the calorimeter in a cone of $\Delta R < 0.2$ around the electron. In addition, an object quality map (OTX map) from the run with the highest luminosity (run 167521) is applied to reject electrons originating from detector regions with known problems such as non-nominal high voltage or readout problems. The OTX cut is applied consistently in both data and MC. Any electrons left after these cuts can be considered in the analysis [47].

5.3 Muons

Muons traverse the entirety of the ATLAS detector leaving track hits in the inner detector and muon spectrometer and a minimum ionising signature as they pass through the calorimeters. Muon candidates are reconstructed combining the information from the muon spectrometer and the inner detector. Hits in the MS are first combined into track segments and then tracks by the MOORE [48] algorithm. Segments are formed from sets of consistent hits in the MS system sub detectors, these are then combined with hit information in the trigger chambers to form ‘roads’ through the MS. Tracks are then formed along these roads by assigning hits to the tracks taking into account energy losses and coulomb scattering as the muon passes through the detectors. These tracks form the input into the MUID [48] combined algorithm, which aims to match the MS tracks back to a track in the ID. MUID begins by expressing the tracks found by MOORE in the same representation as the ID tracks. A combined fit along the entire muon track is then performed in a similar manner as in the MS but including the hits from the ID track. If a satisfactory fit is found then the track is retained as an identified muon object. Corrections are applied to account for the muon energy loss in the calorimeter.

The identified muons are then requested to pass a series of pre-selection cuts. Combined muons found by MUID are required to have $p_T > 20\,\mathrm{GeV}$ and $|\eta| < 2.5$. To ensure a complete track through the detector hit requirements are made on the combined muon track. The track is required to have a hit in the pixel B-layer, followed by at least two hit in the rest of the pixel detector. At least six hits are requested in the SCT. The total track 'holes' in the pixel and SCT are required to be less than two, where a hole is a missing hit in a layer on the path of the track. If the track passes through a known dead module in the pixel or SCT detector then this it counted as a hit and does not add to the total holes. In the TRT, the total number of hits is defined as the sum of on track hits and outliers, $n = n^{hits}_{TRT} + n^{out}_{TRT}$. Within $|\eta| < 1.9$ a requirement of $n > 5$ and $n^{out}_{TRT} < 0.9 \times n$ is made. Outside $|\eta| > 1.9$ the requirement is loosened to $n^{out}_{TRT} < 0.9 \times n$ if $n > 5$. These requirements ensure a good track which traverses the entire ID before being matched to the MS track. In order to reduce fake backgrounds and leptonic decays within heavy flavour jets, the E_T in a cone in $\eta - \phi$ space of radius $R = 0.3$ is required to be $< 4\,\mathrm{GeV}$ in the calorimeter. In addition, the scalar sum of the transverse momentum for additional tracks inside a cone of $R = 0.3$ is required to be less than 4 GeV. Muons are also removed if they are found to be within $\Delta R < 0.4$ of a reconstructed jet with $p_T > 20GeV$, again to reduce muons from heavy flavour decays. Muons remaining after these cuts are then available to be used in the analysis [47, 41].

5.4 Jets and b-jets

All hadronic jets used in this analysis have been reconstructed using the anti-k_t [49] sequential recombination algorithm with a width parameter equal to 0.4. The anti-k_T jet algorithm is a relatively new jet algorithm being used at both ATLAS and CMS. This algorithm is both infra-red safe and collinear safe, as shown in Figure 5.1. Infra-

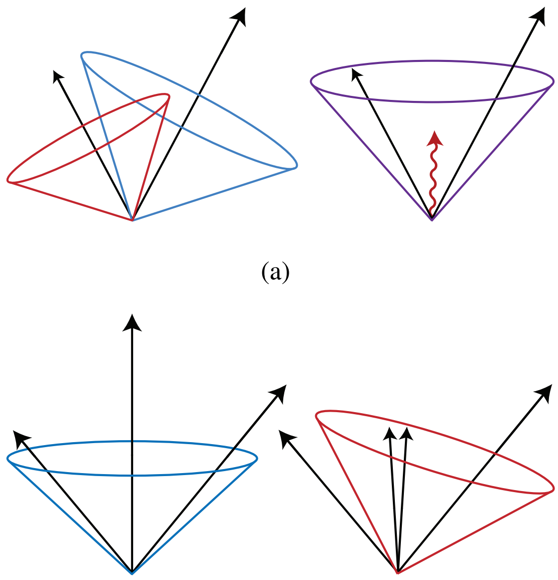

(a)

(b)

Figure 5.1: Diagrams showing possible problems arising in jet algorithms. (a) Infrared safety: a soft gluon emission should not change the jet algorithm's result, (b) Collinear safety: one parton splitting into two collinear partons should not change the jet algorithm's result,

red safety requires that the emission of a soft gluon should not change the outcome of the jet clustering. Collinear safety requires that the splitting of a parton into two collinear partons should not alter the jet clustering.

Sequential recombination algorithms are a generic class of jet algorithms which, instead of forming jets using cones of a fixed radius, cluster objects sequentially into jets. First topological clusters (topoclusters) of energy deposits are formed in the calorimeter by taking seed cells above a threshold signal-to-noise ratio, $\Gamma = E_{cell}/\sigma_{cell}^{noise}$, and forming a three dimensional object by clustering adjacent cells. These topoclusters loosely represent the energy deposited in the calorimeter by individual particles. This is possible due to the fine segmentation of the ATLAS calorimeters. The algorithm then defines a distance parameter between the topoclusters and a distance parameter between the clusters and the beam axis,

$$d_{ij} = \min\left(k_{ti}^{2p}, k_{tj}^{2p}\right)\frac{\Delta_{ij}^2}{R^2}, \tag{5.1}$$

$$d_{iB} = k_{ti}^{2p}, \tag{5.2}$$

where $\Delta_{ij}^2 = (y_i - y_j)^2 + (\phi_i - \phi_j)^2$ and k_{ti}, y_i and ϕ_i are respectively the transverse momentum, rapidity and azimuth of topocluster i. R defines the 'radius' of the resultant jet and p defines the power of the k_t and Δ_{ij} scales. The algorithm forms lists of d_{ij} and d_{iB} for all clusters. It finds within these lists the minimum distance parameter, d_{min}. If $d_{ij} = d_{\mathrm{min}}$ then the topoclusters i and j are combined into a new cluster k. This new cluster then replaces i and j in the list of topoclusters to be combined. If $d_{iB} = d_{\mathrm{min}}$ then the object i is now considered a finished jet and it is removed from the list of objects to be combined. As topoclusters can only enter into one jet the algorithm is infra-red safe. Due to not using seeds to define jet centres the algorithm is also collinear safe. The anti-k_t algorithm used in this analysis is defined by setting $p = -1$. This parameter choice retains the properties of infra-red and collinear safety. However unlike other algorithms with different choices for p ($p = 1$ for the k_t algorithm and $p = 0$ for the Cambridge-Aachen algorithm) it forms more recognisable 'cone' shaped jets. This feature is driven by experimentalists' desire for easily understood, regular objects.

The topoclusters used in the jets have been measured at the electromagnetic scale (EM-scale). This is the energy scale correctly accounting for the energy deposited by photons and electrons in the calorimeters. The ATLAS calorimeter is non-compensating calorimetry system, meaning the electromagnetic detector response is not equivalent to the response to hadronic particles. Therefore for hadronic jets the EM scale energy is generally $\approx 30\%$ lower than the actual energy deposited. A jet energy scale (JES) therefore has to be applied on top of the initial EM-scale measurement to obtain the true jet energy at the hadronic particle scale [50]. The JES also takes into account various additional effects on the measurement of jets energies including:

1. Loss of energy in known dead regions of the detector,

2. Particles escaping the active region of the calorimeter,

3. Particles not included in the reconstructed jet that are part of the true jet energy,

4. Inefficiencies in the calorimeter clustering and jet reconstruction algorithms.

The JES is derived as a function of η and p_T. The JES response of the EM-scale jets

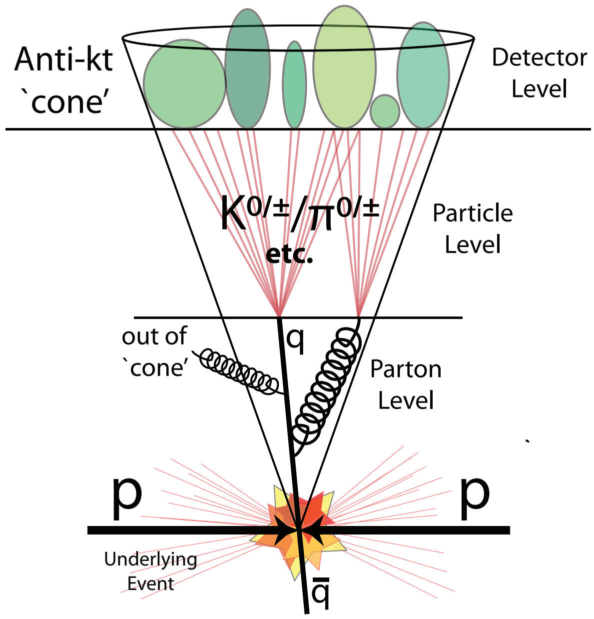

Figure 5.2: Diagram representing the different jet levels of a generic jet from a QCD dijet event.

(R^{EM}) is calculated by matching reconstructed EM-scale jets to particle level truth jets in MC with $\Delta R < 0.3$ and taking the ratio,

$$R^{EM} = \frac{p_T^{\text{jet,EM}}}{p_T^{\text{MC truth jet}}}. \tag{5.3}$$

The JES response of jets is calculated in a large sample of isolated QCD dijet MC events to provide an average response over the range of η and p_T, which can then be used to correct measured jets back to the hadronic particle level. The particle level jet is defined as the point at which the jet has fully hadronised, as can be seen in Figure 5.2. This method relies on an accurate modelling of jets in MC and is therefore subject to systematic effects where the response may be mis-modelled between MC and data. These systematics are the most important uncertainties present in this analysis and the full JES-uncertainty will be outlined in Chapter 8.

The resulting corrected anti-k_t jets are then subjected to additional pre-selection cuts before they are accepted as an analysis object. If a jet is the closest jet within $\Delta R = 0.2$ of an electron candidate it is removed to avoid double counting reconstructed electrons as hadronic jets. The calorimeter suffers from occasional noise bursts and the effects of non-collision backgrounds which can occasionally fake high p_t jet activity. Therefore a set of jet cleaning cuts are applied to remove events which contain a 'bad' jet above 20 GeV. After these cuts jets are accepted for consideration in the final analysis [47].

In the final state of the $t\bar{t}$ system there are two jets originating from b quarks. To distinguish these jets from light-quark jets a b-tagging algorithm is used. This reduces non-$t\bar{t}$ background events and reduces the combinatorics involved in assigning jets correctly in the $t\bar{t}$ reconstruction. The b-quarks from top decays form heavy B mesons which have lifetimes long enough to travel a measurable distance (around 3 mm) in the detector before decaying. Therefore tracks from the b-hadron decay form a secondary vertex in the inner detector which can be used to 'tag' the jet as a 'b-jet'. The jets selected by the pre-selection cuts are passed to a secondary-vertex tagger (SV0) [51] to identify b-jets. This tagger takes the list of tracks associated with each calorimeter

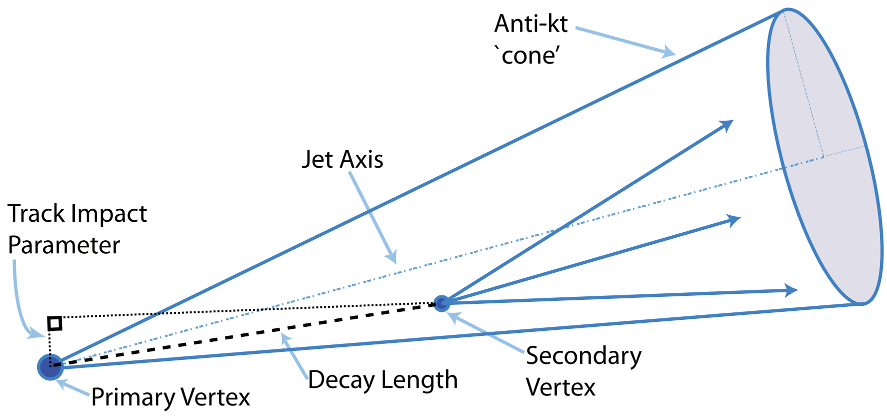

Figure 5.3: Diagram showing a secondary vertex originating from the decay of a long lived particle within the jet. Jets originating from b-quarks can be tagged by searching for secondary vertices within jets that have a large impact parameter significance with respect to the primary vertex.

jet. The SV0 algorithm searches for secondary vertices formed from two tracks which are significantly displaced from the primary vertex, as shown in Figure 5.3. Secondary vertices are required to be formed from tracks with a large combined track impact parameter and to form a vertex which has a statistically significant displacement from the primary vertex. Jets can be tagged as originating from a b-quark by placing cuts on the signed decay length significance, $L/\sigma(L)$, of a secondary vertex found within the jet. A balance needs to be struck between b-tagging efficiency and the purity of the selected sample when selecting the cut value. For this analysis a working point of $L/\sigma(L) > 5.85$ has been used giving a b-tag efficiency of 50% per b-quark in $t\bar{t}$ events. This point provides a sample purity of 94% with the majority of contamination originating from c-jets which also contain a displaced vertex.

5.5 Jet Transfer Functions

The jet energy scale corrects jets in the events back to the particle level as shown in Figure 5.2. Correcting back to the particle level is generally the correct approach to implement as due to quark confinement the parton level is an unphysical representation of the system. The top quark however decays before before it hadronises. To correctly reconstruct top quarks it is therefore necessary to correct the jet energies back to the partonic level. This analysis involves the reconstruction of the entire $t\bar{t}$ system. It is therefore necessary to derive a set of jet transfer functions to correct the jet energies back to the partonic level.

Hadronic showers formed from different flavour partons do not necessarily have the same content. Light flavour jets tend to contain mostly light mesons such as $\pi^{0/\pm}$s or $K^{0/\pm}$ mesons, whereas heavier quarks can hadronise to a higher fraction of heavier mesons. Heavier mesons decay leptonically within the detector more often, and therefore the jet formed can contain a larger neutrino contribution. Thus there is a difference in detector response between jets of different flavours. In order to accurately reconstruct the $t\bar{t}$ system these differences need to be addressed. The transfer functions are defined as a function of p_T separately for both b-jets and light-quark jets (those originating from u, d, s and c quarks). The default SM $t\bar{t}$ Monte Carlo sample is used to derive the transfer function back to the partonic level. An altered set of selection cuts are defined where the p_T requirement of the jets is loosened to 15 GeV, which is the lowest p_T that the generic JES correction is defined for. For each event passing the altered selection cuts a list of jets is formed and the light quarks and b-quarks originating from the hard scatter are selected from the Monte Carlo truth information. Jets are then matched to partons if they are found to satisfy $\Delta R < 0.2$, thus separating the sample of jets into b-quark and light quark initiated jets.

The transverse momentum of the truth parton, p_T^{Parton} is compared back to the transverse momentum of the matched jet, p_T^{Jet}, to provide a response, R, for each jet defined as,

$$\mathrm{R} = \frac{p_T^{\mathrm{Parton}} - p_T^{\mathrm{Jet}}}{p_T^{\mathrm{Jet}}}. \tag{5.4}$$

The distribution of responses for both jet flavours is split into p_T bins to allow the parameterisation of an average response over a range of 15 GeV $< p_T <$ 200 GeV. In this range the p_T bins for each sample are selected to provide an even distribution of statistics. Each p_T bin is fitted using a double gaussian function and the mean of the narrower main gaussian is taken as the most probable value for the average response, $\bar{R}$, of the bin, shown for the light and b-jets in Figures 5.4 and 5.5 respectively. The average response is parameterised using a function of p_T^{Jet},

$$\bar{R} = e^{\left(a+b.p_T^{\mathrm{Jet}}+c/p_T^{\mathrm{Jet}}\right)} + d. \tag{5.5}$$

The transfer function results for both the light and b-jets are shown in Figure 5.6(a). The light jet response is close to zero for the whole p_T range, whereas the b-jet response increases sharply at low p_T. This is expected as the generic jet JES is defined from a dijet QCD sample which will be dominated by light flavour jets, therefore modelling their response better than the heavier b-jets. The transfer functions can now be used to correct the jet energies back to the partonic level. The truth parton momentum can then be compared to the jet energy after the application of the appropriate flavour transfer function via,

$$\mathrm{R}' = \frac{p_T^{\mathrm{Parton}} - p_T^{\mathrm{Adjusted\ Jet}}}{p_T^{\mathrm{Parton}}}. \tag{5.6}$$

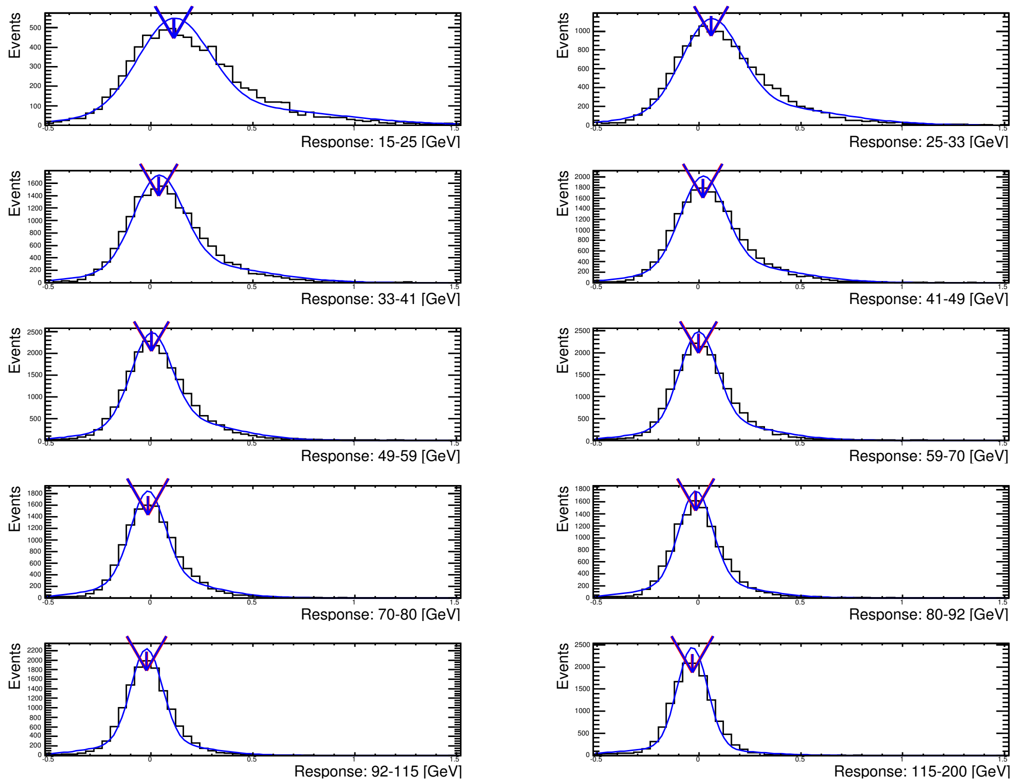

Figure 5.4: Diagrams showing double gaussian fits to gain the most probable value of the average response for each p_T bin of light jets. The most probable value is represented by the blue arrow which is the mean of the gaussian modelling the peak.

Repeating the binning used previously, the two samples can be fitted again using a gaussian function. From each p_T bin the width of the gaussian can be taken as an average uncertainty for the p_T of the newly corrected jets. These widths can once again be parameterised by Equation 5.5, the result of this parameterisation can be seen in Figure 5.6(b).

5.6 Missing transverse energy

Missing transverse energy ($E_{\mathrm{T}}^{\mathrm{miss}}$) in events indicates the presence of particles which have escaped the detector undetected. For example the neutrino present in semi-leptonic $t\bar{t}$ decays passes through ATLAS undetected. $E_{\mathrm{T}}^{\mathrm{miss}}$ is reconstructed as the negative transverse vector sum of all cluster momenta in the calorimeters with ad-

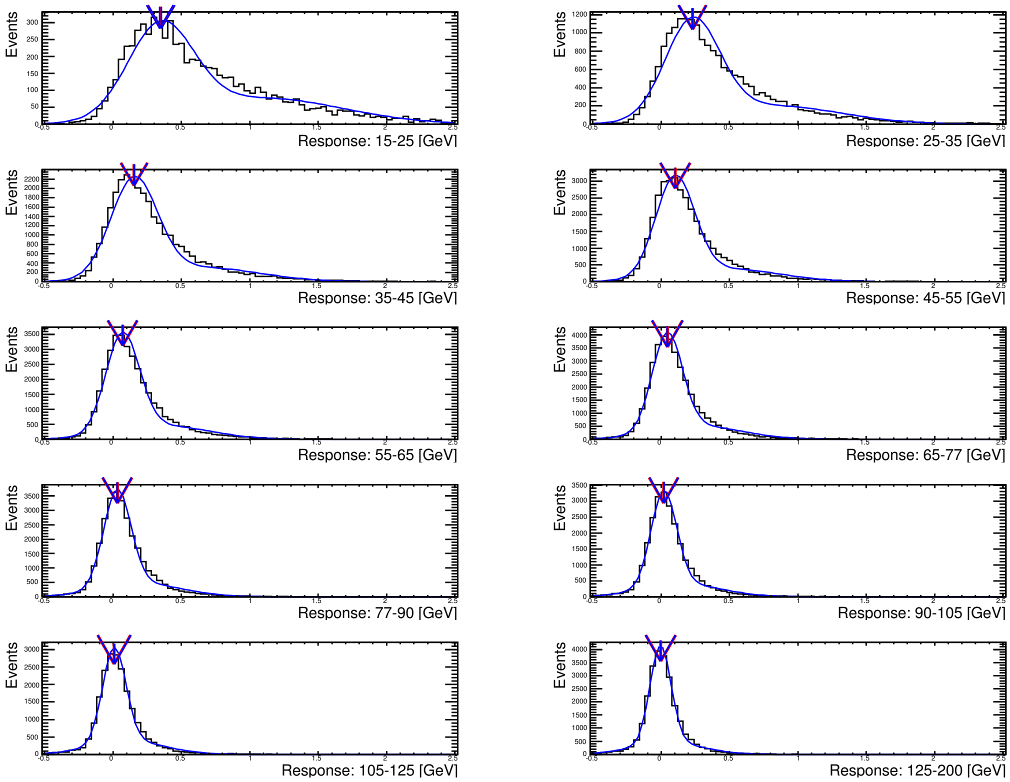

Figure 5.5: Diagrams showing double gaussian fits to gain the most probable value of the average response for each p_T bin of b-jets. The most probable value is represented by the blue arrow which is the mean of the gaussian modelling the peak.

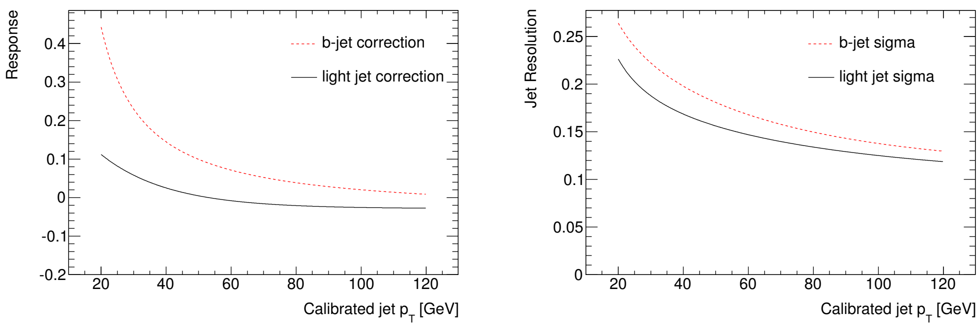

(a) (b)

Figure 5.6: Plots showing the (a) jet transfer and (b) resolution functions derived for b-jet and light quark jets

ditional corrections for identified photons, electron, muons, and jets. The electrons, muons and jets used in the calculations are consistent with the definitions stated in the previous sections. Any energy corrections applied to the event objects are propagated through to the $E_{\mathrm{T}}^{\mathrm{miss}}$. By using the final objects with their full calibrations an improved $E_{\mathrm{T}}^{\mathrm{miss}}$ resolution is achieved as the calibrations of specific objects are better than the generic calibrations of individual cells, where there is no knowledge of the source of the energy deposit. Knowledge of the gaps in detector coverage, the shielding of the calorimeter by the cryostat and dead regions is taken into account in the $E_{\mathrm{T}}^{\mathrm{miss}}$ reconstruction. Electronic noise in the calorimeters can also cause mis-measurement of the $E_{\mathrm{T}}^{\mathrm{miss}}$; this is alleviated by only using calorimeter deposits above a cell's noise threshold and by using topoclusters which already take into account noise suppression [41].

5.7 Scale Factors

A series of corrective scale factors is applied to normalise the MC samples, removing measurable discrepancies between the response of various effects in data and MC. The largest scale factor applied is to correct the efficiency of b-tagging in MC to the lower efficiency level measured in data. This factor is p_T dependant and applied for each tagged jet found in the event; across the whole p_T range the factors are of order 0.9. It is applied to events by randomly dropping the tag on a jet if a random number is rolled above the scale factor. Smearing and rescaling functions are applied to the leptons to account for differences in the resolution and scales seen in data. The resulting corrections to the leptons p_Ts are carried through into the $E_{\mathrm{T}}^{\mathrm{miss}}$ so it remains consistent with the event. Further scale factors are applied to account for data versus MC differences in lepton identification and reconstruction efficiencies. For the muons this weight is a constant whereas the electron scale factor is p_T dependant. A final set of factors are applied to correct for inconsistencies between the trigger efficiency seen in data and that modelled by MC, for these the electron scale factor is a constant whereas the muon ones are p_T dependant. The lepton reconstruction and trigger scale factor corrections are significantly smaller than the b-tag efficiency corrections and are all of order one [47].

Chapter 6

Monte Carlo and Data Samples

6.1 Monte Carlo Generators

To model the kinematics of the signal and background processes expected in this analysis Monte Carlo (MC) generators are used. MC generators use the theoretical knowledge of the required processes to produce a sample of simulated events which can reproduce the yields and distributions expected in the recorded data. MC events are produced using random numbers to pick event kinematics from the theoretical distributions so that as the number of events produced increases the phase space of the process is filled completely.

To produce a full MC event from the initial pp collision through to the final energy deposits in the various sub-detectors of ATLAS a series of steps need to be followed. A generator begins by producing a matrix element level simulation of the central hard scatter process at a given order in perturbation theory. This models the probability of two incoming partons interacting and producing a set of final state partons. At ATLAS next-to-leading order, in α_s, generators are often used, where the possibility of the radiation of an additional gluon or quark is included in the hard scatter process.

The hard scatter process has to be connected back to the initial pp state. The incoming partons present in the hard-scatter process originate from the ensembles present in the colliding protons. Parton distribution functions (PDFs) [52, 53] give the probability of a parton carrying a momentum fraction x of the incident proton's p_z. These PDFs have been produced from many previous measurements of processes such as deep inelastic scattering. Experiments such as the ZEUS and H1 experiments at the HERA accelerator in DESY have measured electron-proton scattering and the results have been extensively analysed to produce PDFs which can then be evolved to the required energy scales. The incoming partons in the hard process are evolved backwards in time to try to match a likely parton present in the proton. This process leads to radiation of gluons from the initial state partons as the hard scatter parton's energy is matched to a parton in the PDFs.

Final state radiation is then modelled for the final particles present in the hard process. This is known as parton showering and models the likelihood of the final state particles to emit a gluon with momentum above a set cut off scale. The parton shower produces a series of emissions to bring the shower from the hard scatter energy scale down to the cut off scale. The final state partons of the process need to be evolved to the final stable particles through hadronisation. This produces jets of hadronic particles from the partons present in the final state; as the detector does not see unbound partons, instead only the hadronic jets produced as a result of quark confinement. Any remaining unstable particles are also decayed at this point leaving only stable final particles in the event.

The underlying event is the result of the remnants of the protons after the collision. This must be included in the MC description of the event. The underlying event includes contributions from multiple parton interactions where secondary partons undergo hard scatters and also the interactions of the remaining beam-beam remnants. In-time pileup originates from secondary pp interactions occurring within the same bunch crossing. It is modelled by the inclusion of 'min-bias' events to provide additional interaction vertices, reproducing the expected distribution of the number of vertices. The whole event is then passed through a detector simulation to model the response of such an event in ATLAS [54]. GEANT4 [**?**] is used to model ATLAS and contains information on the geometry and detector material present. The event is then ready to be analysed in the same way as a real data event from ATLAS.

6.2 Monte Carlo Samples

As shown in Chapter 2 the dominant production mode for light charged Higgs at the LHC is via the decay of the top quark, $t \to H^+b$. Therefore both the signal and main irreducible $t\bar{t}$ background have the kinematics of a semi leptonic $t\bar{t}$ decay. The remaining backgrounds to the H^+ signal are; QCD multi-jet, W/Z+jets, $Wb\bar{b}$+jets, single-top and dibosons events. The full list of signal and background MC generators used to produce the signal and background MC events are listed in Tables 6.1, 6.2 and 6.3. In the tables, the cross-section values including k-factors and branching ratios are listed.

6.2.1 Signal Samples

Process	σ [pb]	Generator	N_{MC}
$H^+ \to c\bar{s}$, 90 GeV	9.87	Pythia	100k
$H^+ \to c\bar{s}$, 110 GeV	9.87	Pythia	100k
$H^+ \to c\bar{s}$, 130 GeV	9.87	Pythia	100k

Table 6.1: Signal Monte Carlo samples are shown with the assumed cross-section including k-factors and branching ratios. The branching ratio $\mathcal{B}(t \to bH^+) = 0.1$ is assumed, which is close to the Tevatron limit.

The signal process, shown in Figure 2.10, for this analysis is modelled by the leading order MC generator Pythia [55] and the AMBT1 [56] tune. Pythia was used to generate the entire event from hard scatter through the parton shower, hadronisation and the underlying event. Large samples have been produced at three separate mass points: 90, 110 and 130 GeV. For the signal cross-sections, the branching ratio $\mathcal{B}(t \to H^+b) = 0.1$ is initially assumed, which is close to the Tevatron limit. These samples are forced to decay to semi-leptonic events by requiring one top to decay as $t \to bH^+$ with the $\mathcal{B}(H^+ \to c\bar{s}) = 100\%$ and the second top forced to decay leptonically.

6.2.2 Standard Model $t\bar{t}$ Samples

The SM $t\bar{t}$ MC provides the main irreducible background to the signal sample as the signal is itself a semi-leptonic $t\bar{t}$ decay. A large SM $t\bar{t}$ sample containing semi-leptonic and dileptonic decays, shown in Figures 2.9 and 2.8 respectively, has been generated using the next to leading order MC generator MC@NLO [57, 58] using the AUET1-CTEQ66 [59] tune. This was coupled with HERWIG [60] to provide the showering and hadronisation modelling. The underlying event was modelled by JIMMY [61]. The fully hadronic decays were produced as a separate sample using the same three generators. It would have been desirable to model the signal and background with the same generator combination to reduce the change of systematics between the samples. However the $H^{+} \to c\bar{s}$ is not currently included as a hard-scatter process in MC@NLO.

As the semi-leptonic $t\bar{t}$ channel is the main background to the signal process a set of systematic samples of the semi-leptonic decay have been produced. A sample with the matrix element produced by POWHEG [62, 63, 64, 65] is used to assess systematic effects arising from using a different MC generator. A further POWHEG sample showered by PYTHIA allows the study of a different showering model. Initial state and final state radiation variations are accessed using ACERMC [66] samples. Details of these systematic effects will be expanded upon in Chapter 8.

6.2.3 Single Top Samples

A small background to $t\bar{t}$ events comes from the three single top production channels: the s, t and Wt channels, examples of which are shown in Figure 6.1. These backgrounds mimic semi-leptonic $t\bar{t}$ decays when the top quark decays leptonically and initial or final state radiation provides additional high-p_T jets. The largest background contribution comes from the $Wt \to WWb$ channel as it has the highest cross section at the LHC and it contains two real W bosons it closely mimics the $t\bar{t}$ system. These channels have all been modelled using the same MC@NLO+HERWIG generator combination as the default $t\bar{t}$ samples.

Process	σ [pb]	Generator	N_{MC}
$t\bar{t}$ no fully hadronic	89.7	MC@NLO+HERWIG	1,000k
$t\bar{t}$ fully hadronic	74.9	MC@NLO+HERWIG	150k
Systematic Samples			
$t\bar{t}$ no fully hadronic	89.4	POWHEG+HERWIG	200k
$t\bar{t}$ no fully hadronic	89.4	POWHEG+PYTHIA	200k
$t\bar{t}$ no fully hadronic	89.1	ACERMC+PYTHIA	200k
$t\bar{t}$ no fully hadronic ISR up	89.1	ACERMC+PYTHIA	200k
$t\bar{t}$ no fully hadronic ISR down	89.1	ACERMC+PYTHIA	200k
$t\bar{t}$ no fully hadronic FSR up	89.1	ACERMC+PYTHIA	200k
$t\bar{t}$ no fully hadronic FSR down	89.1	ACERMC+PYTHIA	200k
Single top $W + t$-channel all decays	14.58	MC@NLO+HERWIG	200k
Single top t-channel (lepton+jets)	7.15	MC@NLO+HERWIG	200k
Single top s-channel (lepton+jets)	0.468	MC@NLO+HERWIG	10k

Table 6.2: Top background Monte Carlo samples are shown with the cross-section including k-factors and branching ratios.

6.2.4 W+jets Samples

The W+jets events, shown in Figure 6.2, have large cross sections at $\sqrt{s} = 7$ TeV. Again these backgrounds mimic the $t\bar{t}$ system when a W boson decaying leptonically combined with emission of additional jets. Pairs of b-jets can be produced in association with a W boson, increasing the probability of the event passing cuts to select $t\bar{t}$ events. These events are however rare compared to the production of a W boson with a pair of light jets. These background channels were modelled using the leading order MC generator ALPGEN [67, 68, 69]. ALPGEN can provide a leading order matrix element with up to six additional partons in the final state. The ALPGEN samples are coupled to HERWIG and JIMMY using the CTEQ6L1 PDFs [59].

Process	σ [pb]	Generator	N_{MC}
$W \to \ell\nu$ + 0 parton	8,400	ALPGEN+HERWIG	1,382k
$W \to \ell\nu$ + 1 partons	1,580	ALPGEN+HERWIG	640k
$W \to \ell\nu$ + 2 partons	460	ALPGEN+HERWIG	190k
$W \to \ell\nu$ + 3 partons	123	ALPGEN+HERWIG	50k
$W \to \ell\nu$ + 4 partons	31	ALPGEN+HERWIG	13k
$W \to \ell\nu$ + 5 partons	8.5	ALPGEN+HERWIG	3.5k
$W + bb$ + 0 parton	3.2	ALPGEN+HERWIG	6496
$W + bb$ + 1 partons	2.6	ALPGEN+HERWIG	5500
$W + bb$ + 2 partons	1.4	ALPGEN+HERWIG	2998
$W + bb$ + 3 partons	0.6	ALPGEN+HERWIG	5500
$Z \to \ell\ell$ + 0 parton	807.5	ALPGEN+HERWIG	304k
$Z \to \ell\ell$ + 1 partons	162.6	ALPGEN+HERWIG	64k
$Z \to \ell\ell$ + 2 partons	49.2	ALPGEN+HERWIG	20k
$Z \to \ell\ell$ + 3 partons	13.7	ALPGEN+HERWIG	5.5k
$Z \to \ell\ell$ + 4 partons	3.3	ALPGEN+HERWIG	1.5k
$Z \to \ell\ell$ + 5 partons	1.0	ALPGEN+HERWIG	0.5k
WW	17.0	HERWIG	15k
WZ	5.5	HERWIG	45k
ZZ	1.3	HERWIG	150k

Table 6.3: Bosonic background Monte Carlo samples are shown with the cross-section including k-factors and branching ratios.

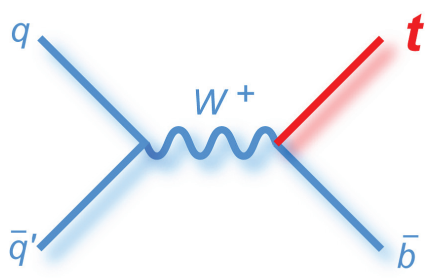

(a)

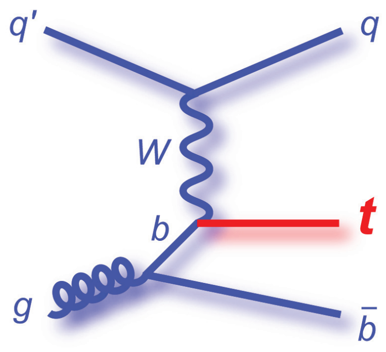

(b)

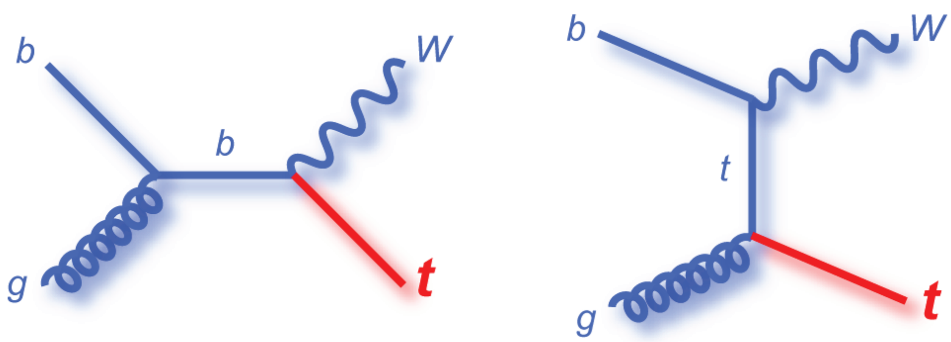

(c)

Figure 6.1: Diagrams showing the production channels for single top decays, (a) shows the s-channel tb production, (b) shows the t-channel tbq production and (c) shows Wt production.

6.2.5 Other Non-$t\bar{t}$ Background Samples

Z+jets events provide a very small background to the semi-leptonic $t\bar{t}$ system. They are produced in similar diagrams to the W+jets backgrounds. They however have a much lower cross section. The presence of two leptons combined with the lack of a neutrino in the final state means this background is easily removed by kinematic cuts for semi-leptonic $t\bar{t}$ events. The Z+jets events are produced using the same ALPGEN and HERWIG combination as the W+jets events. Diboson backgrounds, for example WW production shown in Figure 6.3, can provide a similar final state to $t\bar{t}$ events, especially WW events which can mimic the W bosons present in the final state. However the

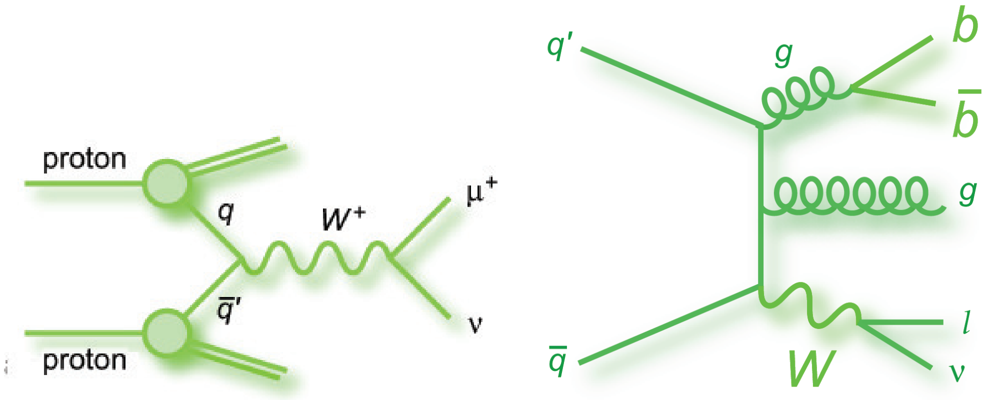

(a) (b)

Figure 6.2: Diagrams showing the production channels for W+jets events, (a) shows the diagram for W production, (b) shows a possible diagram for W production in association with a pair of heavy-flavour jets

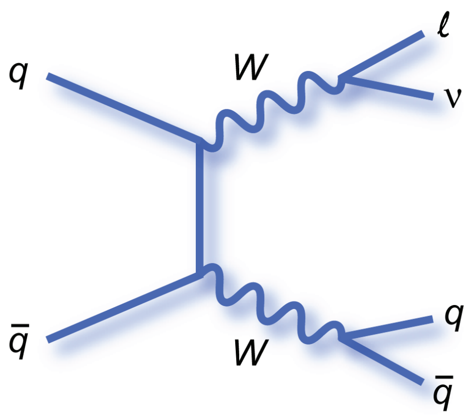

Figure 6.3: Diagram showing WW production.

cross section for these processes is amongst the lowest SM processes studied at hadron colliders at around 1 – 20pb, thus resulting in a small contribution to the total background. The diboson backgrounds are produced using Herwig for the full simulation chain.

6.3 Data sample

The analysis presented here uses $\sqrt{s}$ =7 TeV proton-proton collision data recorded between June and November 2010 by the ATLAS experiment. Semi-leptonic $t\bar{t}$ events are characterised by multiple high p_T jets, a high p_T lepton and large missing E_T. These events need to be selected efficiently whilst simultaneously rejecting some of the dominant backgrounds, such as QCD dijet production. High p_T lepton triggers offer excellent QCD rejection. QCD events tend not to contain isolated leptons and only pass high p_T lepton triggers via the presence of fake or non-prompt leptons. Lepton triggers can remain un-prescaled at relatively low p_T values by making quality and isolation requirements. Lepton triggers also have have fast turn-on curves (i.e., the efficiency plateaus near the threshold), allowing selection cuts to be made at relatively low p_T's as the triggers rapidly reach plateau. Using these triggers therefore efficiently selects a sample containing semi-leptonic $t\bar{t}$ events and rejects a large percentage of the QCD background. The size and kinematics of the remaining QCD multi-jet background is estimated from data driven methods outlined in Chapter 7. The muon triggers used p_T thresholds varying from 10 to 13 GeV, whereas the electron trigger p_T remained constant at 15 GeV throughout the periods. The triggers used for each data period are detailed in Table 6.4.

The data selected by the lepton triggers is also filtered using a Good Runs List (GRL). This list makes selection requirements due to the beam and detector conditions when the data were recorded. The GRL requires that the data was recorded when the LHC was in a condition of stable beams; meaning the beams have been ramped to full energy and are circulating steadily. Good data quality flags are required for all detector systems critical to muon, electron and jet identification, and $E_{\mathrm{T}}^{\mathrm{miss}}$ determination. The GRL can reject data periods from individual luminosity-blocks through to entire runs. By doing this specific data problems can be avoided if the data taking period they affect is known. After these trigger and GRL requirements the resulting dataset corresponds to an integrated luminosity of 35 pb^{-1} [70]. Assuming a fully efficient trigger and the theoretical $\sigma_{t\bar{t}}$ = 164.6pb at $\sqrt{s}$ = 7 TeV this data sample should contain around 2600 semi-leptonic $t\bar{t}$ decays before any selection criteria.

Data period	Muon Trigger	L, [pb^{-1}]	Electron Trigger	L, [pb^{-1}]
E4-E7	EF_mu10_MSonly	0.5	EF_e15_medium	0.5
F	EF_mu10_MSonly	1.5	EF_e15_medium	1.5
G1-G5	EF_mu13	4.3	EF_e15_medium	4.3
G6	EF_mu13_tight	1.2	EF_e15_medium	1.2
H	EF_mu13_tight	6.9	EF_e15_medium	6.9
I	EF_mu13_tight	20.7	EF_e15_medium	20.7

Table 6.4: Triggers used for the different data periods. For MC, EF_mu13_tight and EF_e15_medium were used. The luminosity recorded with each trigger is also shown.

Chapter 7

Analysis

The analysis presented in this thesis considers a potential non-SM decay of top quarks, $t \to H^+b$, with the charged Higgs boson subsequently decaying to two jets [71]. The search is performed in the semi-leptonic $t\bar{t}$ channel looking for events where one top decays hadronically via the charged Higgs and the other top decays leptonically, via $t \to W^-\bar{b}$. The analysis initially needs to select semi-leptonic $t\bar{t}$ events from the data recorded by ATLAS whilst simultaneously rejecting unwanted background events. From this selection of events, the two jets forming the W/H^+ dijet system need to be identified. To allow the correct assignment of jets to the dijet system, the entire $t\bar{t}$ system is reconstructed. This chapter will first outline the selection criteria used and then describe the background estimation methods. It will go on to describe the reconstruction of the full $t\bar{t}$ system to provide the reconstruction of the dijet mass distribution. This distribution is then used to search for a secondary mass peak at m_{H^+} originating from charged Higgs decays. The statistical methods used to perform this search are described in Chapter 9 and the results are presented in Chapter 10.

7.1 Event selection criteria

A series of kinematic and event cleaning requirements are applied to efficiently select semi-leptonic $t\bar{t}$ events while rejecting the non-$t\bar{t}$ backgrounds. The pre-selection requirements used to select the physics objects considered have been outlined in Chapter 5. These requirements have already been applied to the events reaching this stage of the analysis. The data sample has been initially selected from data streams triggered by any electron or muon trigger. The events are also requested to pass the requirements made by the good runs list. The final selection requirements used in this analysis are as follows:

Cut 1. Require the event to have passed the relevant single electron OR muon trigger.

The data has by definition already been triggered by a lepton trigger, but possibly a low p_T one. The data is therefore required to have passed one of the high p_T lepton triggers mentioned in Table 6.4. The MC events are passed through an offline simulation of the trigger system. They are required to pass one of the same triggers as the data.

Cut 2. Require events to contain a primary vertex with > 4 associated tracks.

The purpose of this cut is to remove non-collision backgrounds. Vertices from from cosmic-ray or beam-gas events tend to have a low number of associated tracks. The primary vertices in collision events are the result of real interactions and therefore are the origin of a multitude of tracks.

Cut 3. Require exactly one electron object, OR exactly one muon object.

Here the analysis requires the event to contain only a single lepton with a t$p_T >$ 20 GeV, falling within a well instrumented area of the detector. Signal and SM $t\bar{t}$ background events are expected to contain a single high p_T lepton to be present from the leptonic decay of one of the W bosons. This cut reduces SM background events containing low p_T, fake or multiple leptons. The lepton found is required to match the trigger object within $\Delta R < 0.2$. By requiring exactly one lepton this cut separates the analysis into two orthogonal channels containing muon and electron events separately. This allows further selection cuts to be tailored to the specific kinematics of each channel and to allow the separate handling of data driven backgrounds.

Cut 4. Require the event to have $E_{\mathrm{T}}^{\mathrm{miss}} > 35$ GeV for the electron channel, OR $E_{\mathrm{T}}^{\mathrm{miss}} > 20$ GeV for the muon channel.

This selects events with a high $E_{\mathrm{T}}^{\mathrm{miss}}$ expected from the neutrino present in semi-leptonic $t\bar{t}$ events. This makes a further reduction in QCD multi-jet events where $E_{\mathrm{T}}^{\mathrm{miss}}$ only occurs through mismeasurement of the energy of detector objects and therefore is likely to be low. The asymmetry in the thresholds arises from an optimisation of the cuts in the electron channel improving the modelling and rejection of the QCD multi-jet background.

Cut 5. Transverse W mass required to be $M_t(W) > 25$ GeV for the electron channel, OR $E_T^{miss} + M_t(W) > 60$ GeV for the muon channel.

$M_t(W)$ here is defined as the transverse mass of the lepton and $E_{\mathrm{T}}^{\mathrm{miss}}$ present in the event. In $t\bar{t}$ events the $M_t(W)$ distribution will peak around 80 GeV due to the presence of a real W. In the QCD multi-jet background the distribution will not form such a peak. The two components are not from a W decay but arise from misidentifications and mismeasurements. Again the asymmetry between the two cuts originates from the optimisation made in parallel with the $E_{\mathrm{T}}^{\mathrm{miss}}$ cut.

Cut 6. Select events containing at least four jets with $E_T > 25$ GeV and $|\eta| < 2.5$.

A semi leptonic $t\bar{t}$ event will typically contain at least four high p_T jets from the hadronic W decay and the two b-quarks. This cut is highly efficient at removing the vector boson backgrounds, where jets are from additional gluon emissions from the hard scatter which tend to be lower in p_T. The jets found are required to be in a central region, $|\eta| < 2.5$. Jets found here are in general well reconstructed and have lower uncertainties. This is important as the final discriminating variable is highly sensitive to JES uncertainties. Events containing a poorly reconstructed or 'bad' jet with a $p_T > 10$ GeV are rejected in the data at this point.

Cut 7. Require at least one of the four leading jets to be b-tagged

Here b-tagged jets are defined as in Chapter 5, using the secondary vertex tagger weight SV0 > 5.85. This criteria is efficient at removing further non-$t\bar{t}$ backgrounds as the jets present in QCD multi-jet and W/Z+jets events are more likely to be light flavour jets and therefore likely to not be b-tagged. There are typically two b-jets present in the $t\bar{t}$ system. Therefore requiring two b-tags would offer a very pure $t\bar{t}$ sample. Only a single b-tag is required in early data due to the b-tagging efficiency of 50% per b-jet provided by the simple secondary vertex tagger. The efficiency of a double tagged cut is prohibitive with the small early data set of 35pb^{-1}. The single b-tag therefore offers the balance between background rejection and statistics retention, an important consideration in a small sample.

By the end of the full selection cuts the analysis is now in possession of a set of events with kinematics that closely resemble the expectations for a semi-leptonic $t\bar{t}$ event, i.e., four high p_T jets, at least one of which is b-tagged and a high p_T lepton combined with $E_{\mathrm{T}}^{\mathrm{miss}}$ from the leptonic decay of a W boson. These events will be used to form a dijet mass distribution by fully reconstructing the $t\bar{t}$ system and ascertaining the most probable assignment of jets to partons. The dijet system can then be used to search for a secondary mass peak from H^+ decays. The b-tagging information is used to constrain the number of valid assignment choices and thus reduce the chance of combinatorial errors.

7.2 Signal background estimation

7.2.1 MC Background Estimates

The majority of the backgrounds used in this analysis are modelled by MC alone. The generators used to produce the MC samples have been outlined previously in Chapter 6. The samples are normalised to the NLO cross sections multiplied by the luminosity of the recorded data sample. The normalised samples are then passed through the full selection criteria, providing a description of the data seen. The largest contributions from MC modelled events are the dominant irreducible $t\bar{t}$ background and the large

W+jets background. The quality of the MC description of the W+jets background will be explored later in this chapter. The smaller backgrounds modelled by MC are the single top, diboson and Z+jets backgrounds.

7.2.2 Data Driven Background Estimate

As stated in Chapter 6, data driven methods are used to estimate the QCD multi-jet backgrounds. The accurate MC modelling of fake leptons in QCD multi-jet events is problematic. Fake leptons can for example originate from inflight leptonic decays of π/K mesons, the leptonic decay of heavy mesons (those containing c/b- quarks) or the mis-identification of hadronic jets as electrons. These processes are rare, therefore requiring large statistical samples of QCD multijet events to model them accurately. The relative contributions of the different sources of fakes also have large systematic uncertainties. Using data driven methods to estimate the QCD multijet background removes the large uncertainties arising from the poor MC modelling of QCD multijet events containing fake leptons. The muon and electron channels in this analysis each use a separate method to estimate the both the size and shape of the QCD multi-jet backgrounds; the 'matrix method' in the muon channel and a fit based method in the electron channel. Both of these methods share common features by searching in a 'side band' region of the data to obtain a background dominated sample, modelling this sample and extrapolating it to the signal region. In early data these methods can suffer from low statistics however they are still preferable to producing large MC datasets.

7.2.3 μ+jets channel: The 'Matrix Method'

In the μ+jets channel, semi-leptonic $t\bar{t}$ events with 'real' muons are predominantly 'faked' by QCD multi-jet events with final states containing a non-prompt muon. For example non-prompt muons can originate from the leptonic decay of a heavy mesons containing c/b-quarks or inflight decays of π/K mesons. To estimate the contribution from this type of event in the data a 'matrix method' [47] estimate has been performed. The method begins by defining a loose and a tight muon sample in the recorded data. Here the tight sample is selected by the cuts outlined earlier in this chapter: the loose sample follows the standard cuts but removes the isolation requirements made in the pre-selection of the muon objects. Loosening the isolation criteria increases the QCD multi-jet background contribution as non-promt muons from heavy quark decays are not generally isolated from the calorimeter deposits of the jet they originate from. The numbers of events selected in data by the loose and standard criteria, N^{loose} and N^{std}, can be therefore written as:

$$N^{loose} = N^{loose}_{real} + N^{loose}_{fake}, \tag{7.1}$$

$$N^{std} = \epsilon_r N^{loose}_{real} + \epsilon_f N^{loose}_{fake}, \tag{7.2}$$

where ϵ_r and ϵ_f are the efficiencies for 'real' and 'fake' loose muons to pass the standard selection. These efficiencies are measured in the data in control samples with large fractions of prompt and non-prompt muons. The fraction of 'real' muons is estimated in an inclusive control sample of $Z \to \mu^+\mu^-$ where the majority of muons are expected to be prompt from the Z decay. Here the real efficiency from prompt muons is measured to be $\epsilon_r = 0.990 \pm 0.003$. Two control regions are used to estimate the non-prompt muon efficiency; sample A requires events with a low $E_{\mathrm{T}}^{\mathrm{miss}} < 10$ GeV and at least one high p_T jet and sample B requires the normal $E_{\mathrm{T}}^{\mathrm{miss}} > 20$ GeV requirement with at least one high p_T jet with the additional requirement of a large muon impact parameter. Sample A is dominated by QCD multi-jet events which in general have a low $E_{\mathrm{T}}^{\mathrm{miss}}$ value due to the lack of neutrinos. After removing contamination from W/Z events containing prompt muons the fake muon efficiency is measured to be $\epsilon_f = 0.382 \pm 0.007(stat.)$ from sample A. Sample B selects a sample enriched with events where a muon has originated from a secondary vertex, consistent with the leptonic decay of a heavy quark. From this sample the fake muon efficiency is measured to be $\epsilon_f = 0.295 \pm 0.025(stat.)$. An unweighted average of the two samples is taken as the final efficiency, $\epsilon_f = 0.339 \pm 0.013(stat.) \pm 0.061(syst.)$. Both selections are run on the data and a weight is calculated for each event are defined as:

$$W_{loose} = (\epsilon_f \epsilon_r)/(\epsilon_r - \epsilon_f), \tag{7.3}$$

$$W_{tight} = (\epsilon_f(\epsilon_r - 1))/(\epsilon_r - \epsilon_f). \tag{7.4}$$

Applying these weights to the data events selected provides an estimate of the QCD multi-jet contribution in the μ+jets channel, providing both the number of expected events, as shown in Table 7.2, and the shape of the QCD multi-jet distribution. Each event selected by the loose criteria only provides a positive contribution to the modelling whereas each selected by both loose and tight lead to a small negative contribution. The method is therefore sensitive to low statistics in the loose data selection. However it provides a reasonable model and is preferential to MC methods.

7.2.4 e+jets channel: The Template Fit

In the e+jets channel there are additional sources of fake leptons. These can be non-prompt electrons, for example from photon conversions, or fake electrons from hadronic jets with high electromagnetic fractions. These additional sources have relatively large contributions to the QCD multi-jet background. The matrix method could also be used to describe the electron background. However the fakes found in the control region are not guaranteed to have the same composition compared to the signal region. If the matrix method was used such differences could introduce a bias in the extrapolation of the fake efficiency to the signal region. Therefore, the size of the QCD multi-jet background contribution has been estimated from a binned likelihood template fit of the E_T^{miss} distribution in data [47]. The fit uses four template distributions QCD multi-jet, $t\bar{t}$, W + jets and Z + jets. The QCD multi-jet template is obtained from two data control regions, 'jet-electrons' and 'non-electrons'. In the first region events are selected with standard cuts, the electron is however replaced with a hadronic jet object. This jet is required to pass the electron kinematic cuts, have at least four inner detector tracks and an f_{EM} of 80-95%, where f_{EM} is the fraction of the jets energy deposited in the EM calorimeter. This selection leads to a sample predominately composed of events containing a jet appearing in the detector like an electron. In the second region the electron track quality requirements are dropped in the inner layers of the tracker, thus increasing the contamination of the sample by photons. The likelihood fits to the data are performed using these two QCD multi-jet templates in a control region with $E_T^{miss} < 20$ GeV and the $M_t(W)$ requirement removed. The result of both fits is ρ_{QCD} which is the predicted fraction of QCD multi-jet events assuming the QCD multi-jet background has a 100% contribution from either jet-electrons or non-electrons. As these samples are not true representations of the true background an unweighted average of ρ_{QCD} from the two QCD multi- jet templates is taken and extrapolated into the signal region. The observed number of events in data is then used to estimate the final expected QCD multi-jet contribution in the e+jets channel. The averaged QCD multi-jet template is rescaled to the ρ_{QCD} fraction of the observed data.

7.3 χ^2 Kinematic Fitter

The presence of a H^+ boson in $t\bar{t}$ decays will lead to a secondary dijet mass peak centred around m_{H^+} and a variation in the observed number of events. The shape and normalisation of invariant mass of the dijet system originating from the hadronically decaying boson present in the semi-leptonic $t\bar{t}$ system will be used as the discriminating variables in this analysis. To reconstruct the dijet mass originating from the decays of W^+ or $H^+ \rightarrow qq$, the two jets need to be correctly identified in the $t\bar{t}$ event. Using prior knowledge of m_t and m_W the $t\bar{t}$ system can be fully reconstructed. To do so the jets present in the selected events must be correctly assigned to the partons of the original system. By reconstructing the $t\bar{t}$ system the dijet mass distribution can be recovered. Clearly an incorrect assignment of jets to partons in the $t\bar{t}$ system will destroy the kinematics of the system and therefore the discriminating power of the dijet mass will be lost. In order to correctly identify the two jets forming the dijet system, a kinematic fitter, based upon a χ^2 function is used. The fitter performs the jet assignment and fully reconstructs $t\bar{t}$ events by considering the most likely combination of the four jets, lepton and the $E_{\mathrm{T}}^{\mathrm{miss}}$. The fitter also aims to improve the dijet mass resolution to enhance the separation between signal and background events. Prior to the fit the signal and background dijet distributions tend to be poorly separated with broad peaks and long tail to high masses, shown in Figure 7.1. Events with incorrectly assigned jets form a combinatorial background which lies under the main peaks of the distributions. As m_{H^+} tends towards m_W, differentiating the two distributions becomes increasingly

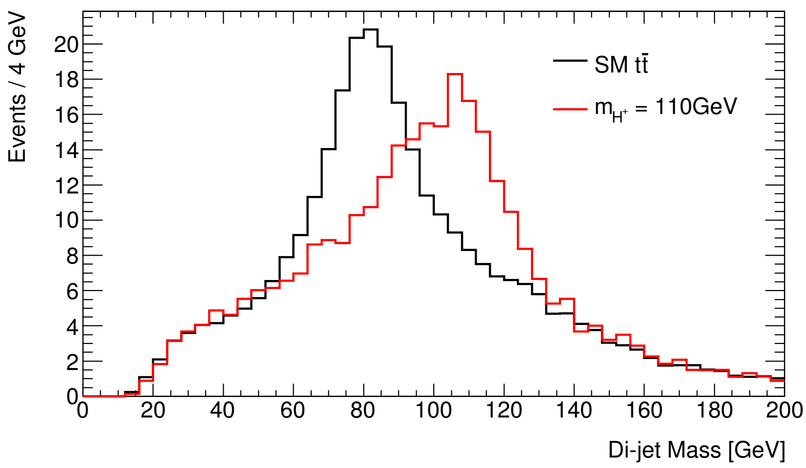

Figure 7.1: The dijet mass distribution (both channels combined) for the reconstructed H^+, m_{H^+} = 110 GeV, and W-bosons prior to the kinematic fit.

difficult as the distributions merge.

Initially the possible jet-parton assignments available for the fitter to consider must be identified. Tagging information provides constraints on the possible combinations. It is assumed that tagged jets can only be assigned to b-quarks. In a perfect scenario where the leading four jets in the event originate from the $t\bar{t}$ decay, both b-jets present have been tagged and the lepton and neutrino from the leptonic W have been well measured, reconstruction of the $t\bar{t}$ system is trivial. In this case there are only two valid combinations for matching the jets from the top quark decays to the four original partons. The jets from the decay of the $W^{\pm}$ or $H^{\pm}$ are indistinguishable in terms of assignment, therefore only leaving a choice in attributing the b-tagged jets to the leptonic or hadronic top decays. For single tagged events the constraint from the b-tagging has been partially lost and therefore there are 6 distinct jet combinations possible. Each of these are valid possible combinations of the jets available and are considered by the fitter.

Unfortunately in the crowded hadron collider environment of ATLAS, jet assignment is not an insignificant task. Although kinematically favoured, there is no guarantee that the four jets needed to reconstruct the $t\bar{t}$ system lie within the four leading p_T jets in the event. Final state radiation can reduce the energy of a parton from a top decay or a high p_T jet from a secondary interaction could also displace a jet. If even one of the 'correct' jets in an event has lower p_T than the fourth highest p_T jet then obviously no combination of the leading four jets will yield a correct reconstruction of the system. In order to recover these events it is necessary to consider jets outside the leading four. Monte Carlo studies were made using the MC truth information to ascertain the fraction of events where a jet from a top decay had p_T lower than the four highest p_T jets. At least one quark was matched to the fifth jet or beyond in one third of $t\bar{t}$ events. Most of these quarks were matched to the fifth jet. To recover these events the fifth jet was allowed to be considered in the jet combinations passed to the fitter. The fifth jet was only allowed to be swapped with one of the lower two p_T jets, reducing the combinations to be assessed but still recovering lost events. A separate problem occurs as m_{H^+} approaches $m_{\rm top}$ as the energy available to the b-jet decreases, thus skewing the p_T distribution towards softer b-jets. These b-jets are therefore more likely to fail the jet p_T requirements or have p_T lower than the four highest p_T jets therefore increasing the combinatorial background.

7.4 The Fit

In the fitting process the measured momenta of the final state particles are allowed to vary within their experimental resolutions, while their η and ϕ remain fixed. By rescaling the measured p_T values the dijet mass resolution can be improved and the full $t\bar{t}$ system reconstructed. For each jet combination two jets are assumed to be the b-jets and the remaining two jets form the dijet system. Tagged jets were always considered as b-jets, unless three or more jets are tagged. For each combination considered the jet transfer functions described in Chapter 5 were applied. The b-jet transfer functions are applied to the assumed b-jets, even if the jet is untagged. The light-quark jet transfer functions are applied to the two jets assumed to originate from the dijet system.

The full neutrino momentum has to be calculated to allow the reconstruction of the leptonically decaying W-boson. The transverse momentum of the neutrino, $p_T(\nu)$, is inferred from the E_T^{miss} measured by ATLAS. The longitudinal momentum component of the neutrino, $p_L(\nu)$, is missing as the total p_z of the system is an unknown. By constraining the mass of the leptonically decaying W-boson to be 80.4 GeV, $p_L(\nu)$ can be expressed in terms of the known quantities of the system: $p_T(\nu)$ and the lepton momentum p_l. This results in a quadratic equation in $p_L(\nu)$ which provides two solutions for each permutation of the jet assignment. The full calculation used to calculate $p_L(\nu)$ is shown in Appendix B.

To describe the kinematics of the semi-leptonic $t\bar{t}$ event the following χ^2 function is used, and its value minimised by varying its components using the MINUIT [72] algorithm,

$$\begin{aligned}\chi^2 &= \sum_{k=jjb,bl\nu} \frac{(M_k - M_{top})^2}{\sigma_{top}^2} \\ &+ \sum_{i=l,4jets} \frac{(p_T^{i,fit} - p_T^{i,meas})^2}{\sigma_i^2} \\ &+ \sum_{j=x,y} \frac{(p_j^{RE,fit} - p_j^{RE,meas})^2}{\sigma_{RE}^2}. \end{aligned} \tag{7.5}$$

The first term in this function constrains the mass of the leptonic, $l\nu b$, and hadronic, jjb, top systems in the semi-leptonic event to be within the top width, $\sigma_{top} = 1.5$ GeV, of the assumed top mass $M_{top} = 172.5$ GeV. These two requirements place the initial constraints on the system. They allow separation between true $t\bar{t}$ events and backgrounds which contain no tops. The second term allows the measured values of the jets and the lepton to vary within the experimental uncertainties. The jets are allowed to vary within the σ_{jet} taken from the p_T parameterisation, as derived in Section 5.5, for the jet flavour currently under consideration. The final term allows the remaining energy, RE, present in the event to be rescaled within its uncertainty. The remaining energy is calculated using additional information from a looser jet selection, lowering the p_T threshold to 15 GeV. All jets above this threshold are summed to give an overall vector describing additional jet activity. The sum of jet activity, lepton p_T's and $E_{\mathrm{T}}^{\mathrm{miss}}$ are then subtracted from a null vector. This gives the final remaining energy value representing the net calorimeter energy not associated with the other items present in the χ^2. This remaining energy is allowed to vary within an uncertainty of 25% for RE above 20 GeV and 40% for lower energy RE. These uncertainties were taken by extrapolating the jet transfer function uncertainties back to lower energies. By allowing the RE to vary the $E_{\mathrm{T}}^{\mathrm{miss}}$ can be indirectly rescaled as the jets and leptons are rescaled in the fits. This allows the neutrino p_z to be recalculated during the fit using the rescaled $E_{\mathrm{T}}^{\mathrm{miss}}$ value. By not constraining the hadronic decay to W mass in this χ^2 function both W and H^+ bosons present in $t\bar{t}$ decays can be reconstructed.

For each event the fitter considers all allowed combinations of the jets and the neutrino solutions, varying the measured values in the fit. Each combination is mimimsed and provides a final χ^2 value. The combination with the smallest χ^2 is taken as the most likely arrangement of jets to form the $t\bar{t}$ system. By placing a cut of $\chi^2 < 20$, poorly reconstructed and background events can be removed. The efficiency for $t\bar{t}$ events to pass this χ^2 cut if only the leading four jets are considered is 68%, which is a large loss of statistics. By allowing the fifth jet to be used in the manner described previously the efficiency of the cut is increased to 82%. The result of this improvement is seen in Figure 7.2. Figure 7.3 shows how the combined dijet mass distribution is improved

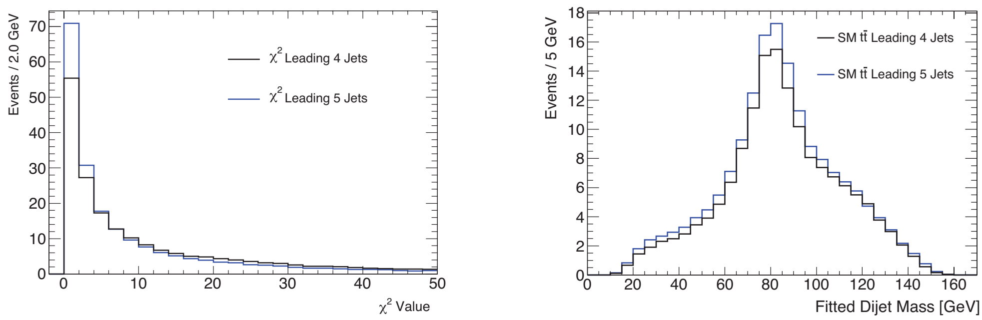

(a) (b)

Figure 7.2: Figure (a) Shows the comparison of the χ^2 distributions when using the four leading jets or the five leading jets. An improved efficiency of the $\chi^2 < 20$ cut of 82% is obtained using leading five jets. Figures (b) shows the improvement in the fitted dijet mass for SM $t\bar{t}$ when using five jets

after the kinematic fit and the requirement of $\chi^2 < 20$. The fitted dijet mass distribution is used as the final discriminating variable for the analysis. This distributions are used in the likelihood fit used to search for a H^+ signal or exclude it if no signal is seen. The procedure used for this likelihood fit is described in Chapter 9.

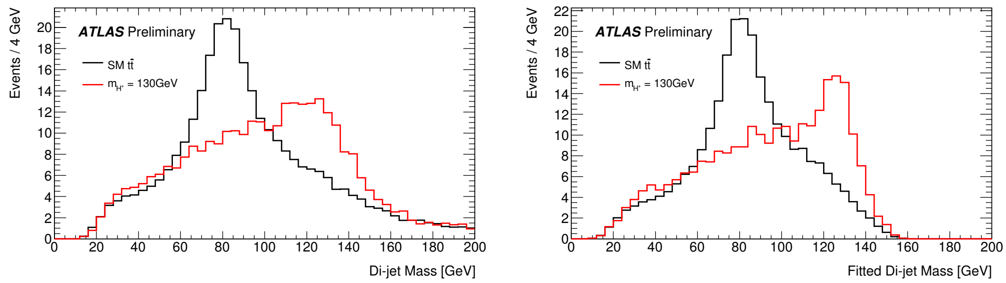

(a) (b)

Figure 7.3: The dijet mass distribution (both channels combined) for the reconstructed H^+ and W-bosons is shown in (a) before the fit. The dijet mass distribution (both channels combined) for H^+ and W after fitting is shown in (b). In the fitted distributions, an upper bound on the χ^2 was applied at 20.

7.5 Data Versus Monte Carlo Comparison

Tables 7.1 and 7.2 show the expected number of events for the signal and background processes and the observation in the data at different stages of the selection cuts. Both of the data driven QCD estimates are only defined for the pre-tagged and tagged samples. The scale factors outlined in Section 5.7 are applied to the events. Good agreement is seen between the expected number of SM background events and the data in both channels.

The expectations for three charged Higgs boson signals are also shown in the tables assuming $\mathcal{B}(t \to H^+b) = 0.1$. The signal acceptance for the single b-tag events is observed to decrease as the H^+ mass approaches the top mass. As the m_{H^+} increases the energy available to the b-jet on the hadronic side reduces and therefore the acceptance of the b-tag requirement is reduced.

The agreement between the number of expected events and the number observed in data seen gives an initial confidence in the modelling of the SM backgrounds. To have full confidence in the background estimation it is necessary to check that the kinematics

electron channel	no cut	trigger	1 electron	E_T^{miss}	4 jets	1 b-tag	χ^2
Data	-	5.41×10^6	318467	53896	399	156	130
SM $t\bar{t}$, not all hadronic	3163	1031	572	379	188	132	106
Single top, Wt-channel	514	100	55	34	8	5	3
Single top, t-channel	253	181	116	72	2	2	1
Single top, s-channel	17	12	7	5	0	0	0
$Wb\bar{b}$ + jets	74	72	48	25	3	2	1
$W \to e\nu$ + jets	191619	187001	127890	52183	168	12	8
$Z \to ee$ + jets	37462	28363	14338	149	14	1	1
$Z \to \tau\tau$ + jets	37250	2789	983	22	2	0	0
Dibosons	840	329	185	93	2	0	0
QCD(e)	-	-	-	-	22	9	6
Total SM background	-	-	-	-	410	164	127
$H^+ \to c\bar{s}$, 90 GeV	342	99	61	38	23	17	14
$H^+ \to c\bar{s}$, 110 GeV	342	99	61	38	24	17	14
$H^+ \to c\bar{s}$, 130 GeV	342	99	61	39	23	15	12

Table 7.1: Cut flow table for the charged Higgs boson signal with $\mathcal{B}(t \to bH^+) = 10\%$, and for the main SM backgrounds in the electron channel. The integrated luminosity is 35.3 pb^{-1}.

of the system are being correctly modelled. The expected distributions from Monte Carlo simulations are from this point onwards scaled to the expected values for 35.3 pb^{-1} of data.

7.5.1 Pre-tag Sample

To begin the comparison of the data to the backgrounds, the b-tag requirement is dropped. This produces the pre-tag sample. The level of agreement can be tested here with higher statistics. The main increase in events arises from the non-$t\bar{t}$ backgrounds, especially the W+jets process. The pre-tag sample is therefore a good test of

Process	Number of events after						
muon channel	no cut	trigger	1 muon	E_T^{miss}	4 jets	1 b-tag	χ^2
Data	-	2.59×10^6	274302	171839	654	246	193
SM $t\bar{t}$, not all hadronic	3163	1071	617	534	270	190	156
Single top, Wt-channel	514	101	56	48	10	6	5
Single top, t-channel	253	171	135	116	4	3	2
Single top, s-channel	17	12	7	4	0	0	0
$Wb\bar{b}$ + jets	104	81	62	51	5	3	2
$W \to \mu\nu$ + jets	262040	198190	171531	158124	303	21	14
$Z \to \mu\mu$ + jets	37193	28857	11582	6216	18	2	1
$Z \to \tau\tau$ + jets	37250	2981	1415	338	5	0	0
Dibosons	840	323	216	175	4	0	0
QCD(μ)	-	-	-	-	51	13	11
Total SM background	-	-	-	-	670	239	191
$H^+ \to c\bar{s}$, 90 GeV	342	109	65	55	34	24	20
$H^+ \to c\bar{s}$, 110 GeV	342	106	65	55	34	24	20
$H^+ \to c\bar{s}$, 130 GeV	342	104	64	54	32	21	18

Table 7.2: Cut flow table for the charged Higgs boson signal with $\mathcal{B}(t \to bH^+) = 10\%$, and for the main SM backgrounds in the muon channel. The integrated luminosity is 35.3 pb^{-1}.

the modelling of the non-$t\bar{t}$ backgrounds.

Figure 7.4 shows the pre-tag comparisons between data and MC for the kinematics of the leptons, $E_{\mathrm{T}}^{\mathrm{miss}}$ and a selection of the jets. The lepton kinematic shapes shown are expected to be unaffected by the presence of a signal and therefore provide a good control distribution in which to test the data and MC agreement. Good agreement is seen in both the electron and muon channels for the lepton p_T, η and ϕ. The jet p_Ts also show good agreement. The jet p_T distributions would be altered by the presence of a signal and so agreement here is not a conclusive test of background modelling. Figure 7.5 shows comparisons of the data and MC for variables derived from the fitter output. Good agreement is again seen here for all plots. This shows that the fitter treats the data and MC consitently, even when the majority of events used are non-$t\bar{t}$ events. A good point to note is the shape seen for the W+jets component in the fitted dijet distribution. This is the shape of the combinatorial background, flat and smooth with no discernible peak.

7.5.2 Full Selection Sample

By re-introducing the b-tagging criteria the MC modelling of the final system can be explored. Figure 7.6 shows the data and MC agreement seen in the lepton kinematic variables after the kinematic fit. Good agreement is seen here between the data and MC, showing good modelling of both electrons and muons within the detector. Figure 7.7 shows the data and MC agreement seen in the $E_{\mathrm{T}}^{\mathrm{miss}}$ and also the complete neutrino kinematics as reconstructed from the kinematic fit. The measured $E_{\mathrm{T}}^{\mathrm{miss}}$ distributions agrees well between data and MC, with some relative minor statistical fluctuations, thus showing the good overall modelling of the detector in MC. The agreement in the fully reconstructed neutrino kinematics is fairly remarkable, considering the longitudinal neutrino momentum was an unknown in the system. It has however been recovered with good agreement between data and MC.

The data versus MC agreement for the main kinematic variables of the b-tagged jets and the jets assumed to originate from the hadronic W decay are shown in Figures 7.8 and 7.9 respectively. Good agreement is seen for all jet p_T distributions both before and after the kinematic fit has varied the jets. As expected all jets follow a uniform distribution in ϕ and peak towards the central region in η as would be expected for high p_T events. These distributions are sensitive to the presence of a signal which would alter the dijet distributions directly and indirectly affect the hadronic b-jet distributions by reducing the kinematic phase space available to the b-quark. This would manifest itself as a difference between the hadronic and leptonic b-jet distributions; no obvious discrepancies of this nature can be seen in the data.

With the overall excellent agreement of the kinematic distributions, before and after the b-tag requirement, especially the neutrino calculated variables, it is safe to

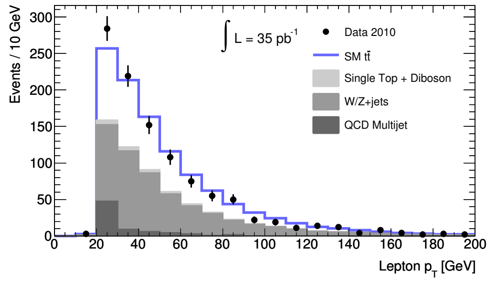

(a)

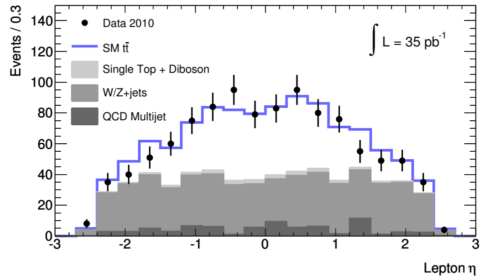

(b)

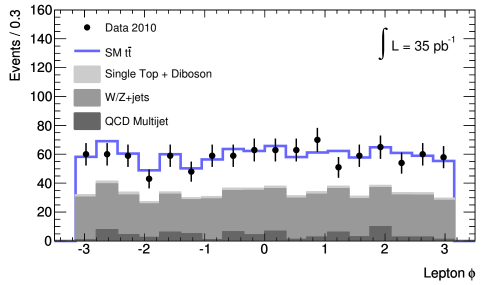

(c)

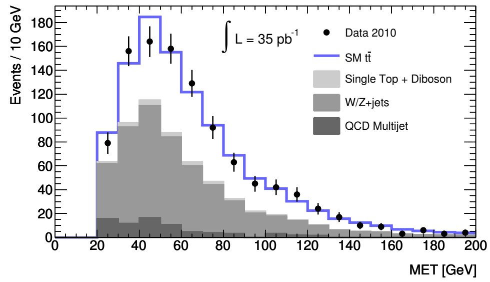

(d)

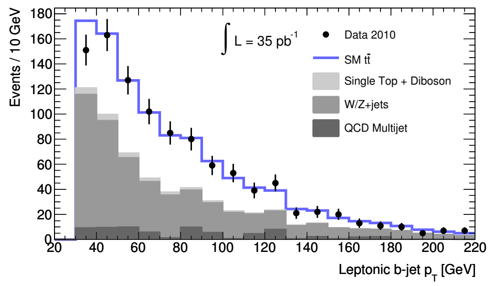

(e)

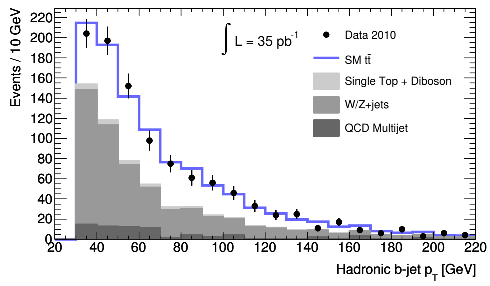

(f)

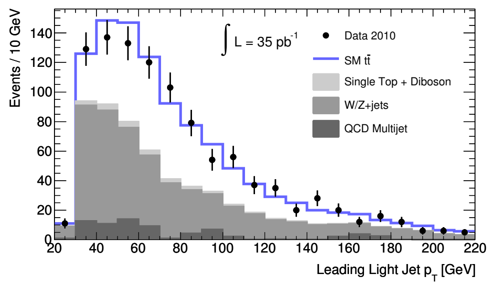

(g)

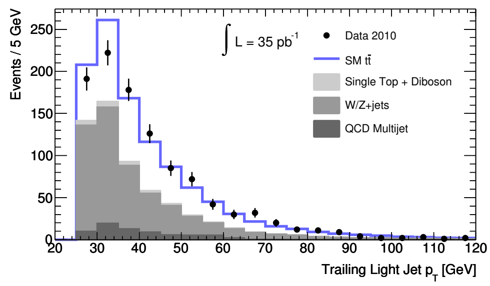

(h)

Figure 7.4: Comparison of the data and predicted backgrounds with no b-tag requirements for (a, b, c) the lepton p_T, η and ϕ, (d) the $E_{\mathrm{T}}^{\mathrm{miss}}$, (e, f, g, h) the leptonic and hadronic b-jets p_T and the dijets p_T. These plots contain the muon and electron channels combined.

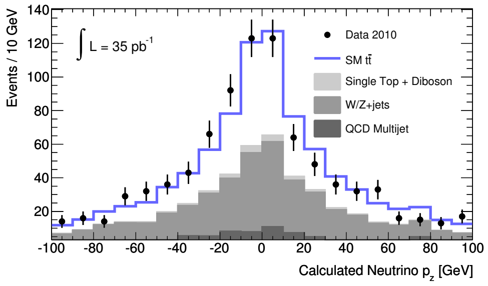

(a)

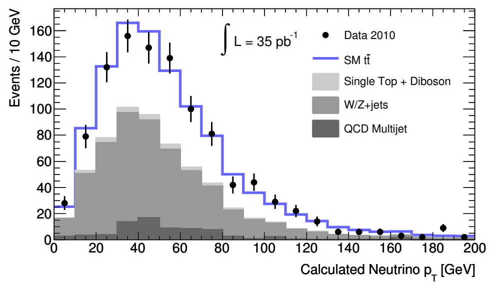

(b)

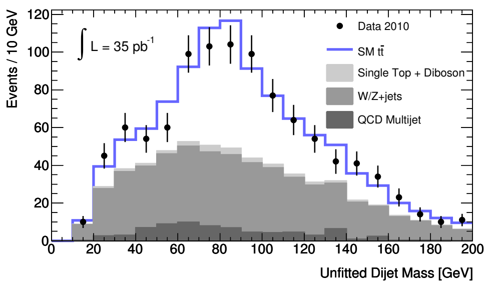

(c)

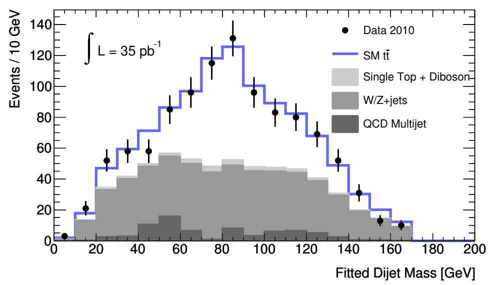

(d)

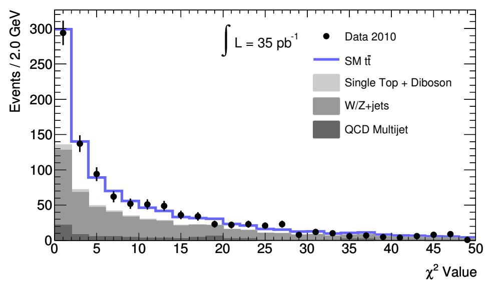

(e)

Figure 7.5: Comparison of the data and predicted backgrounds with no b-tag requirements for variables extracted from the fitter. Figures (a, b) show the neutrino p_z and p_T respectively, (c, d) show the unfitted and fitted dijet mass distributions and (e) shows the χ^2 distribution. These plots contain the muon and electron channels combined.

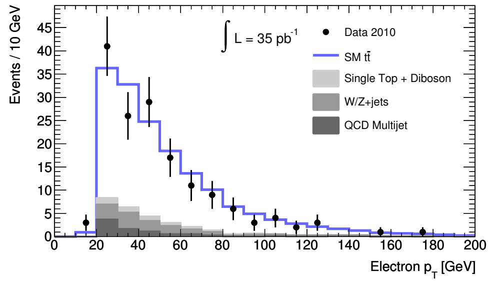

(a)

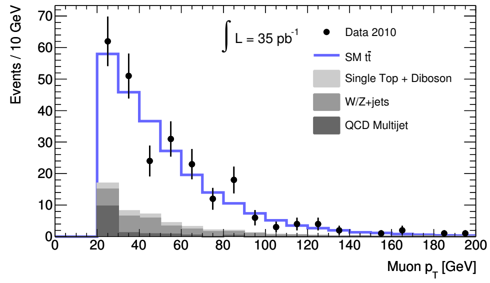

(b)

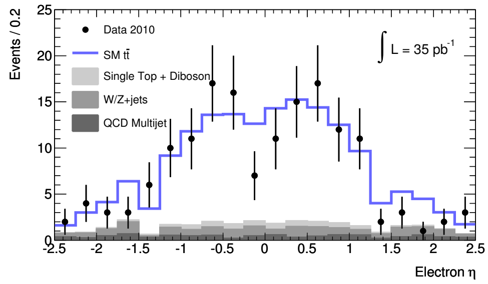

(c)

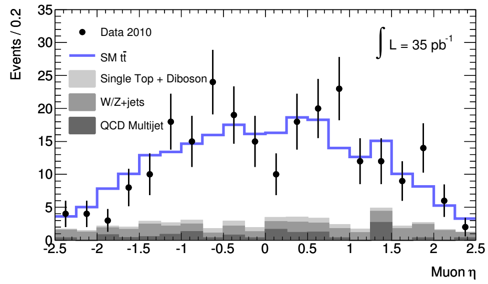

(d)

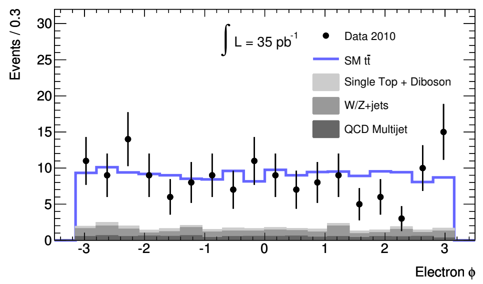

(e)

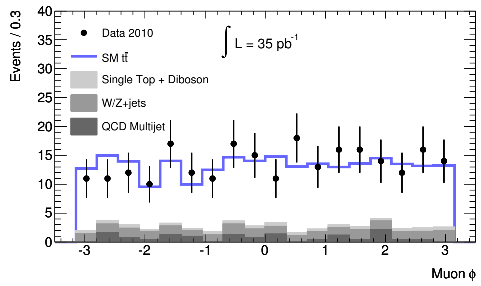

(f)

Figure 7.6: Comparison of the data and predicted backgrounds for lepton p_T, η and ϕ: electron sample (a,c,e), muon sample (b,d,f). Plots shown here show the agreement after the fitter and the $\chi^2 < 20$ cut have been applied

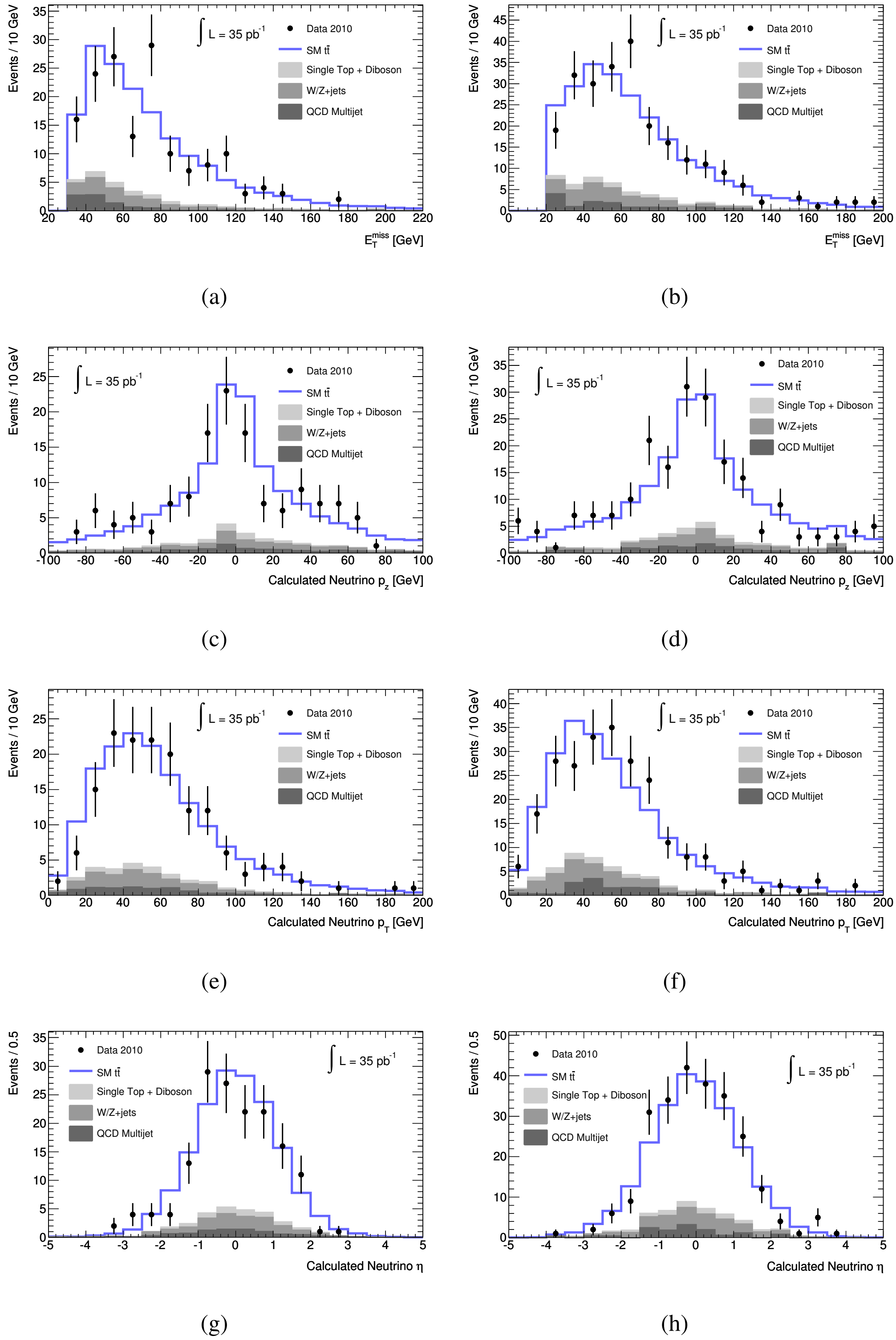

Figure 7.7: Comparison of the data and predicted backgrounds for the $E_{\mathrm{T}}^{\mathrm{miss}}$ and the calculated neutrino values p_z, p_T and η: electron sample (a,c,e,g), muon sample (b,d,f,h). Plots shown here show the agreement after the fitter and the $\chi^2 < 20$ cut have been applied

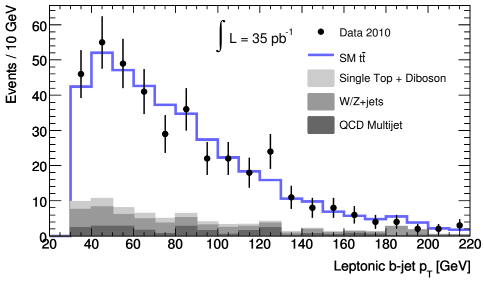

(a)

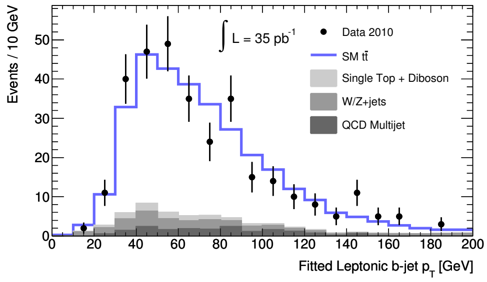

(b)

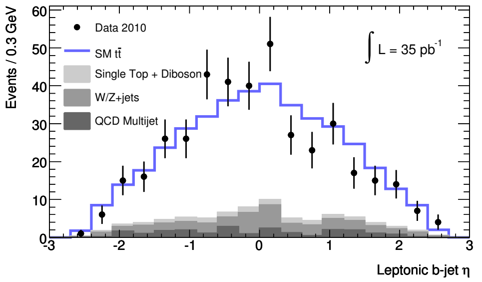

(c)

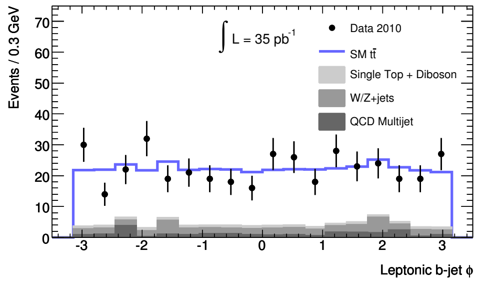

(d)

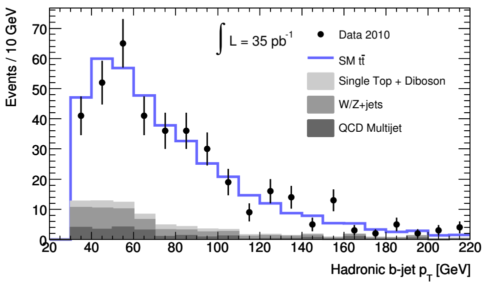

(e)

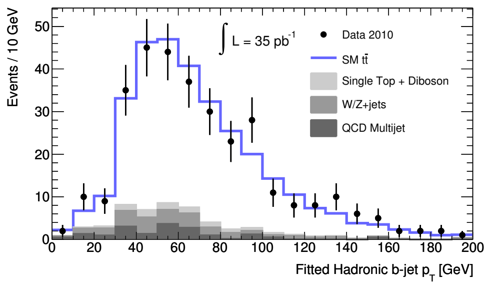

(f)

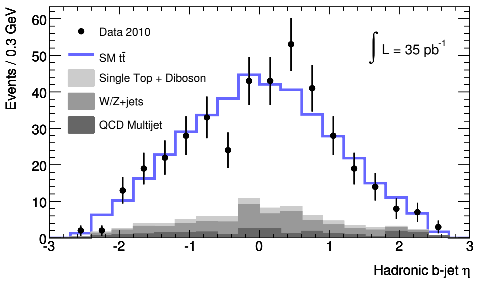

(g)

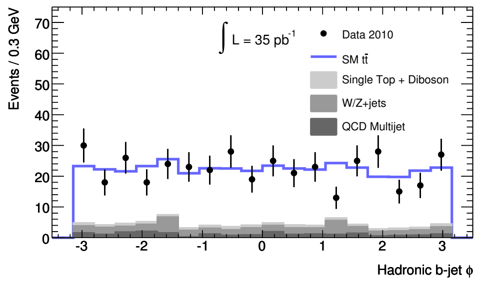

(h)

Figure 7.8: Comparison of the data and predicted backgrounds for the leptonic and hadronic b-jets p_T, η and ϕ. Plots shown here show the agreement after the fitter and the $\chi^2 < 20$ cut have been applied, except in plots (a,e) which show the p_T distributions prior to the fit.

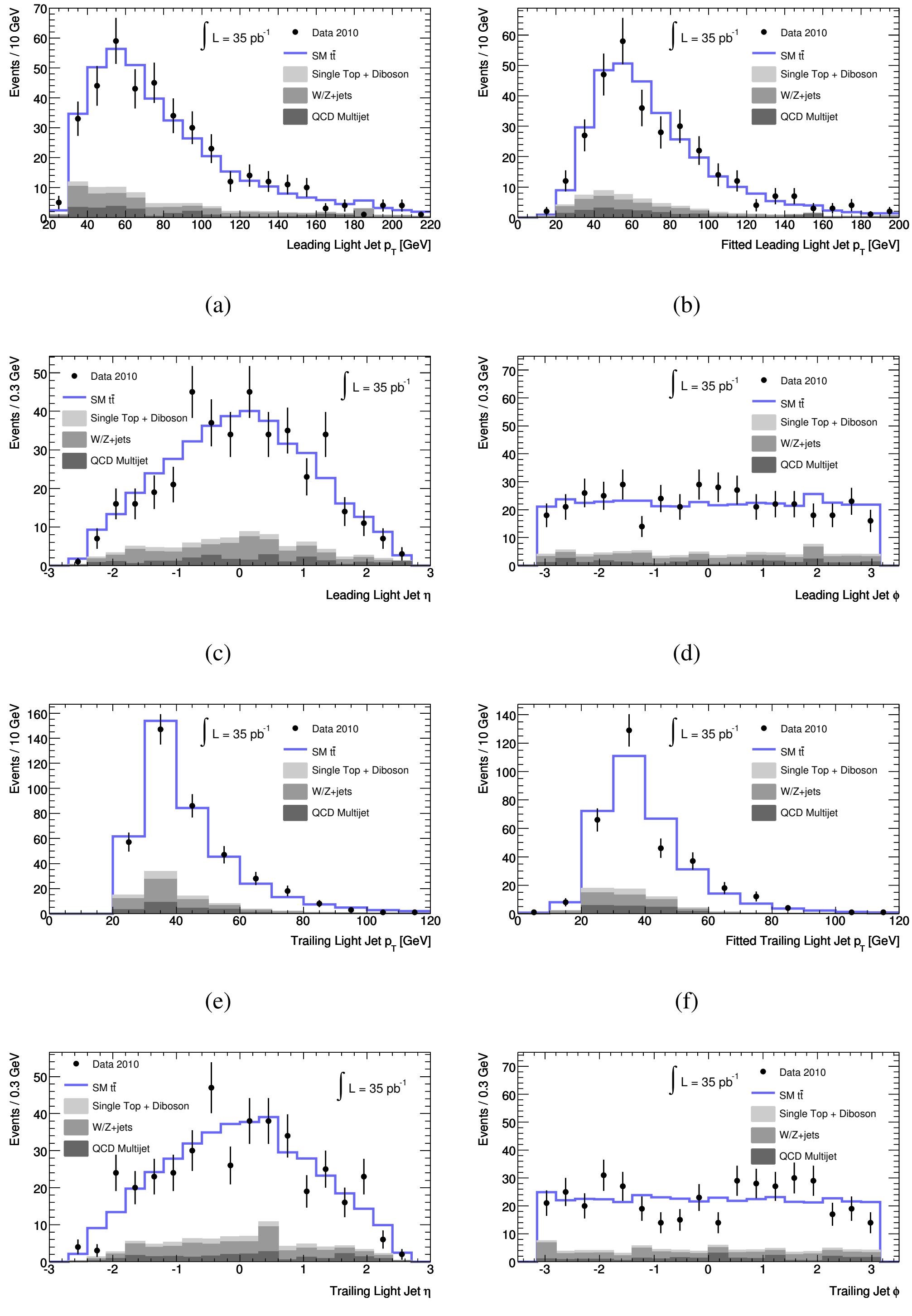

(a) (b)

(c) (d)

(e) (f)

(g) (h)

Figure 7.9: Comparison of the data and predicted backgrounds for each jet from the light-quark dijets: p_T, η and ϕ. Plots shown here show the agreement after the fitter and the $\chi^2 < 20$ cut have been applied, except in plots (a,e) which show the p_T distribution prior to the fit.

assume that the fitter is behaving as expected. To check the behaviour, Figure 7.10 shows the χ^2 distribution for both channels. The consistency here that the data and MC both respond to the fitter in the same fashion. As can be seen here the $\chi^2 < 20$ selection removes mainly events forming the background. For example, events where the wrong four jets have been passed to the fitter will likely fail this requirement as the jet rescaling required to form a top mass will cause a large χ^2 contribution. The dijet mass distribtuions both before and after the fit are also shown in Figure 7.10. Both show good data versus MC consistency and give distributions which peak at the W boson mass. The tail seen to high masses is mainly the result of the combinatorial backgrounds, after the fit the tail is reduced and the peak becomes more pronounced.

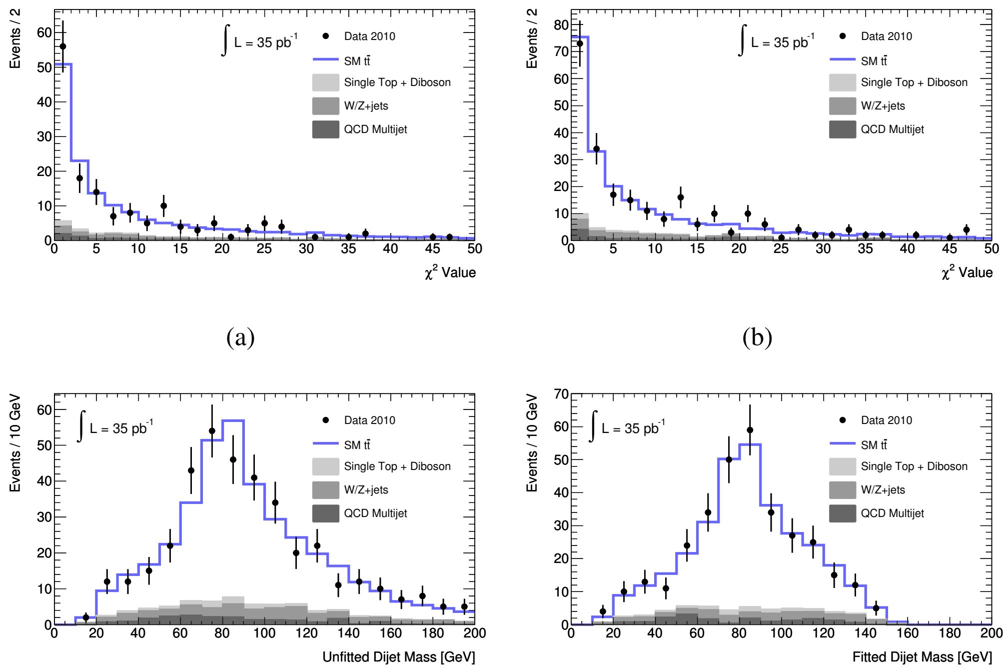

(a) (b)

(c) (d)

Figure 7.10: Comparison of the χ^2 distribution in data and the predicted backgrounds for (a) the electron channel and (b) the muon channel. The dijet mass distribution before the jet rescaling in the fit (using the jet combination from the fit) is shown in (c) and the distribution after the fit and the χ^2 cut is shown in (d).

Chapter 8

Systematic Uncertainties

This analysis is affected by systematic effects which can perturb the dijet mass distribution and thus alter the conclusion of the analysis. The systematic uncertainties can alter the dijet distribution in two main ways, firstly normalisation effects which change the acceptance of events through the selection requirements. These effects tend to modify both signal and background in the same fashion. Secondly various systematic uncertainties can perturb the shape of the dijet mass distribution. As the analysis is reliant upon the discriminating power of the shape of the distribution these are important sources of systematic uncertainty. They can potentially fake a signal peak by shifting events from the W peak to a higher mass. In this chapter the main sources of systematic uncertainty will be outlined showing both their effects on the normalisation and where appropriate the shape changes they cause.

8.1 Sources of Systematic Uncertainty

This section will split the sources of systematic uncertainty into those which contain a shape component and those which affect only the normalisation of the dijet mass distribution. For each systematic uncertainty the $\pm 1\sigma$ systematic effects will be shown as they are used in the analysis, either as an altered dijet mass distribution or an overall normalisation. The altered dijet distributions were produced by re-running the entire event selection and kinematic fit with the systematic uncertainty variation under consideration. This produces a dijet mass distribution and acceptance change relative to the nominal selection which can then be considered in the analysis. The definitions of each systematic uncertainty can be found in Table 8.1 and the overall effect on the acceptance of events can be seen in Table 8.2.

Systematic uncertainty	Definition $\pm 1\sigma$
Jet energy scale	$\pm$ 4%$*$ ($\|\eta\| < 3.2$), $\pm$ 10%$*$ ($\|\eta\| > 3.2$)
b-jet energy scale	$\pm$ 2.5%
Jet energy resolution	$\pm$ 5%$*$ ($\|\eta\| < 0.8$), $\pm$ 10%$*$ ($\|\eta\| > 0.8$)
b-tagging efficiency	$\pm$8%$*$
MC generator	MC@NLO vs POWHEG
Parton shower	HERWIG vs PYTHIA
ISR/FSR	ACERMC: up vs down
Additional Interactions	Vertex re-weighting off vs on
Luminosity	$\pm$3.4%
Electron reconstruction & identification	$\pm$3.9%
Muon reconstruction & identification	$\pm$0.4%
Electron trigger	$\pm$0.2%
Muon trigger	$\pm$0.8%
$t\bar{t}$ cross section	+7%, −9%
Non-$t\bar{t}$ backgrounds	background normalisation, $\pm$32%

Table 8.1: Definitions of the main sources of systematic uncertainty. The sources marked with a $*$ are dependent upon kinematic variables defined in bins of p_T and η.

8.2 Shape Perturbing Systematics

8.2.1 Jet Energy Scale Uncertainty

The jet energy scale (JES) uncertainty is largest systematic uncertainty for this analysis. It directly affects both the normalisation and shape of the dijet mass distribution. As

Systematic Uncertainty Source	Normalisation Effect
Jet energy scale	$+11, -13\%$ (SM $t\bar{t}$)
	$+9, -12\%$ (signal)
Jet energy resolution	$\pm 1\%$
b-tagging efficiency	$+4, -9\%$
MC generator	$\pm 4\%$
Parton shower	$\pm 3\%$
ISR/FSR	$\pm 1\%$
Additional Interactions	$\pm 2\%$
Luminosity	$\pm 3.4\%$
Electron reconstruction	$\pm 1.6\%$
Muon reconstruction	$\pm 0.2\%$
Electron trigger	$\pm 0.2\%$
Muon trigger	$\pm 0.5\%$
$t\bar{t}$ cross section	$+7, -9\%$

Table 8.2: Effect of the systematic uncertainties on the expected number of $t\bar{t}$ background and signal ($m_{H^+} = 110$ GeV) events. Where only one uncertainty is given, the effect is the same for both the signal and $t\bar{t}$ background.

mentioned in Chapter 5, the calorimeter response to jets has to be corrected to return to the actual energy deposited by the particle level jets. The uncertainty on the p_T of the jets after the JES is applied is taken into account by the JES uncertainty. The main contributions to the uncertainty are determined from measurements made in inclusive dijet events. The variation, $\Delta_{JES}^{variation}$, with respect to the nominal JES response, R, is calculated for each source of systematic uncertainty:

$$\Delta_{JES}^{variation} = \left| 1 - \frac{R_{variation}}{R_{nominal}} \right|. \tag{8.1}$$

Each source is added in quadrature to gain the full JES systematic uncertainty. Various detector related sources of uncertainty are modelled using MC and data driven calibration techniques. Sources of uncertainty include:

1. The JES calibration method uncertainties.

   The EM-JES calibration method has some uncertainty associated with the closure of the method, i.e. does the correction return the jet to the correct p_T. The effect can be seen by applying the calibration derived to a sample of jets and observing that the response is not uniformly one as you would expect after a calibration. This is due to the calibration being an average compensatory factor which may not be applicable to all jets. An uncertainty due to non-closure is taken to be the deviation of the response from unity between E and p_T.

2. The calorimeter response uncertainties.

   Single particle response measurement from early ATLAS data and pion test beams are used to estimate the size of the calorimeter energy uncertainties. Miss-modelling of the calorimeter noise can lead to biases. An uncertainty is estimated by using the noise measured in data.

3. The detector simulation uncertainties.

   The detector model used in data could be incorrect. In-situ measurements are once again employed to firstly improve the material description of the model and secondly apply an uncertainty by varying the material in the GEANT model.

4. The MC generator uncertainties.

   The MC used to derive the JES does not necessarily model the fragmentation of jets or the underlying event perfectly. An uncertainty is prescribed by varying the generator used for event generation, showering and underlying event. Different parton distribution functions are also compared to consider their effects.

5. The pile-up uncertainties.

   An uncertainty due to multiple proton interactions is applied to account for possible variations due to the pile-up. Pile-up can add energy to jets. The size of this uncertainty varies with the number of additional vertices.

6. The $t\bar{t}$ sample jet flavour uncertainties.

The final two uncertainties are specific to the multi-jet environment of the $t\bar{t}$ system. The other JES uncertainties are derived from an inclusive QCD dijet sample providing high statistics and a clean environment. The $t\bar{t}$ system contains a large number of jets, therefore the assumptions made for the generic JES do not necessarily hold anymore. Light quark and gluon jets have different responses in the calorimeter with light quark initiated jets tending to have a narrower shower shape than gluon jets. As the main JES was derived in the dijet system this calibration assumes a certain ratio of light quark to gluon initiated jets. The $t\bar{t}$ system by definition will not have the same ratios of light quark to gluon jets. An uncertainty is therefore applied to account for differences between the dijet and $t\bar{t}$ systems. The relative uncertainty due to light quark and gluon initiated jets are defined relative to the dijet sample as functions of p_T and η. These are then combined with the uncertainty on the gluon fraction in the $t\bar{t}$ sample relative to the dijet sample to provide the full flavour uncertainty,

$$\Delta_{t\bar{t}} = \alpha_c \left(\frac{R_{\text{light/gluon}}}{R_{\text{dijet}}} - \frac{R_{t\bar{t}}}{R_{\text{dijet}}} \right) / \left(\frac{R_{t\bar{t}}}{R_{\text{dijet}}} \right), \tag{8.2}$$

where R is the response of jets in each sample and α_c is the uncertainty on the fraction of gluon jets in the $t\bar{t}$ sample.

7. <u>The close-by jet uncertainties.</u>

   In the dijet system jets tend to be fairly isolated from other jets (ignoring pile-up effects which are dealt with separately) leading to a low level of energy leakage from one to another. In the semi-leptonic $t\bar{t}$ system at least four jets are expected in the final state. Therefore there is a larger chance of the jets' edges overlapping and assigning energy to the incorrect jet. To account for this an additional uncertainty of 5% is applied in quadrature to jets with a second jet within $\Delta R < 0.6$.

The full JES uncertainty takes the full set of uncertainties and combines them in quadrature. It is defined as a function of both p_T and η. When using the $\pm\sigma$ JES uncertainties the altered p_T's of the jets are propagated into the calculation of E_T^{miss}. The effect of applying the full JES uncertainty can be seen in Figure 8.1. The first effect of the JES uncertainty is to raise and lower the efficiency of events passing the selection

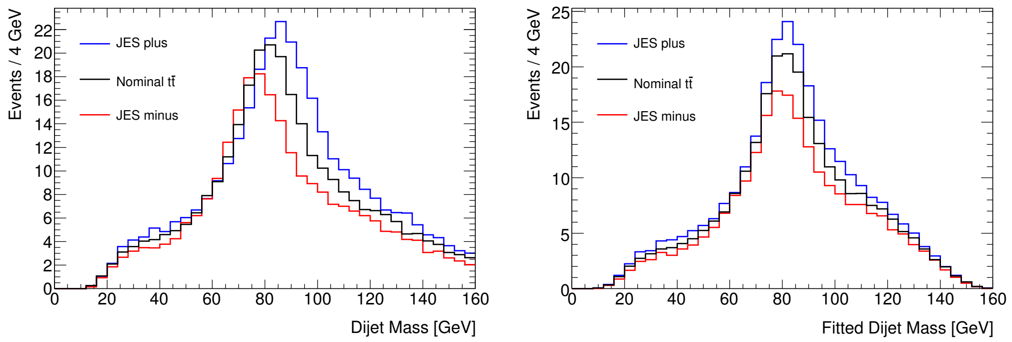

(a) (b)

Figure 8.1: (a) The dijet mass distribution for the reconstructed W bosons in the SM $t\bar{t}$ sample with JES $\pm\sigma$. (b) The distributions after the fit and χ^2 cut.

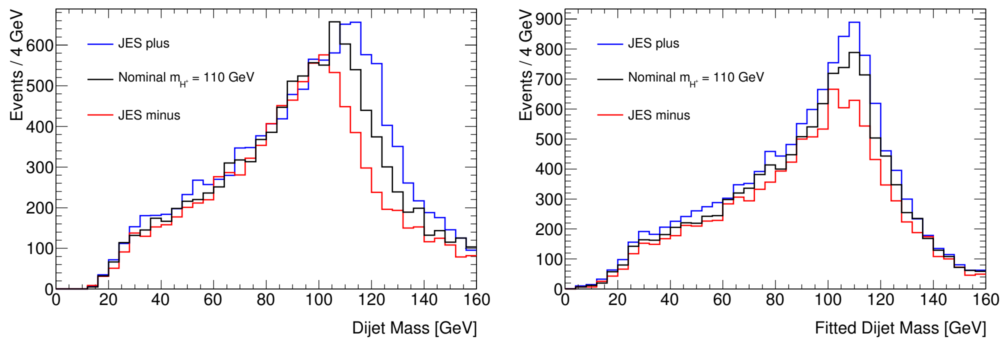

(a) (b)

Figure 8.2: (a) The dijet mass distribution for the reconstructed H^+ bosons in the 110 GeV sample with JES $\pm\sigma$. (b) The distributions after the fit and χ^2 cut.

cuts, because the change in jet p_T alters the acceptance of the four jet requirement. The second effect is a shift in the peak position of the dijet mass distribution. This effect is more prominent before the χ^2 fitter is applied and is partially alleviated by the varying of each jet's p_T in the χ^2 fitter which reconstructs the W mass peak more efficiently. A similar effect is seen in the signal samples, shown in Figure 8.2, with the shape effect of the JES again being reduced after the χ^2 fitter is used. The overall normalisation effect of the JES uncertainty can be seen in Table 8.2.

8.2.2 b-jet Energy Scale Uncertainty

The JES uncertainty described in the previous section made the assumption that jets were either quark or gluon initiated. It made no separate considerations for b-quark initiated jets. Heavy flavour jets show a different calorimeter response to light jets and gluons. The fragmentation of b-quarks is less well understood compared to light quark jets due to the inclusion of heavier mesons such as B hadrons. These heavier hadrons can regularly decay leptonically leading to the emission of a neutrino which escapes the detector undetected, thus leading to a different response to light jets. Studies using b-tagged jets show that the energy scales agree across the full p_T range within 2.5%. An uncertainty of 2.5% on the jet p_T was placed on b-tagged jets. This has a minor effect on the peak of the dijet mass distribution and a negligible effect on the over all acceptance, as shown in Figure 8.3.

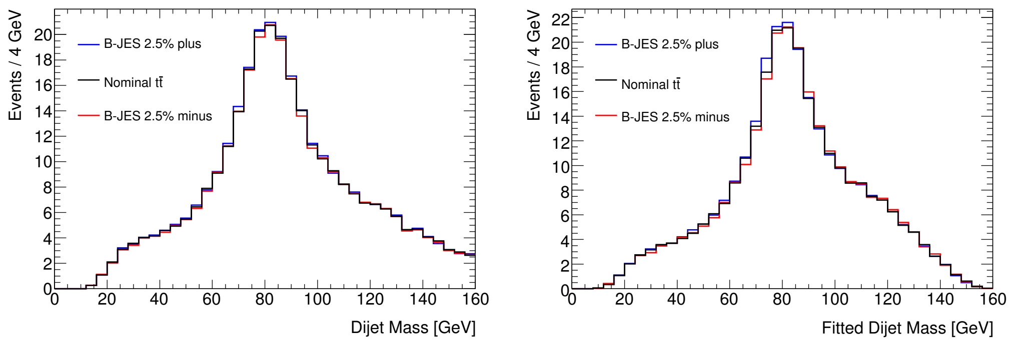

(a) (b)

Figure 8.3: (a) The dijet mass distribution for the reconstructed W bosons with b-JES $\pm\sigma$. (b) The distributions after the fit and χ^2 cut .

8.2.3 Jet Energy Resolution

The resolution of jets recorded by ATLAS directly affects the width of the dijet mass peak observed by broadening the constituent jets. The jet energy resolution (JER) observed in data therefore needs to be correctly modelled in the MC. The systematic uncertainty on the JER modelling is taken by applying a gaussian smearing of each jet's energy in MC, with the size of the smearing depending on its η position in the detector. Central jets are better understood than jets in the end-cap region and therefore the JER uncertainty increases as $|\eta|$ increases. This procedure accounts for the case of the data having a worse resolution than the MC. The resolution measured in data is within 10% of the MC resolution for all jets $30 < p_T < 500$ GeV and $|\eta| < 2.8$ [73]. The reverse situation is accounted for by symmeterizing the JER uncertainty about the nominal sample. The effect of this systematic uncertainty is small but produces a slightly broader W mass peak as shown in Figure 8.4. As shown for the case of the JES uncertainty the χ^2 fitter once again reduces the size of this systematic uncertainty.

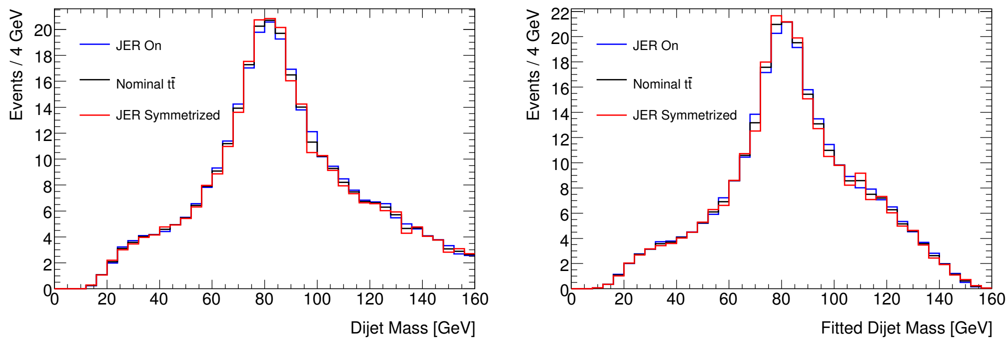

(a) (b)

Figure 8.4: (a) The dijet mass distribution for the reconstructed W bosons in the SM $t\bar{t}$ sample with JER $\pm\sigma$. (b) The distributions after the fit and χ^2 cut . The negative sigma systematic uncertainty is taken as the symmeterized distribution of the JER On distribution.

8.2.4 B-tagging Efficiency

The scale factor applied to match the rate of tagging b quarks in data to the rate in MC has been calculated with a known uncertainty. The nominal scale factor, f_{tag}, was applied to the data by dropping the tagging information from jets proportional to $1 - f_{tag}$. The uncertainty was applied by varying the rate at which b-tags were dropped in MC by the $\pm 1\sigma$ uncertainty. The effect of the uncertainty is shown in Figure 8.5.

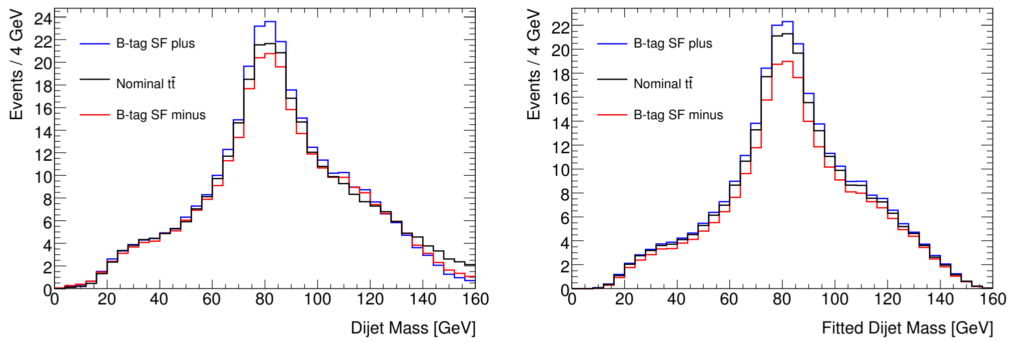

(a) (b)

Figure 8.5: (a) The dijet mass distribution for the reconstructed W bosons in the SM $t\bar{t}$ sample with the b-tagging efficiency scale factor $\pm\sigma$. (b) The distributions after the fit and χ^2 cut.

8.2.5 Initial and Final State Radiation

In the $t\bar{t}$ system gluons can be radiated from the incoming partons (initial state radiation, ISR) or from the final state quarks (final state radiation, FSR). ISR radiation can produce a high p_T jet which could then be considered as one of the jets forming the $t\bar{t}$ system. If a FSR gluon is emitted at a wide angle outside the jet this reduces the p_T of the original parton and forms a second jet. The loss of energy can cause the jet to be no longer be considered in the fit. In both cases the incorrect jets would now be considered in the fit. This would cause the event to be mis-reconstructed, adding to the combinatorial background of the dijet mass distribution. Samples produced by the AcerMC MC generator have been used to vary the amount of ISR/FSR present in the $t\bar{t}$ sample and observe the effect on the dijet mass distribution. The size of the effect is taken relative to the nominal AcerMC sample and then transformed to the nominal MC@NLO sample to give the final systematic uncertainty templates. This procedure avoids introducing addition systematic uncertainties due to the differences between a leading order generator such as AcerMC and the next-to-leading order generator MC@NLO. As shown in Figure 8.6, the effect of variations in the amount of ISR/FSR radiation follows a similar shape change to the effect of JES variation. As FSR increases or decreases it removes or adds more energy from the dijet system and thus alters the efficiency of the cuts and

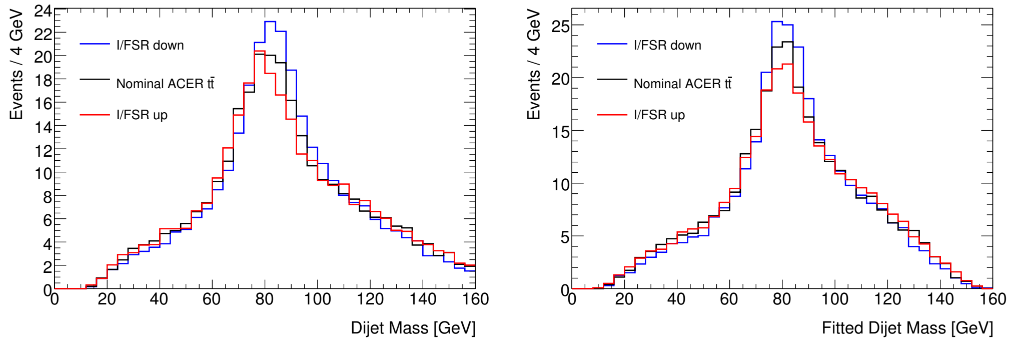

(a) (b)

Figure 8.6: (a) The dijet mass distribution for the reconstructed W bosons with ISR/FSR up/down. (b) The distributions after the kinematic fit.

shifts the peak to lower or higher masses. Increasing and decreasing the ISR varies the size of the combinatorial background but has a significantly smaller effect on shape of the distribution. As no samples with variations of the ISR or FSR are available for the signal sample the relative size of the acceptance changea in the SM samples was taken as a normalisation systematic uncertainty on the signal sample.

8.2.6 MC Generator and Showering Choice

MC generators attempt to model the physics processes being studied in a series of steps. They describe the evolution of the incoming partons into the hard-scatter process then through the showering and fragmentation of the final state partons into stable particles. The choice of program or algorithm at each step can be ascribed an uncertainty by observing the difference between the default choice and an alternate generator. The generator POWHEG was chosen to ascribe an uncertainty to using a different MC program to describe the central hard-scatter process. The POWHEG $t\bar{t}$ events were showered using HERWIG along with JIMMY for the multiple parton interactions as in the default MC@NLO sample. The difference was taken with respect to the nominal sample and the effect can be seen in Figure 8.7. The difference between the two programs is not manifested as an obvious peak shift or broadening and a priori such clear cut differences would not be expected.

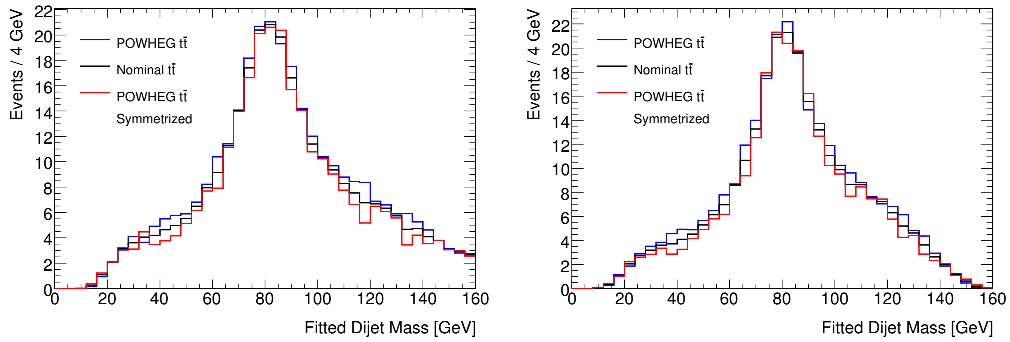

(a) (b)

Figure 8.7: (a) The dijet mass distribution for the reconstructed W bosons in the SM $t\bar{t}$ sample with the generator choice systematic uncertainty $\pm\sigma$. (b) The distributions after the fit and χ^2 cut. The negative systematic uncertainty is taken as the symmeterized version of the distribution obtained by swapping generator to Powheg.

Another possible source of systematic uncertainty arises from the choice of MC generator used to shower the central process. A systematic sample was generated using Powheg and showered by Pythia. The default choice of showering algorithm Herwig is a angular ordered showering algorithm. It first produces emissions with the widest angle to the emitting parton with subsequent emissions becoming more and more collinear. The showering algorithm in Pythia however is instead p_T ordered. It begins by producing the highest p_T emissions in the shower, decreasing until it reaches the hadronisation scale. The Pythia showered Powheg sample was compared to the Powheg+Herwig sample and the relative change between the two taken as the difference in showering models. This difference was then applied to the default MC to produce the systematic uncertainty templates. The effect of this can be seen in Figure 8.8.

8.2.7 Vertex Re-weighting

Pileup occurs when multiple pp interactions from the same, in-time pileup, or surrounding bunch crossings, out-of-time pileup, are read out simultaneously by the detector. The modelling of in and out-of-time pileup in the MC was found to be imper-

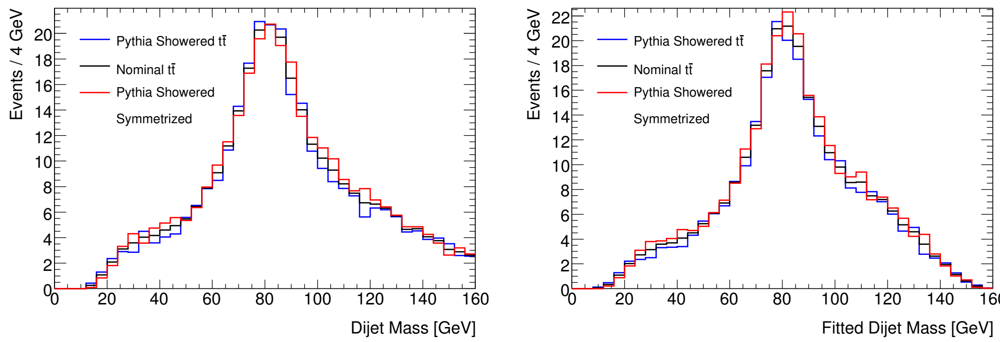

(a) (b)

Figure 8.8: (a) The dijet mass distribution for the reconstructed W bosons in the SM $t\bar{t}$ sample with the shower generator choice systematic uncertainty $\pm\sigma$. (b) The distributions after the fit and χ^2 cut. The negative systematic uncertainty is taken as the symmeterized version of the distribution obtained by swapping generator to PYTHIA.

fect. The distribution of primary vertices in MC did not match the full data run for the year. A scale factor was therefore applied according to the number of vertices in the MC to correct this mismodelling. The effect of re-weighting on the number of vertices distribution can be seen in Figure 8.9. It shows an improved agreement between data and MC after the re-weighting has been applied. The dijet mass shape dependence of applying the vertex re-weighting is small and can be seen in Figure 8.10.

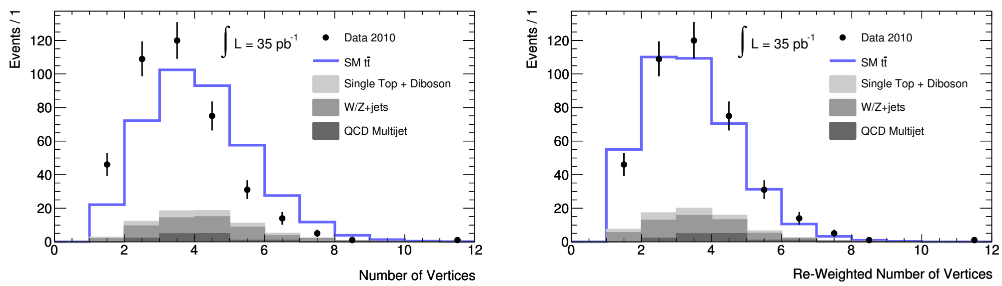

(a) (b)

Figure 8.9: The number of vertices (a) using only the default pileup modelling in the MC, and (b) the result of applying vertex re-weighting to the events. As the QCD multijet contribution is derived from data is it unaffected by by the vertex re-weighting

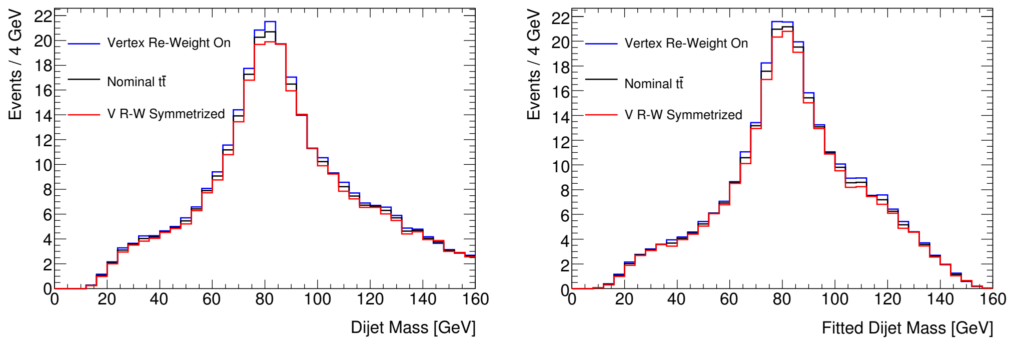

(a) (b)

Figure 8.10: (a) The dijet mass distribution of the reconstructed W bosons in the SM $t\bar{t}$ sample with vertex re-weighting $\pm\sigma$. (b) The distributions after the fit and χ^2 cut. The negative systematic uncertainty is taken as the symmeterized distribution of the vertex re-weighting on distribution.

8.3 Normalisation Effects

The following uncertainties do not alter the shape of the dijet mass distribution, instead only causing a change in the number of expected events. They are therefore included in the fit as a normalisation factor to the appropriate samples.

8.3.1 Theoretical $t\bar{t}$ Cross-Section

The SM $t\bar{t}$ cross section assumed in this analysis, 164.6pb [28], was taken from theory calculations. This systematic effect is the dominant source of uncertainty on the normalisation of the dijet mass peak. The uncertainty on this cross-section was taken to be $^{+7\%}_{-9\%}$ [28], which includes both the scale and PDF uncertainties. This systematic effect was applied as a normalisation uncertainty to both the signal and background SM $t\bar{t}$ decays.

8.3.2 Top Mass Variation

The calculation of the SM $t\bar{t}$ cross section also depends upon the $m_{t\bar{t}}$ that is assumed. The samples used for signal, background and systematic effects were all produced at a top mass of 172.5 GeV. If a charged Higgs boson were present in semi-leptonic $t\bar{t}$ decays this could bias previous mass measurements. To account for this effect the uncertainty on the top mass was taken from the latest Tevatron dilepton measurements [74, 75] to be $\Delta m_t = 2.5$ GeV. The shift in the SM $t\bar{t}$ cross section due to the uncertainty on m_t was found to be ±7% [28]. It is taken as uncorrelated with the theoretical uncertainty.

8.3.3 Lepton Scale Factors

The lepton reconstruction and trigger efficiency scale factors have small uncertainties associated with them. These uncertainties have a minor effect (of the order 0.2%) on the acceptance of the selection cuts, shown in Table 8.2. No shape dependence was seen for any of these uncertainties and therefore they were combined in quadrature with the normalization uncertainty on the theoretical cross-section.

8.3.4 Normalisation of the Non-$t\bar{t}$ Backgrounds

The largest contribution to the non-$t\bar{t}$ backgrounds is the W+jets background. This background is well modelled by the MC as demonstrated by the agreement in the pre-tag channel shown in Chapter 6. An uncertainty on the normalisation of the W+jets background is determined by performing a fit to the data of the lepton η distribution in the W+jets sample before b-tagging is applied. This variable is selected as it is expected to be consistent between signal and background samples. Therefore the presence of a signal in data would not introduce a bias to the fit. In this fit the W+jets and $t\bar{t}$ contributions were allowed to float, holding the other non-$t\bar{t}$ contributions constant. From this fit a W+jets normalisation uncertainty of ±26% was extracted. An additional uncertainty was added to account for the b-tag mis-tag rate. This covers the probability of a light jet in a W+jets event to be incorrectly b-tagged and therefore pass the cuts. Adding this leads to a 22% change in acceptance for the W+jets sample. These uncertainties were combined in quadrature producing a total uncertainty of 34%. Uncertainty on the QCD multi-jet backgrounds are conservatively estimated to be 30 and 50% citeATLAS-CONF-2011-023 for the muon and electron channel. The remaining single top and diboson samples are assigned 10 and 5% citeATLAS-CONF-2011-023 uncertainties respectively. These uncertainties were combined in quadrature and taken as an overall uncertainty on the non-$t\bar{t}$ background of 17.7%. The non-$t\bar{t}$ backgrounds form a combinatorial background to the fit as the fitter tries to force the reconstruction of a $t\bar{t}$ event. The uncertainty was calculated by combining in quadrature the various sources of uncertainty on the modelling of the channels contribution to the non-$t\bar{t}$ background.

8.3.5 Luminosity Uncertainty

The luminosity used in this analysis of 35.3pb^{-1} has been calculated by various techniques described in Section 3.1. The LHC and ATLAS have employed various methods to constrain the luminosity uncertainty. Full Van de Meer scans can be performed at the LHC which involve moving one beam position in steps with respect to the other and measuring the hit rates in forward detectors such as LUCID and the ZDC. LUCID is a consists of gas filled tubes acting as a Cherenkov integrating detector surrounding the beam pipe in the forward region $5.4 < |\eta| < 6.1$. The ZDC consists of two zero degree Tungsten-quartz fiber calorimeters at 140m down the beam pipes from the interaction point. With this method the beam spot size, as used in Equation 3.2 can be precisely determined. Smaller scans are used at the start of a run to optimise the luminosity collected. The uncertainty on the bunch currents has been reduced by detailed studies, thus reducing the error on $n_1 n_2$. These measurements combined with accurate measurements of the beam spot position lead to an uncertainty of 3.4% on the luminosity. This is a significant achievement for a relatively young experiment and is testament to the precise control of the entire LHC complex.

Chapter 9

Limit Setting

In a search for new particles it is necessary to set out a robust statistical framework in which it is possible to define the significance of any new signal seen. The same framework should also be able to, in the absence of an observation, make a sensible statement on the strength of signal that could exist and still be consistent with the observed data [76].

For example consider a simple counting experiment with a result of n events observed. A hypothesis can be made on the outcome of the experiment, for example by defining a model of the number of expected background events. A statistical test can be constructed to define for what range of observed events, n, the background only hypothesis, H_b, can be rejected in favour of an alternative signal and background hypothesis, H_{s+b}. Typically an analysis defines a test statistic variable from the data which can discriminate between the two hypotheses. Expected probability density functions (pdf) for the test statistic can then be produced for both hypotheses using toy MC events or via analytical methods. A critical region of the pdf, α, is that in which H_b is rejected if the observed test statistic lies within it. This rejection has a confidence level (CL) equal to $1 - \alpha$, also known as the coverage of the test. Confidence levels in particle physics are typical defined as 95%. Thus there is a 5% chance of rejecting H_b when it is true, this is known as a type one error. Conversely if H_{s+b} is true and H_b is accepted this is a type two error. A type two error has a probability β of occurring and the quantity $1 - \beta$ is defined as the power of the test. These basic principles can be extended to more complex analyses using test statistics based on the full information from kinematic distributions or even discriminating variables from multi-variate analyses.

9.1 Defining the Test Statistic

For the analysis presented in this thesis a profile likelihood ratio (PLR) test statistic is defined using a likelihood function which describes the number of expected signal and background events at a given $\mathcal{B}(t \to H^+b)$. The distributions of the dijet mass in the background $t\bar{t}$, non-$t\bar{t}$ and the three signal mass points are used as the input into the limit setting procedure. Combined they provide the expected number of events in each bin of the distribution and can be used to compare the data to the background expection. The SM background templates are scaled to the total expected number of events as shown in Chapter 6. The signal templates are rescaled within the fit to represent the full range of $\mathcal{B}$. The likelihood function is dependant upon the signal strength, in this case $\mathcal{B}(t \to H^+b)$, and the systematic uncertainties and is defined as,

$$L(\mathcal{B}, \alpha) = \prod_i \frac{\nu_i^{n_i} e^{-\nu_i}}{n_i!} \prod_j \frac{1}{\sqrt{2\pi}} e^{-\frac{\alpha_j^2}{2}}, \tag{9.1}$$

where n_i is the number of events observed in bin i of the dijet mass distribution and j labels the systematic sources. The number of expected events, ν_i in each bin, is given by

$$\begin{aligned} \nu_i = {} & 2\mathcal{B}(1-\mathcal{B})\sigma_{t\bar{t}}\mathcal{L}\varepsilon_{\rangle}^{\mathcal{H}^+} \prod_{|} \rho_{|\rangle}^{\mathcal{H}^+}(\alpha_|) \\ & + (1-\mathcal{B})^2\sigma_{t\bar{t}}\mathcal{L}\varepsilon_{\rangle}^{\mathcal{W}} \prod_{|} \rho_{|\rangle}^{\mathcal{W}}(\alpha_|) + \backslash_{\rangle}^{\lfloor} \prod_{|} \rho_{|\rangle}^{\lfloor}(\alpha_|) \end{aligned} \tag{9.2}$$

where n_i^b is the expected number of non-$t\bar{t}$ background events, $\sigma_{t\bar{t}}$ is the production cross-section for top pair production, $\mathcal{L}$ is the integrated luminosity, $\mathcal{B}$ is the branching ratio of $t \to H^+b$ and $\varepsilon_i^{H^+}$, ε_i^W are the efficiencies to select signal ($t\bar{t} \to H^+bW^-\bar{b}$) and SM $t\bar{t}$ ($t\bar{t} \to W^+bW^-\bar{b}$) events respectively including the effect of the W branching ratios. The ρ_{ji} parameters represent the $\pm1\sigma$ fractional change in the dijet mass spectrum of systematic j and are defined as

$$\rho_{mi}(\alpha) = \prod_{j} I(\alpha_j; \sigma^{+}_{mij}, \sigma^{-}_{mij}) \tag{9.3}$$

where

$$I(\alpha; x^{+}, x^{-}) = \begin{cases} 1 + \alpha x^{+} & \text{if } \alpha > 0 \\ 1 & \text{if } \alpha = 0 \\ 1 - \alpha x^{-} & \text{if } \alpha < 0 \end{cases} \tag{9.4}$$

where σ^{+}_{mij} and σ^{-}_{mij} represent the one σ fractional effect of systematic j, in bin i for process m. By including the uncertainties in this way systematics with an asymmetric shape effect can be included alongside systematics which only have normalisation effects. The α_j variables are parameters in the fit that are constrained via the Gaussian terms in Equation 9.1. Since the final data sample contains a significant number of events, the effect of the systematic uncertainties on m_{jj}, i.e. ρ_{ji} and α_j, can be constrained when the likelihood fit is performed. The first term describes the number of

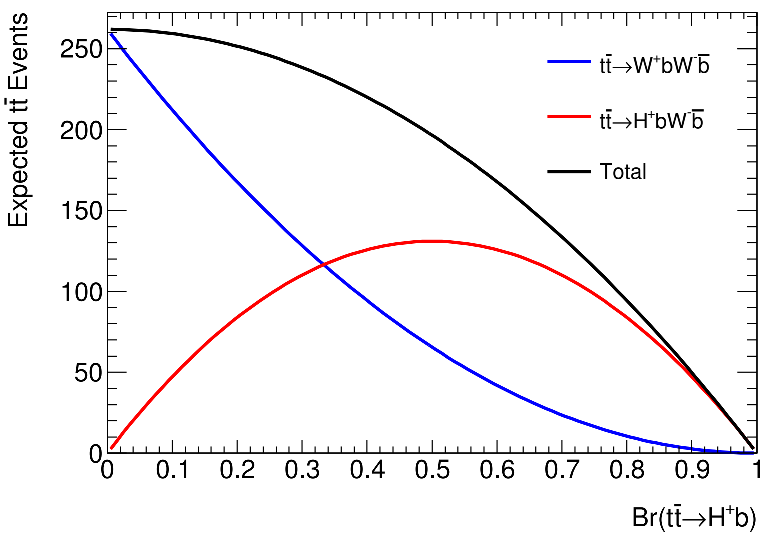

Figure 9.1: Number of expected events after all selection cuts from the SM $t\bar{t}$ background and charged Higgs boson signal as a function of the branching ratio of top to charged Higgs. The number of non-$t\bar{t}$ background events expected is not shown, since this does not depend on the branching ratio.

expected semi-leptonic $t\bar{t}$ decays containing a single $H^{+} \to c\bar{s}$ decay. The second term gives the expected number of semi-leptonic standard model $t\bar{t}$ decays in each bin as a function of $\mathcal{B}$. The third term gives the expected events for the non-$t\bar{t}$ background and does not depend on the $\mathcal{B}$. Figure 9.1 shows in blue the expected decrease in SM $t\bar{t}$ events, decreasing like $(1-\mathcal{B})^2$, as the $\mathcal{B}$ increases. The red line follows the expected number of signal events which follow $\mathcal{B}(1-\mathcal{B})$ and therefore peaks at $\mathcal{B} = 0.5$. At this point the analysis picks up an unusual feature, as the signal $\mathcal{B}$ increases then the total number of expected events decreases, shown by the black line in Figure 9.1. The decay mode $t\bar{t} \to H^+bH^-\bar{b}$ is absent from Equation 9.2 as it does not contain an isolated high p_T lepton. These events therefore have a negligible efficiency, of the order 10^{-6}, to pass the analysis selection requirements. Therefore as the contribution of these events increases, proportional to $\mathcal{B}^2$, they are lost to the analysis and the expected number of events decreases. This is unusual as the presence of a signal would not only show a second peak at the m_{H^+} but also an overall decrease in the number of semi-leptonic $t\bar{t}$ events seen. Therefore both the shape and normalisation of the observed dijet mass distribution contribute significantly to the sensitivity of the analysis. Systematics are considered to be uncorrelated between different sources and each source is considered to be correlated between signal and the background.

A profile likelihood ratio can be defined as,

$$\lambda(\mathcal{B}) = \begin{cases} \frac{L(\mathcal{B},\hat{\hat{\alpha}}(\mathcal{B}))}{L(0,\hat{\hat{\alpha}}(0))} & \text{if } \hat{\mathcal{B}} < 0 \\ \frac{L(\mathcal{B},\hat{\hat{\alpha}}(\mathcal{B}))}{L(\hat{\mathcal{B}},\hat{\alpha})} & \text{if } 0 < \hat{\mathcal{B}} < \mathcal{B} \\ 0 & \text{if } \hat{\mathcal{B}} > \mathcal{B} \end{cases} \tag{9.5}$$

where $\hat{\alpha}$ and $\hat{\mathcal{B}}$ are the maximum likelihood estimators (MLE) for the systematics and the branching ratio for the signal. $\hat{\hat{\alpha}}(\mathcal{B})$ are the conditional MLE for the systematics for a given branching ratio $\mathcal{B}$. It is here that by performing the MLE fits, information from the data can be used to constrain the effect of systematics uncertainties.

A test statistic, $q_{\mathcal{B}}$, based on the profile likelihood ratio is defined as,

$$q_{\mathcal{B}} = -2\ln\lambda(\mathcal{B})\,. \tag{9.6}$$

By defining the test statistic in this way, higher values of $q_{\mathcal{B}}$ show the data are less compatible with the hypothesis. To define the level of disagreement observed, a p-value can be defined,

$$p_{\mathcal{B}} = \int_{q_{\mathcal{B},obs}}^{\infty} f\left(q_{\mathcal{B}}|\mathcal{B}\right) dq_{\mathcal{B}}, \tag{9.7}$$

where $q_{\mathcal{B},obs}$ is the value of the test statistic observed in the data and $f\left(q_{\mathcal{B}}|\mathcal{B}\right)$ is the probability density function (pdf) of the test statistic assuming a branching ratio of $\mathcal{B}$. The pdfs of the test statistic for a range of branching ratios form the core of the statistical test.

9.2 Probability Density Functions

The expected pdf distributions for the PLR test statistic for the background hypothesis and signal plus background hypothesis at any $\mathcal{B}$ can be produced using the input signal and background templates. The expected background hypothesis distribution can be found by producing a set of toy MC by applying poisson fluctuations of the SM templates bin by bin around the expected values. These toy data now represent a set of possible SM datasets that ATLAS could record. By evaluating the test statistic for each of these pseudo data templates the background pdf can be produced. Pseudo data can also be produced with an increasing signal $\mathcal{B}$ in steps of 0.01, producing a set of possible signal plus background templates at each incremental signal point. Repeating the evaluation of the test statistic over these toy data sets the signal plus background pdf's are produced for each incremental step in $\mathcal{B}$. An idealised example of these test statistic pdf's can be seen in Figure 9.2. Here more signal like events tend towards 0 and background events tend to be more evenly distributed offering separation between the two hypotheses.

The p-value for a given set of data for the background only case is found by integrating the pdf obtained from the background-only toy experiments:

$$p_b = \int_{q_{\mathcal{B},obs}}^{\infty} f(q_{\mathcal{B}}|0, \hat{\hat{\alpha}}(0, obs))dq_{\mathcal{B}}. \tag{9.8}$$

Similarly, the p-value for a given signal stength $\mathcal{B}$ of the observation ($p_{\mathcal{B}}$) is found by integrating the pdf for that signal strength $\mathcal{B}$:

$$p_{\mathcal{B}} = \int_{q_{\mathcal{B},obs}}^{\infty} f(q_{\mathcal{B}}|\mathcal{B}, \hat{\hat{\alpha}}(\mathcal{B}, obs))dq_{\mathcal{B}}. \tag{9.9}$$

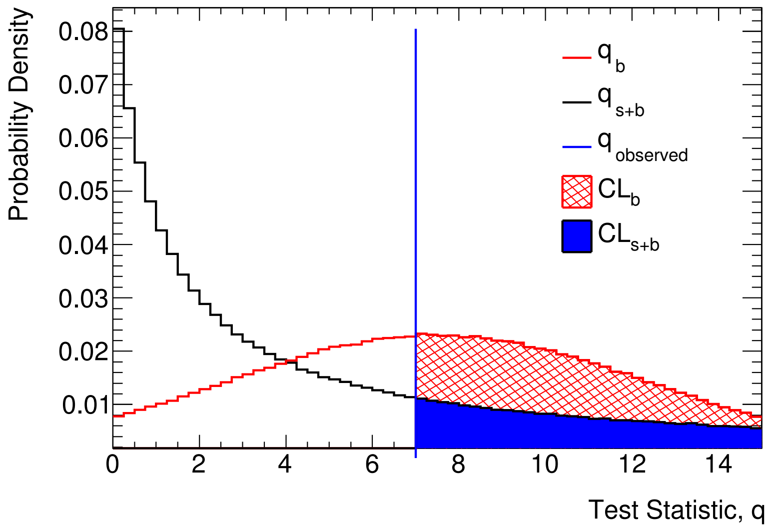

Figure 9.2: Comparison of the distributions for the background and signal plus background expectations for a generic test statistic q. In this example lower test statistic values indicate more signal like events. Also shown is the observed value for the test statistic and the areas integrated to calculate the signal plus background confidence level, CL_{s+b} and the signal confidence level, CL_s.

As shown CL regions can be defined by taking the integral of the expected distributions from the observed value of the test statistic. The two CL regions are the background hypothesis, CL_b, and signal plus background hypothesis, CL_{s+b}, defined as,

$$CL_b = p_b\,(q \geq q_{obs})\,, \tag{9.10}$$

$$CL_{s+b} = p_{s+b}\,(q \geq q_{obs})\,. \tag{9.11}$$

Here $p_b(q \geq q_{obs})$ is the probability that the test statistic result is less signal like than the observed data using the background hypothesis and similarly for $p_{s+b}(q \geq q_{obs})$ using the signal plus background hypothesis.

If a signal is present in the data the background confidence level, $1 - CL_b$, is used to set the level of significance of the data departure from the background model. The consensus in particle physics is that to claim evidence of a new particle or process a statistically significant departure from the expected background result is required. For evidence of a processes existence a 3σ departure from the background is required and for discovery a 5σ departure is needed. These respectively correspond to $CL_b = 2.7x10^{-3}$ and $CL_b = 5.7x10^{-7}$, thus leaving a vanishingly small chance of a background fluctuation causing such a result. Some may call this over cautious, but for large numbers of experiments this offers protection against regular false discoveries and reduces the effect of the 'look-elsewhere' effect[1]. As p_b depends on the test statistic it has to be evaluated at a specific $\mathcal{B}$, for this analysis $\mathcal{B} = 0.1$ was chosen.

If no signal is seen then upper limits can be placed on how much signal could be present in the data. In this case the expected CL_{s+b} is produced for each signal strength considered. Typically a limit is defined at the 95% CL, i.e. the signal contribution is increased until $1 - CL_{s+b} = 0.95$. This signal strength now defines the upper limit at which a signal could occur and still produce the data observed. For limits a less stringent critical region $\alpha = 5\%$ is typically defined, as false exclusions of a signal are generally less troublesome than a false statement of discovery. An expected limit can be produced by poisson fluctuating the expected SM result to produce multiple simulated experiments. For each simulated experiment the upper limit on the $\mathcal{B}(t \rightarrow H^+b)$ can be calculated and a median expected upper limit can be found. The expected 95% CL distribution also provides the $\pm1\sigma$ and $\pm2\sigma$ uncertainty bands. Observed limits are taken simply as the 95%upper limit for the test statistic calculated from the observed data.

9.3 Asymptotic Limits

Producing toy MC to define the pdfs for the background and each $\mathcal{B}$ point can be a computing intensive problem. However as the statistics available to an analysis increases, the distributions for the pdfs asymptotically tend towards an analytically calculable result. This means the large numbers of toys can be replaced by a set of fast analytic functions, vastly reducing the computing time required to set limits or the significance

[1]The 'look-elsewhere' effect refers to the fact that a search over a wide mass range is likely to observe some statistical fluctuations. Care needs to be taken to not assign excessive importance to one of these fluctuations if it happens to lay where you were expecting your signal to be.

of a result [76]. It can be shown [77] that the test statistic for a single parameter of interest can be re-arranged to,

$$q_{\mathcal{B}} = \frac{\left(\mathcal{B} - \hat{\mathcal{B}}\right)^2}{\sigma^2} + \mathcal{O}\left(\frac{1}{\sqrt{N}}\right), \tag{9.12}$$

where is is assumed that $\mathcal{B}$ follows a gaussian distribution with a mean of $\mathcal{B}'$ and a standard deviation σ, with N here representing the number of events in the data sample. For results from sufficiently high statistics the second term become negligible. The test statistic can be shown [78] to simply be a non-central χ^2 distribution with one degree of freedom.

There is an issue remaining in this approach, the σ of $\hat{\mathcal{B}}$ is not a priori known. To estimate σ of $\hat{\mathcal{B}}$ an artificial data set is defined such that the MLE are equal to the true parameters. This data set is known as the "Asimov data set". This data set can be taken to be approximately the expectation from MC, assuming large statistics, at the required $\mathcal{B}$, taking into account the expected loss of events with increasing $\mathcal{B}$ shown in Equation 9.2. Defining this single data set for each pdf is trivial since it is just the expected number of events for a given set of parameters. As this Asimov data set for a branching ratio $\mathcal{B}'$ is defined to have a MLE of $\hat{\mathcal{B}} = \mathcal{B}'$ it can be shown that,

$$-2\ln\lambda_A(\mathcal{B}) \approx \frac{(\mathcal{B} - \mathcal{B}')^2}{\sigma_A^2}, \tag{9.13}$$

and also,

$$\sigma_A^2 = \frac{(\mathcal{B} - \mathcal{B}')^2}{q_{Br,A}}, \tag{9.14}$$

where $-2\ln\lambda_A(\mathcal{B})$ is the test statistic for the Asimov data, $q_{\mathcal{B},A}$. From Equations 9.13 and 9.14 it is possible to obtain the parameters describing the χ^2 function and therefore define the pdf for any given $\mathcal{B}$. The limits gained using this method to define the pdf were verified by comparison to the limits gained from producing toy data. The limits agreed favourably within $\mathcal{B} < 1\%$, which is around the statistical accuracy of the limit. This suggests first that the method is valid and that the analysis, with 35.3pb^{-1}, has a large enough N to make the assumptions for the asymptotic limits valid. The asymptotic formulae were therefore used in setting the final limits presented here.

9.4 CL_s

Issues can arise surrounding the sensitivity and power of the limit setting method. For example if the test statistic for the background and signal plus background hypotheses are very similar then the analysis will have very little discriminating power between the two. In this case a limit can be found on the signal much lower than the experiment is actually sensitive to. CL_s [79] has been widely used in the past at LEP experiments and at the Tevatron. This technique uses the background CL_b to protect against situations where the two hypotheses are poorly separated. CL_s is defined as;

$$CL_s = \frac{CL_{s+b}}{CL_b}. \tag{9.15}$$

CL_s can then be used in the same way as CL_{s+b}, varying the signal contribution until the critical region is reached. In this way the CL_b contribution softens any limits gained. The effect is to increase the coverage of the test from the quoted 95% to 100% in a smooth fashion. If the pdfs for the two hypotheses are well separated the softening of the limit will be minimal due to the small overlap. As the pdfs become more indistinguishable the contribution of CL_b will increase and the limit will be softened representing the loss in confidence in the power of the analysis to distinguish the two scenarios. The main failing of CL_s cited by its opponents is that it is not a true probability, instead only a ratio of probabilities. In this way it becomes more difficult to infer the level of over-coverage from 95%. The main limits quoted in this analysis will use the CL_s method described here.

Chapter 10

Results

In this chapter the 35.3pb^{-1} of data recorded by ATLAS will be compared to the background expectations. The procedures set out in Chapter 9 will be used to test the agreement of the data with the signal and background hypotheses. The systematic uncertainties presented in Chapter 8 are included in the statistical treatment of the data. The final results will be shown, explained and compared with previous results.

10.1 Consistency of Data with the Standard Model

The data are compared with the SM expectation using the dijet mass spectrum as shown in Figure.10.1. The data are seen to be in good agreement with the SM expectations. The shaded band shows the uncertainty on the background prediction. The band includes all $\pm 1\sigma$ systematic uncertainties combined in quadrature. To test if any significant deviation from the background only model has been observed CL_b has been calculated for a $\mathcal{B} = 0.1$. This p-value was found to vary between 0.67 and 0.71 across the range of m_{H^+} studied. This shows that the data are indeed statistically consistent with the expectation from the SM hypothesis. A significant deviation from the background caused by a signal would have been apparent if a small p-value was observed. The values observed suggest a slight upwards fluctuation in the data away from the median expectation for background. This can be confirmed by looking at the data to Standard Model MC comparison in Figure 10.1.

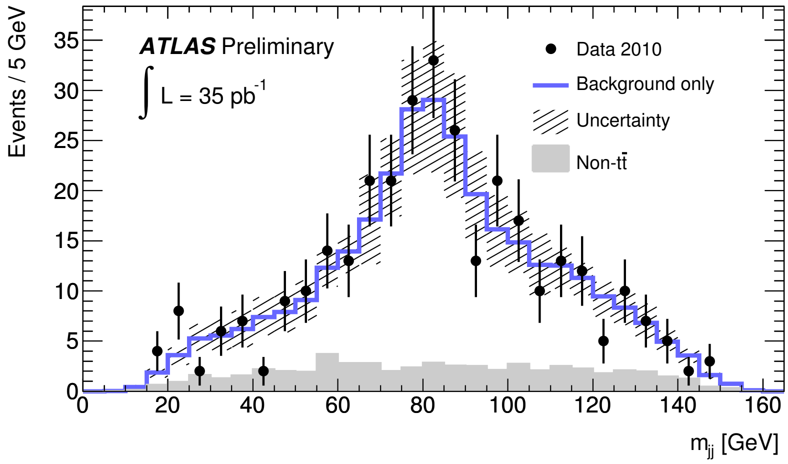

Figure 10.1: The data are compared to the SM expectation as described by MC and data driven methods. The full uncertainty on the the SM expectation is shown as the shaded area. This uncertainty can be constrained by the data in the likelihood fit.

10.2 Limits

Upper limits have been set on $\mathcal{B}(t \to H^+b)$ assuming that $\mathcal{B}(H^+ \to c\bar{s}) = 100\%$. The limit is a combination of both branching ratios. These limits can be used directly in a model where the charged Higgs is lighter than the top and decays to predominantly to hadrons. As no assumption has been made on the flavour of the quarks in the dijet system the limits are equally applicable to models with decays to $u\bar{d}$. Using the limits in models with more decay options for charged Higgs bosons is a more delicate task. The validity of the limits hold if the non-hadronic decays available in the model have a low acceptance through the analysis cuts.

The expected limits have been evaluated using the asymptotic formulae and the CL_s method. The validity of these formulae for this analysis was assessed by first running the limit setting procedure using toy MC to calculate the expected limits. These results were then compared with a set gained using the asymptotic formulae. The limits produced by both methods agree to within $\mathcal{B} < 1\%$. This is of the order of the statistical accuracy of the limits. This therefore shows the analysis is within the asymptotic regime, allowing the usage of the asymptotic formulae to produce the probability density functions.

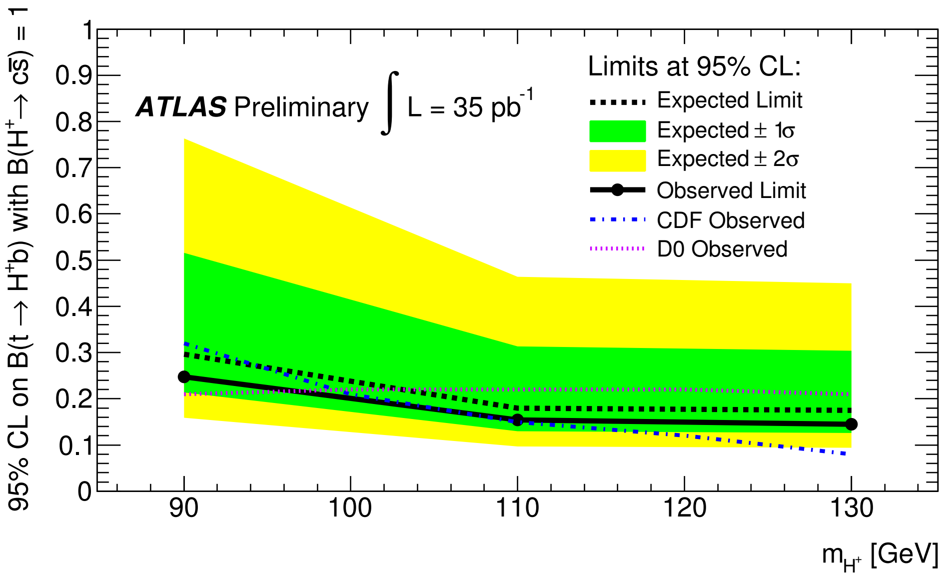

Figure 10.2: The extracted 95% C.L. upper limits on $\mathcal{B}(t \rightarrow H^{+}b)$ from the ATLAS data are compared with the expected results and results from the Tevatron. The results assume $\mathcal{B}(H^{+} \rightarrow c\bar{s} = 100\%)$. The ATLAS limits shown are calculated using the CL_s limit setting procedure. The green and yellow bands show the one and two sigma uncertainties on the expected limit respectively.

The systematic effects described in Chapter 8 were all included in the final limit setting procedure. The systematics were all assumed to be 100% correlated between the signal and SM $t\bar{t}$ samples. The CL_s limits gained from the data can be seen in both Table 10.1 and Figure 10.2. The limits follow the expected pattern, with the limits worsening as m_{H^+} approaches m_W. This is due to the increasing difficulty separating the H^+ mass peak from the SM W mass peak. The observed results are consistently better than the expected limits but all lie within the one sigma uncertainty band of the expected results.

To understand the tighter than expected limits it is necessary to study Figures 10.3 and Figure 10.4. Figure 10.3 compares the data with the SM expectation and the distribution if a signal was present with a $\mathcal{B}$ at the expected limit for each mass point. The number of expected signal and background events for the expected $\mathcal{B}$ are found

Higgs Mass	Expected limit	Observed limit
90 GeV	0.30	0.25
110 GeV	0.18	0.15
130 GeV	0.17	0.14

Table 10.1: Expected and observed 95% CL limits on the branching ratio of top to a charged Higgs boson and a b-quark. The limits shown are calculated using the CL_s limit setting procedure.

using Equation 9.2. Figure 10.4 shows the same but with the observed limits. The figures show that there is a slight upward fluctuation in the data at the W-mass peak. This is a fluctuation away from the signal expectation. If a signal was present, the events expected at 80 GeV would be reduced. As $\mathcal{B}(t \rightarrow H^{+}b)$ increases events begin to decay to charged Higgs bosons, thus forming a secondary peak at $m_{H^{+}}$. The loss of events to the channel containing two charged Higgs decays also exasperates the disappearance of events under the W mass peak at higher $\mathcal{B}$. The removal of these events causes a reduction in the total number of events expected across the whole range. A secondary effect causing the stronger observed limits is the lack of any upwards fluctuations consistent with a secondary mass peak from a charged Higgs. Combined these two reasons explain why the observed limits are consistently lower than expected across the full mass range.

The observed limits can be compared to previous results from the Tevatron experiments. The analysis at CDF followed a similar method to the one presented in this thesis, however it set limits using a Bayesian procedure. The D0 analysis used a simpler cut and count method looking at the balance between the different $t\bar{t}$ decay channels. The observed limit from this analysis is competitive with both the D0 and CDF results. Both Tevatron results were made with significantly more data than this analysis, D0 used 1fb^{-1} whereas CDF used 2.2fb^{-1}. However the significant increase in $\sigma_{t\bar{t}}$ between the Tevatron energies and the LHC increases the sample of $t\bar{t}$ events available in the smaller ATLAS dataset of 35pb^{-1} to an almost equivalent level. The effort to retain high statistics by only requiring a single b-tag and allowing the fifth jet to be used in the fit allows the analysis to be fully competitive.

The results presented here are the first charged Higgs results from ATLAS and the first studying the $H^+ \to c\bar{s}$ channel at the LHC. The analysis has been presented at the EPS-HEP conference 2011 in Grenoble [80].

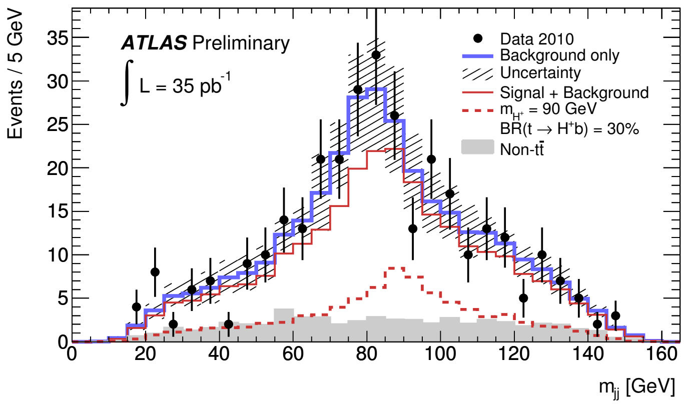

(a)

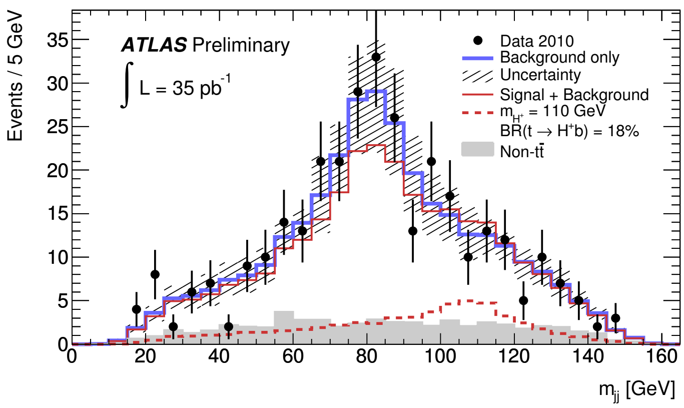

(b)

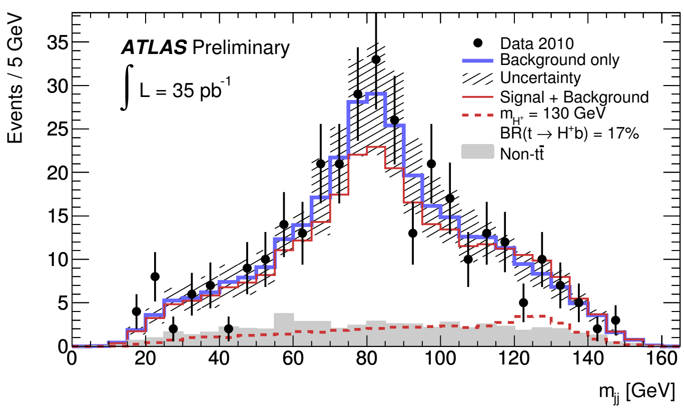

(c)

Figure 10.3: The dijet mass distribution of the data are compared with the expectation from the SM ($\mathcal{B} = 0$) and with (a) the expectation with $\mathcal{B} = 0.30$ ($m_{H^+} = 90$ GeV), (b) the expectation with $\mathcal{B} = 0.18$ ($m_{H^+} = 110$ GeV) and (c) the expectation with $\mathcal{B} = 0.17$ ($m_{H^+} = 130$ GeV). The error bars represent the statistical uncertainty from the data. The uncertainty shown on the background estimate is the combination in quadrature of the $\pm 1\sigma$ systematic uncertainties. The size of these uncertainties can be constrained by the data in the likelihood fit.

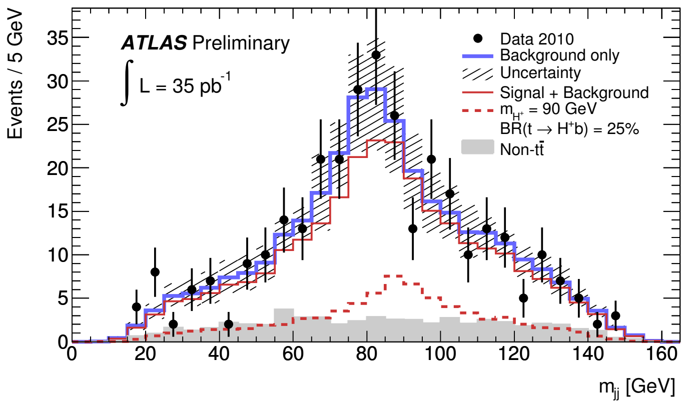

(a)

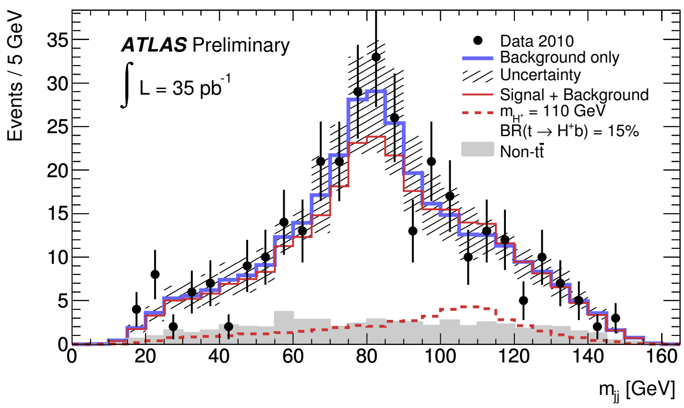

(b)

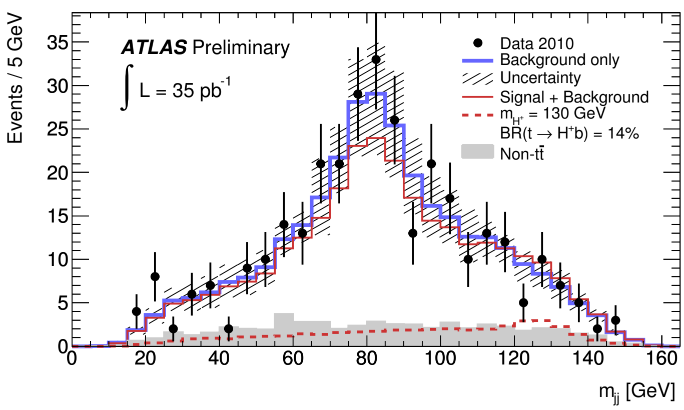

(c)

Figure 10.4: The dijet mass distribution of the data are compared with the expectation from the SM ($\mathcal{B} = 0$) and with (a) the observed limit at $\mathcal{B} = 0.25$ ($m_{H^+} = 90$ GeV), (b) the observed limit at $\mathcal{B} = 0.15$ ($m_{H^+} = 110$ GeV) and (c) the observed limit at $\mathcal{B} = 0.14$ ($m_{H^+} = 130$ GeV). The error bars represent the statistical uncertainty from the data. The uncertainty shown on the background estimate is the combination in quadrature of the $\pm 1\sigma$ systematic uncertainties. The size of these uncertainties can be constrained by the data in the likelihood fit.

Chapter 11

Conclusion

A search for a charged Higgs boson decaying hadronically in semi-leptonic $t\bar{t}$ events has been presented. The analysis used 35pb^{-1} of pp collision data recorded in 2010 by the ATLAS detector at the LHC in CERN. No significant signal is observed in the data. Limits are set on the branching ratio $\mathcal{B}(t \to H^+ b)$ at three separate m_{H^+} under the assumption that $\mathcal{B}(H^+ \to c\bar{s}) = 100\%$. These limits are the first LHC charged Higgs results in the decay channel $H^+ \to c\bar{s}$. Additionally they are the first charged Higgs limits to be presented by ATLAS.

The data are initially selected in two separate channels by triggering on events containing an electron or muon with a transverse momentum $p_T > 20$ GeV. Further kinematic selection requirements are made to preferentially select semi-leptonic $t\bar{t}$ events: at least four high p_T jets with at least one tagged as originating from a b-quark and high $E_{\mathrm{T}}^{\mathrm{miss}}$. The main irreducible background to the signal process is the SM semi-leptonic $t\bar{t}$ events. The main reducible backgrounds are W/Z boson production in association with jets, QCD multijet, single top and diboson events. The QCD multijet background is estimated by two data driven methods, one for each lepton channel. The rest of the backgrounds are estimated using Monte Carlo generators to model the shape and numbers of expected events. These simulations are then corrected to take into account differences in the b-tagging efficiency, lepton identification, triggering and reconstruction between data and MC.

The data are fit to reconstruct the dijet mass system originating from the hadronic decay of either a SM background W or the signal H^+ bosons. A χ^2 fitter is employed to fully reconstruct the $t\bar{t}$ events using the top-quark and W-boson masses to constrain the the possible object combinations. The most likely assignment of jets to partons is selected by the fit therefore reconstructing the dijet mass system. During the fit the jet p_T values are transferred back to the partonic level by a set of quark flavour dependant transfer functions. In doing so the fitter improves the resolution of the dijet system and allows for greater signal and background separation.

The reconstructed dijet mass distribution is used to search for a charged Higgs boson signal in the data. No significant signal is observed with the data in agreement with the SM expectation. As no excess is seen 95% confidence limits are set on the $\mathcal{B}(t \to H^+b)$ for charged Higgs bosons in the range 90 GeV $< m_{H^+} <$ 130 GeV. For these limits the charged Higgs is assumed to decay via $H^+ \to c\bar{s}$ with a branching ratio of 100%. The observed limits are in the range 25% at 90 GeV to 14% at 130 GeV. These limits are comparable to previous Tevatron limits from D0 and CDF, but use around 25 times less data.

With the continued success of LHC and ATLAS running the parameter space allowed for new physics is being rapidly reduced. Limits on the charged Higgs have been improved recently with results from CMS and ATLAS in the $H^+ \to \tau\nu$ channel, with the CMS results excluding down to 4%. With an increase in data this analysis could complement these searches leading to the discovery or exclusion of a charged Higgs boson at a low branching ratio. Further searches could be performed extending the methods to the the high mass range (above the top-quark mass) where the charged Higgs would mainly decay via $H+ \to t\bar{b}$.

Appendix A

QED

Electromagnetic interactions between charged particles are described by Quantum Electro Dynamics (QED) which is the simplest of the gauge theories. The Lagrangian for a massless electron, which can be written as,

$$\mathcal{L} = i\bar{\psi}\gamma^{\mu}\delta_{\mu}\psi, \tag{A.1}$$

where ψ is a complex field describing the electron, γ^{μ} are Dirac γ-matrices. This Lagrangian can be shown to be invariant under local phase transformations,

$$\psi(x) \rightarrow e^{i\alpha(x)}\psi(x), \tag{A.2}$$

where the phase $\alpha(x)$ is described as local as it depends upon the space-time position, x. Phase transformations of this type, $e^{i\alpha}$, form a unitary Abelian group known as U(1). Abelian means that the group multiplication is commutative. Invariance under this transformation would imply a conserved current. A problem arises due to the presence of the δ_{μ} in the Lagrangian which breaks this invariance. It is therefore necessary to replace δ_{μ} with the covariant derivative, D_{μ} which transforms covariantly under local phase transformations, i.e. it is also invariant under the phase transformation. The covariant derivative is defined as,

$$D_{\mu} \equiv \delta_{\mu} - ieA_{\mu}, \tag{A.3}$$

where A_{μ} is a vector field that transforms like,

$$A_{\mu} \rightarrow A_{\mu} + \frac{1}{e}\delta_{\mu}\alpha. \tag{A.4}$$

This vector field A_μ can be regarded as a physical photon field which couples to charged particles, thus mediating the electromagnetic force. By replacing δ_μ with the covariant derivative the QED Lagrangian is revealed as,

$$\mathcal{L} = i\bar{\psi}\gamma^\mu\delta_\mu\psi + e\bar{\psi}\gamma^\mu A_\mu\psi - \frac{1}{4}F_{\mu\nu}F^{\mu\nu}. \tag{A.5}$$

Here the first term is the original Lagrangian for the electron field. The second term is the result of applying the covariant derivative to the original Lagrangian. It describes the the interaction of the fermion field with the gauge field. The third term is introduced as the gauge invariant kinetic term for the new vector field A_μ, where $F_{\mu\nu}$ is the gauge invariant field strength tensor,

$$F_{\mu\nu} = \delta_\mu A_\nu - \delta_\nu A_\mu. \tag{A.6}$$

Assuming that A_μ transforms as in Equation A.4, the addition of a explicit mass term, $\frac{1}{2}m^2 A_\mu A^\mu$ would not be gauge invariant. Therefore the photon and indeed any boson created by such a method will be massless. As the photon field has no charge it does not self couple. Thus, requiring the invariance of the Lagrangian under the U(1) local gauge transformations describes a new photon field mediating the electromagnetic force and reproduces the well-measured results of QED.

Appendix B

Neutrino Momentum Solutions

Semi-leptonic $t\bar{t}$ events contain a single neutrino from the leptonic decay of a W. The $p_{L(\nu)}$ component of the neutrino momentum is an unknown of the $t\bar{t}$ system as the centre of mass energy of the initial parton-parton interaction is unknown. The $E_{\mathrm{T}}^{\mathrm{miss}}$ measured in the events can be interpreted as the $p_{T(\nu)}$, assuming no other sources of $E_{\mathrm{T}}^{\mathrm{miss}}$ are present in the event. To fully reconstruct the leptonic top present in the $t\bar{t}$ events the $p_{L(\nu)}$ information needs to be calculated somehow. By constraining the the lepton and the neutrino four-vectors, P_l and P_ν, to be equal to the W boson mass, $m_W = 80.4$ GeV, the value of $p_{L(\nu)}$ can be inferred.

The calculation begins with the previously stated constraint;

$$m_W^2 = (P_l + P_\nu)^2\,, \tag{B.1}$$

then by assuming the system is produced on mass shell

$$P_\nu^2 = 0, \;\; P_l^2 = m_l^2, \tag{B.2}$$

and by also taking $m_l^2 \ll m_W^2$, this can be re-arranged to,

$$E_\nu = \frac{1}{E_l}\left(\frac{m_W^2}{2} + 2p_l.p_\nu\right). \tag{B.3}$$

Neutrinos all have a negligible mass therefore E_ν can be taken to be,

$$E_\nu = \sqrt{\left(p_{x(\nu)}^2 + p_{y(\nu)}^2 + p_{z(\nu)}^2\right)}. \tag{B.4}$$

Equation B.3 can be expanded into the separate momentum components and re-arranged to give a quadratic equation in powers of the longitudinal neutrino momentum, $p_{L(\nu)} = p_{\nu z}$,

$$0 = a.p_{L(\nu)}^2 + b.p_{L(\nu)} + c, \tag{B.5}$$

where the three coefficients a, b, c are given, alongside a constant factor d, as,

$$a = E_l^2 - p_{z(l)}^2, \tag{B.6}$$

$$b = -2d.p_{z(l)}, \tag{B.7}$$

$$c = E_l^2.p_{T(\nu)} - d^2, \tag{B.8}$$

$$d = \left(\frac{m_W^2}{2} + p_{x(l)}.p_{x(\nu)} + p_{y(l)}.p_{y(\nu)}\right). \tag{B.9}$$

By solving this equation using the usual quadratic formula,

$$p_{L(\nu)} = \frac{-b \pm \sqrt{b^2 - 4ac}}{2a}, \tag{B.10}$$

we obviously gain two solutions for the longitudinal neutrino momentum. These solutions can then be used to form the full neutrino momentum and reconstruct the leptonically decaying top quark.

Bibliography

[1] Gfitter Collaboration, arXiv:1107.0975v1 (2011).

[2] ALEPH Collaboration, arXiv:hep-ph/1012.2367 (2010).

[3] F. Halzen, A.D. Martin, *Quarks and Leptons*. John Wily & Sons, 1984.

[4] K. Nakamura *et al.* J. Phys. G **37**, 075021 (2010).

[5] F. Englert and R. Brout, Phys. Rev. Lett. **13**, 321 (1964).

[6] P. W. Higgs, Phys. Lett. **12** 132 (1964).

[7] G. Guralnik *et al.* Phys. Rev. Lett. **13** 585 (1964).

[8] MuLan Collaboration, Phys. Rev. Lett. **99**, 99 (2007).

[9] ALEPH Collaboration, Phys. Lett. B **526** 191 (2002).

[10] DetPHI Collaboration, Eur. Phys. J. C **32** 145 (2004).

[11] L3 Collaboration, Phys. Lett. B **517** 319 (2001).

[12] OPAL Collaboration, Eur. Phys. J. C **26** 479 (2003).

[13] The LEP Higgs working group, Phys. Lett. B **565** 61 (2003).

[14] CDF and D0 Collaborations, [arXiv:1107.5518] (2011).

[15] ATLAS Collaboration, ATLAS-CONF-2011-112 (2011).

[16] CMS Collaboration, CMS-PAS-HIG-11-011 (2011).

[17] L. Susskind, Phys. Rev. D **20**, 2619 (1979).

[18] H. Fritzsch *et al.* Prog. Part. Nucl. Phys. **45**, 1-81 (2000).

[19] G. Bertone *et al.* Phys.Rept. **405**, 279-390 (2005).

[20] M. Markevitch *et al.* Astrophys.J. **606**, 819-824 (2004).

[21] A. D. Sakharov, JETP Lett. **5**, 24 (1967).

[22] A. D. Sakharov, Soviet Physics Uspekhi **34** 392 (1991).

[23] S. P. Martin, arXiv:hep-ph/9709356 (2011).

[24] H. Nishino *et al.* Phys.Rev.Lett. **102**, 141801 (2009).

[25] R. Eusebi, FERMILAB-THESIS-2005-33 (2005).

[26] J. S. Lee, *et al.* Comput. Phys. Commun. **156** (2004).

[27] H. E. Logan and D. MacLennan Phys. Rev. D **81**, 075016 (2010).

[28] M. Aliev *et al.* Comput.Phys.Commun. **182**, 1034-1046 (2011).

[29] S. Moch, and P. Uwer, Phys. Rev. D **78**, 034003 (2008).

[30] ATLAS Collaboration, ATLAS-CONF-2011-100 (2011).

[31] CMS Collaboration, TOP-11-001-PAS (2011).

[32] ALEPH Collaboration, Phys. Lett. B **543**, 1 (2002).

[33] DetPHI Collaboration, Phys. Lett. B **525**, 17 (2002).

[34] L3 Collaboration, Phys. Lett. B **575**, 208 (2003).

[35] OPAL Collaboration, Eur. Phys. J. C **7**, 407 (1999).

[36] CDF Collaboration, Phys. Rev. Lett. **103**, 101803 (2009).

[37] D0 Collaboration, Phys. Lett. B **682**, 278 (2009).

[38] C. Lefevre, CERN-DI-0812015 (2008).

[39] L. Evans and P. Bryant, JINST **3** S08001 (2008).

[40] ATLAS Collaboration, Phys. Rev. Lett. **105** (2010) 252303.

[41] ATLAS Collaboration, arXiv:0901.0512 (2009).

[42] ATLAS Collaboration, JINST **3** S08003 (2008).

[43] P. Betl *et al.* ATL-DAQ-PROC-2009-047 (2009).

[44] S. Marti-Garcia, ATL-COM-INDET-2011-069 (2011).

[45] ATLAS Collaboration, ATL-PHYS-PUB-2011-006 (2011).

[46] ATLAS Collaboration, ATL-PHYS-PUB-2011-007 (2011).

[47] ATLAS Collaboration, Eur.Phys.J. C **71**, 1577 (2011).

[48] B. Resende, ATL-COM-PHYS-2009-519 (2009).

[49] M. Cacciari *et al.* JHEP **2008** 04, 063 (2008).

[50] ATLAS Collaboration, ATLAS-CONF-2011-007 (2011).

[51] B. Alvarez *et al.* ATL-COM-PHYS-2011-124 (2011).

[52] J. Pumplin, *et al.* JHEP **0207**, 012 (2002).

[53] A.D. Martin *et al.* Eur.Phys.J. C**63**, 189-285 (2009).

[54] ATLAS Collaboration, Eur. Phys. J. C **70**, 823 (2010).

[55] T. Sjöstrand, S. Mrenna and P. Z. Skands JHEP **0605**, 026 (2006).

[56] ATLAS Collaboration, ATLAS-CONF-2010-031 (2010).

[57] S. Frixione and B.R. Webber, JHEP **0206** 029 (2002).

[58] S. Frixione and B.R. Webber, JHEP **0308** 007 (2003).

[59] ATLAS Collaboration, ATLAS-PHYS-PUB-2010-014 (2010).

[60] G. Corcetla *et al.* JHEP **0101** 010 (2001).

[61] J. M. Butterworth *et al.* Z. Phys. C **72**, 637-646 (1996).

[62] S. Alioli, P. Nason, C. Oleari and E. Re, JHEP **06**, 043 (2010).

[63] S. Frixione, P. Nason, and C. Oleari, JHEP **11**, 070 (2007).

[64] P. Nason, JHEP **11**, 040 (2004).

[65] S. Frixione, P. Nason and G. Ridolfi, JHEP **09**, 126 (2007).

[66] B. P. Kersevan and E. Richter-Was, arXiv:hep-ph/0405247 (2004).

[67] M. L. Mangano *et al.* JHEP **0307**, 001 (2003).

[68] M. L. Mangano *et al.* Nucl. Phys. B **632**, 343-362 (2002).

[69] F. Caravaglios *et al.* Nucl. Phys. B **539**, 215-232 (1999).

[70] ATLAS Collaboration, ATLAS-CONF-2011-011 (2011).

[71] ATLAS Collaboration, ATLAS-CONF-2011-035 (2011).

[72] F. James and M. Roos, Comput.Phys.Commun. **10**, 343-367 (1975).

[73] G. Romeo *et al.* ATL-COM-PHYS-2011-240 (2011).

[74] D0 Collaboration Phys. Rev. Lett. **107**, 082004 (2011).

[75] CDF Collaboration, Phys. Rev. D**83**, 111101 (2011).

[76] G. Cowan *et al.* Eur.Phys.J. C **71**, 1554 (2011).

[77] A. Wald, Trans. of the American Mathematical Society **54** Vol. 3 426-482 (1943).

[78] S. S. Wilks, Ann. Math. Statist. **9**, 60-2 (1938).

[79] A. L. Read, CERN-OPEN-2000-205 (2000).

[80] ATLAS Collaboration, ATLAS-CONF-2011-094 (2011).